2020

Correlating In-Situ Monitoring Data with Internal Defects in Laser Powder Bed Fusion Additive Manufacturing

Andrew J. Harvey
Wright State University

CORRELATING IN-SITU MONITORING DATA WITH INTERNAL DEFECTS IN LASER POWDER BED FUSION ADDITIVE MANUFACTURING

A thesis submitted in partial fulfillment of the
requirements for the degree of
Master of Science in Mechanical Engineering

By

ANDREW J. HARVEY

B.S.M.E., Wright State University, 2018

2020

Wright State University

WRIGHT STATE UNIVERSITY

GRADUATE SCHOOL

07/24/2020

I HEREBY RECOMMEND THAT THE THESIS PREPARED UNDER MY SUPERVISION BY Andrew J. Harvey ENTITLED Correlating In-situ Monitoring Data with Internal Defects in Laser Powder Bed Fusion Additive Manufacturing BE ACCEPTED IN PARTIAL FULFILLMENT OF THE REQUIREMENTS FOR THE DEGREE OF Master of Science in Mechanical Engineering.

_____

Joy Gockel, Ph.D.
Thesis Director

_____

Raghavan Srinivasan, Ph.D., P.E.
Chair, Mechanical and Materials Engineering Department

Committee on Final Examination:

_____

Joy Gockel, Ph.D.

_____

Nathan Klingbeil, Ph.D.

_____

John Middendorf, Ph.D.

_____

Barry Milligan, Ph.D.
Interim Dean of the Graduate School

ABSTRACT

Harvey, Andrew J. M.S.M.E., Department of Mechanical and Materials Engineering, Wright State University, 2020. Correlating In-Situ Monitoring Data with Internal Defects in Laser Powder Bed Fusion Additive Manufacturing.

The presence of defects within laser powder bed fusion (LPBF) parts can lead to reduced mechanical properties and life of components. Because of this, the ability to detect these defects within the parts is critical before the part is subject to its intended loading. Normally the parts are subjected to a quality analysis once they are completed however, this process is typically expensive and time consuming. A solution for these problems is to sense the creation of defects and pores in the parts in-situ, while the part is being fabricated. One proposed method of in-situ monitoring is visible spectroscopy to identify defects based on the light intensities during prints. In this work, in-situ spectroscopy intensities and ex-situ computed tomography defect data are compared for different processing parameters and two LPBF builds to determine correlation. Results show that changes in the signals from the spectroscopy occur for different conditions of processing parameters and geometries.

Table of Contents

Chapter 1 Introduction and Literature Review 1

1.1 Additive Manufacturing 1

1.2 Laser Powder Bed Fusion 2

1.2.1 Terminology in LPBF 3

1.2.2 Microstructure 7

1.2.3 Rosenthal Heat Transfer 8

1.3 Processing Parameters 10

1.4 Post Processing 12

1.4.1 Hot Isostatic Pressing 12

1.4.2 Other Post Processing 13

1.5 Defects in Additive Manufacturing 13

1.5.1 Defects in Laser Powder Bed Fusion 14

1.6 Defect Detection 17

1.6.1 Post Build Defect Sensing 18

1.6.2 In-situ Defect Sensing 19

1.7 Thesis Contributions 22

Chapter 2 Effects on Spectroscopy Data of LPBF Single Beads with Varied Processing Parameters (Variable Experiment) 24

2.1 Introduction 24

2.2 Theory 24

2.3 Experiment Setup 25

2.3.1 Build 25

2.3.2 Machine 27

2.3.3 Material 28

2.3.4 Spectroscopy 29

2.3.5 Processing Parameters 29

2.4 Analysis 31

2.4.1 Cooling Rate Calculation 32

2.4.2 Isolating Build Intensity Data 33

2.4.3 Intensity Values 41

2.4.4 Generating Equation of Processing Parameters 46

2.5 Results 54

2.5.1 Harvey's Theorem 55

2.5.2 Estimating Intensity Values 56

2.5.3 Error of Estimation 60

2.5.4 Line to Continuum 66

2.5.5 Summary of Trends Based on Varying Processing Parameters 67

2.6 Discussion 68

2.7 Conclusion 71

2.7.1 Carryover to Big Little Experiment 72

Chapter 3 Analysis of In-situ Spectroscopy Data of Laser Powder Bed Fusion Build (Big Little Experiment) 73

3.1 Introduction 73

3.2 Theory 73

3.3 Experiment Setup 74

3.3.1 Build 74

3.3.2 Machine 76

3.3.3 Material 77

3.3.4 Monitoring Setup 77

3.3.5 Processing Parameters 77

3.3.6 Scan Patterns 77

3.4 Analysis 79

3.4.1 Extracting Spectroscopy Data 79
3.4.2 Separating Builds 81
3.5 Layer by Layer Analysis 87
3.5.1 Average Intensity per Layer 87
3.5.2 Line to Continuum Ratio per Layer 91
3.6 CT Data 91
3.6.1 Porosity Analysis 92
3.6.2 Number of Pores per Layer 93
3.7 Results 97
3.7.1 Layer by Layer 97
3.7.2 Relative Comparison 105
3.7.3 Spatial Relation Attempt 113
3.8 Discussion 117
3.9 Conclusion 120
Chapter 4 Conclusion 122
Chapter 5 Future Work 125
5.1 Collect More Data 125
5.1.1 Build Geometries 125

5.1.2 Material Variety 125

5.1.3 Processing Parameter Combinations 126

5.2 Machine Learning 126

5.2.1 Training Model 126

5.2.2 Scrap or Correct Builds based on In-situ Monitoring 127

References 128

Table of Equations

Equation 1.1 Rosenthal Dimensionless Temperature [15] 9

Equation 1.2 Alternate Rosenthal Dimensionless Temperature [15]..... 10

Equation 1.3 Dimensionless Cooling Rate [14, 13]..... 10

Equation 1.4 Line to Continuum Ratio [35] 22

Equation 2.1 General form of Intensity, Power, and Velocity Relationship 53

Equation 2.2 Harvey's Theorem..... 55

Equation 2.3 Percent Error Calculation [41]..... 60

Equation 2.4 Coefficient of Determination (R^2) [42] 64

Equation 3.1 Tolerance Line (Tline)..... 82

Table of Figures

Figure 1.1 AM Part Progression from Design to Finish 1

Figure 1.2 Laser Powder Bed Fusion System [5] 2

Figure 1.3 Melt Pool Model [7] 4

Figure 1.4 Computer Imaging of Plume Isolation [8] 5

Figure 1.5 Spatter Expelled from Melt Pool and Removed by Inert Gas Flow [10] 7

Figure 1.6 Microstructure for a) Columnar Grains b) Equiaxed Grains [11] 8

Figure 1.7 Geometry of Rosenthal Heat Transfer Solution [14] 9

Figure 1.8 Common Processing Parameters in LPBF [16] 11

Figure 1.9 Common HIP Device [18] 12

Figure 1.10 Lack of Fusion of a LPBF Build [24] 15

Figure 1.11 LPBF with High Speed X-Ray Monitoring [25] 16

Figure 1.12 LPBF Defect Categorization by Processing Parameters [26] 17

Figure 1.13 CT Scan of LPBF Part [27] 18

Figure 1.14 Sensing Methods Matrix for LPBF [29] 20

Figure 2.1 Variable Experiment Build Plate CAD Renderings 26

Figure 2.2 Variable Experiment Build Plate Photograph 27

Figure 2.3: Open Additive PANDA LPBF Machine [36] 28

Figure 2.4 Variable Experiment Build Parameters 31

Figure 2.5 Variable Experiment Cooling Rate vs. Normalized Melt Pool Depth 32
Figure 2.6 Variable Processing Parameter Raw Broadband Intensity Data 33
Figure 2.7 Variable Processing Parameter 520 nm and 530 nm Raw Intensity Data..... 34
Figure 2.8 Variable Processing Parameter Original Broadband Build Data 35
Figure 2.9 Variable Processing Parameter Updated Broadband Build Data 36
Figure 2.10 Variable Processing Parameter Original 520 nm Build Data..... 37
Figure 2.11 Variable Processing Parameter Updated 520 nm Build Data..... 38
Figure 2.12 Variable Processing Parameter Original 530 nm Build Data..... 39
Figure 2.13 Variable Processing Parameter Updated 530 nm Build Data..... 40
Figure 2.14 Normal Distribution of Broadband Intensity for P=450 W, V=500 mm/s.... 41
Figure 2.15 Variable Processing Parameter Average Broadband Intensity..... 42
Figure 2.16 Variable Processing Parameter Average 520 nm Intensity 44
Figure 2.17 Variable Processing Parameter Average 530 nm Intensity 45
Figure 2.18 Variable Processing Parameter Power vs. Average Broadband Intensity..... 46
Figure 2.19 Variable Processing Parameter Power vs. Average 520 nm Intensity 48
Figure 2.20 Variable Processing Parameter Power vs. Average 530 nm Intensity 49
Figure 2.21 Variable Processing Parameter Velocity vs. Average Broadband Intensity . 51
Figure 2.22 Variable Processing Parameter Velocity vs. Average 520 nm Intensity..... 52
Figure 2.23 Variable Processing Parameter Velocity vs. Average 530 nm Intensity..... 53
Figure 2.24 Variable Processing Parameter Power Velocity Broadband Intensity Relationship 57

Figure 2.25 Variable Processing Parameter 520 nm Power Velocity Intensity Relationship 58
Figure 2.26 Variable Processing Parameter 530 nm Power Velocity Intensity Relationship 59
Figure 2.27 Error of Broadband Intensity Estimation 61
Figure 2.28 Error of 520 nm Intensity Estimation 62
Figure 2.29 Error of 530 nm Intensity Estimation 63
Figure 2.30 Variable Experiment Power and Velocity vs Line to Continuum 66
Figure 2.31 Summary of Effects on Trends by Varrying Power and Velocity 67
Figure 3.1 Big Little Experiment CAD Rendering 75
Figure 3.2 Big and Little Builds Removed from Build Plate 76
Figure 3.3 Scan Patterns of the Build 78
Figure 3.4 Diode Data for Broadband Layer 1 81
Figure 3.5 Separating Broadband Builds Layer 1 Raw Data 82
Figure 3.6 Separating Broadband Builds Layer 1 Tline 83
Figure 3.7 Separating Broadband Builds Layer 1 Noise Reduction 84
Figure 3.8 Separating Broadband Builds Layer 1 Separated Builds 85
Figure 3.9 Raw Spectral Intensity for Layer 1 520 nm and 530 nm 86
Figure 3.10 Separated Spectral Intensity for Layer 1 520 nm and 530 nm 86
Figure 3.11 Average Broadband Intensity per Layer 88
Figure 3.12 Average 520 nm Intensity per Layer 89

Figure 3.13 Average 530 nm Intensity per Layer 90
Figure 3.14 Average Line to Continuum Intensity per Layer 91
Figure 3.15 Big CT Porosity Analysis 92
Figure 3.16 Little CT Porosity Analysis 93
Figure 3.17 Big CT Pores per Layer 95
Figure 3.18 Little CT Pores per Layer 96
Figure 3.19 Big CT Pores vs Average Broadband Intensity per Layer 98
Figure 3.20 Little CT Pores vs Average Broadband Intensity per Layer 99
Figure 3.21 Big CT Pores vs Average 520 nm Intensity per Layer 100
Figure 3.22 Little CT Pores vs Average 520 nm Intensity per Layer 102
Figure 3.23 Big CT Pores vs Average 530 nm Intensity per Layer 103
Figure 3.24 Little CT Pores vs Average 530 nm Intensity per Layer 104
Figure 3.25 Big CT Pores vs Average Broadband Intensity Smoothed 106
Figure 3.26 Little CT Pores vs Average Broadband Intensity Smoothed 108
Figure 3.27 Big CT Pores vs Average 520 nm Intensity Smoothed 109
Figure 3.28 Little CT Pores vs Average 520 nm Intensity Smoothed 110
Figure 3.29 Big CT Pores vs Average 530 nm Intensity Smoothed 111
Figure 3.30 Little CT Pores vs Average 530 nm Intensity Smoothed 112
Figure 3.31 Broadband Top 500 Intensities for Big Layers 1-8 114
Figure 3.32 Broadband Top 500 Intensities for Little Layers 1-8 116

Table of Tables

Table 2.1 Material properties for Alloy 718 [38] 29

Table 2.2 Processing Parameters of Single Bead Experiment 30

Table 2.3 Original Constants of Harvey's Theorem 55

Table 2.4 Updated Constants of Harvey's Theorem 56

Table 2.5 Original and Adjusted Average Percent Error 64

Table 2.6 Original and Updated Coefficient of Determination R^2 Values 65

Table 3.1 Example of .csv file Format 80

Chapter 1 Introduction and Literature Review

1.1 Additive Manufacturing

Additive manufacturing (AM), also known as 3D printing is a manufacturing method that consists of building components and devices by thin layers or sheets. Due to its layer-by-layer approach, AM can have some significant advantages over traditional manufacturing techniques. One advantage is the ability to create complex structures that traditional manufacturing cannot. An example of a complex structure is a part with nonlinear internal piping or ventilation that cannot be machined by mills or other machining equipment. Another advantage that AM has over traditional manufacturing is wide range of materials that it can create parts from. Additively manufactured parts can be made from material such as metals, metal alloys, polymers, plastics, rubbers, ceramics, glass, concrete, biomaterial, and food [1]. AM can also uses these materials more efficiently. Since parts are build layer-by-layer, the amount of material used is significantly less than traditional subtractive manufacturing where materials need to be removed from a block of raw stock. Any leftover material in AM can typically be reused easily [2]. Because of these advantages, AM has found uses in many major industries around the world. Some of these industries include aerospace, automotive, machine tool production, healthcare, dental, architectural, retail, and food industries [3].

The process of creating an additively manufactured part begins with a designed model. Typically this is in the form of a computer aided design (CAD) solid model. The next step is to partition the model into a mesh of triangles. This is performed using computer software and the file types are commonly referred to as a stereolithography or standard tessellation language file (STL). Next, more software is needed in order to slice the model into the desired 2D cross-sections for the build. Once the model has been meshed and sliced, the information can be sent to the AM machine that will produce the parts layer-by-layer based on the geometry provided by each slice. Figure 1.1 displays the progression of an AM part from the designed CAD model to the final printed part.

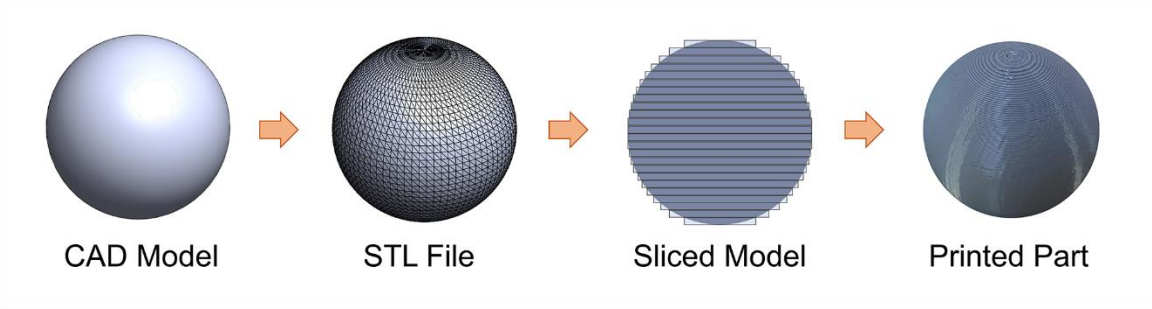

Figure 1.1 AM Part Progression from Design to Finish

The final printed parts can be subjected to many sorts of post processing techniques including surface machining, heat treatment, or polishing.

Seven major AM methods exist that can create parts in the layer-by-layer process above. These processes can have many names but in general are referred to as, binder jetting, direct energy deposition, material extrusion, material jetting, powder bed fusion, sheet lamination, and vat photopolymerization [4]. The AM method that will be focused

on in this work is a form of powder bed fusion known as laser powder bed fusion (LPBF).

1.2 Laser Powder Bed Fusion

LPBF is a metal based AM process that can produce highly complex and accurate parts with similar material properties to that of traditional subtractive manufacturing. It works by first spreading thin layer of powder material across a build platform. Then a laser energy source is directed by a mirror to scan the layer of powder which melts into the desired layer shape and solidifies when cooled. Next the build plate is lowered one layer thickness and a recoater blade spreads a new layer of raw powder material. This process is repeated until the part has been fully build [4]. Figure 1.2 displays a diagram of a LPBF system.

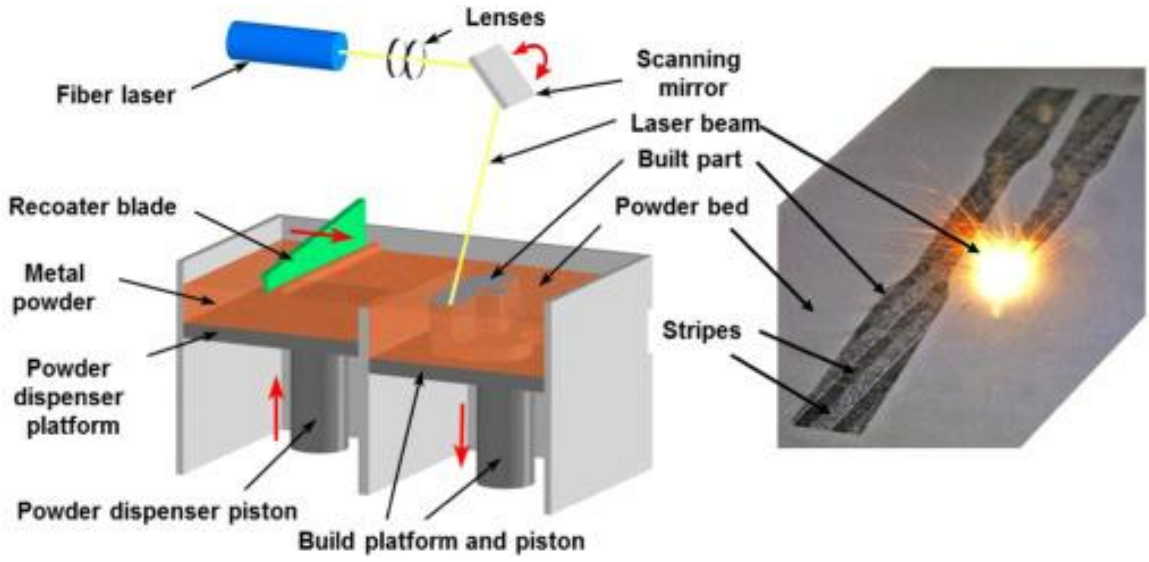

Figure 1.2 Laser Powder Bed Fusion System [5]

The entire process is contained inside a build chamber which control the atmosphere by introducing an inert gas such as argon or nitrogen to limit the amount of oxygen that can influence the high temperature reaction [6].

Once the LPBF part is complete and removed from the build plate it may go through a number of post processing techniques. Typical prost processing techniques for LPBF parts include machining (to remove solidified support material), surface finishing, polishing, chemical treating, and heat treatment. Heat treatment can be performed to remove residual stresses within the part, modify the microstructure of the material, or to remove porosity or other defects within the part.

1.2.1 Terminology in LPBF

1.2.1.1 Melt Pool

A melt pool forms at the reaction site of the laser and powder material as the laser heats the material and causes it to melt. As the laser continues to move the melt pool will move with it but will leave behind a trailing edge of melted material that is still solidifying. Figure 1.3 displays a model and cross-section of a melt pool in motion with trailing edge of solidifying material.

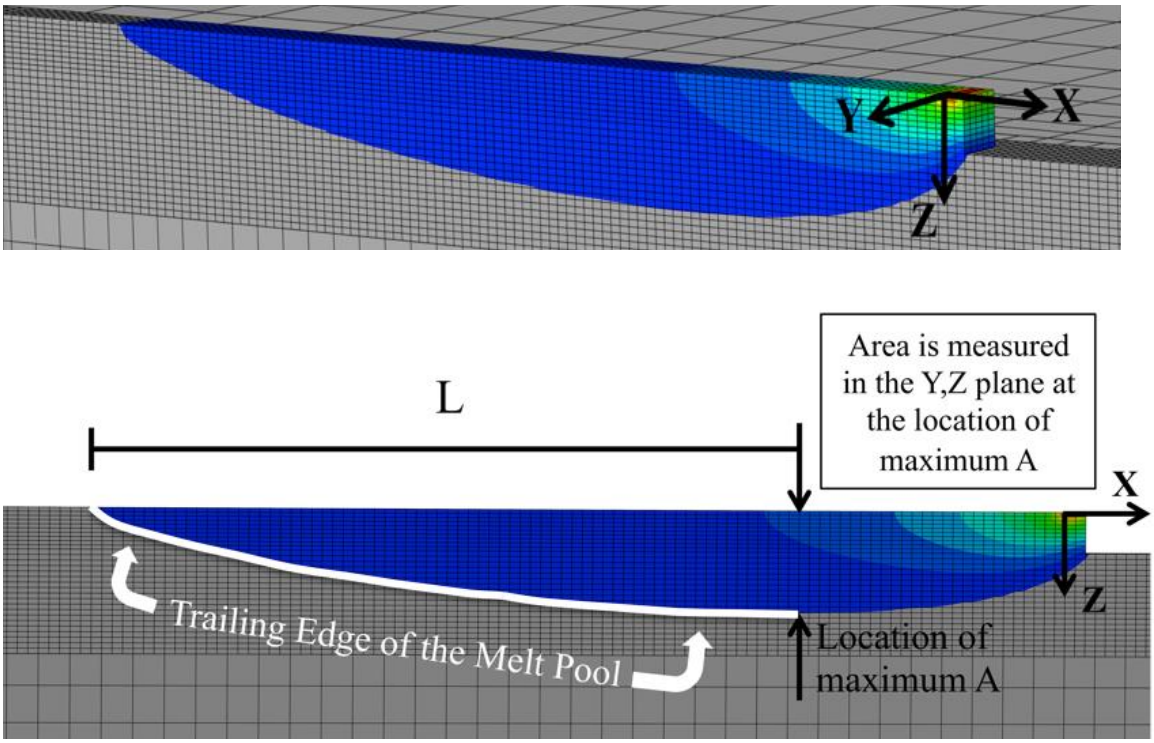

Figure 1.3 Melt Pool Model [7]

In Figure 1.3, the laser heat source is moving in the x-direction and the depth of the melt pool is in the z-direction. The length of the melt pool L follows behind in the x-direction and the "Trailing Edge of the Melt Pool" is the location at which the liquid material is cooling into a solid. A refers to the maximum cross-sectional area of the melt pool in the y-z plane and occurs at the maximum depth of the melt pool [7]. Understanding the melt pool shape and cooling rate is critical for creating reliable LPBF parts.

1.2.1.2 Plume

The plume is a phenomenon that occurs during the build process of LPBF that exists above the melt pool. The plume forms when the laser heats the powder material to the melting point. When this happens a metal vapor of the material is generated and

ejected from the melt pool area. This metal vapor will then interact with the melting laser creating a region of plasma radiation. When the plasma radiation interacts with the thermal radiation from the melting reaction, the byproduct is referred to as the plume. Figure 1.4 displays a computer vison process that filters out an image of a plume above a melt pool in a LPBF build.

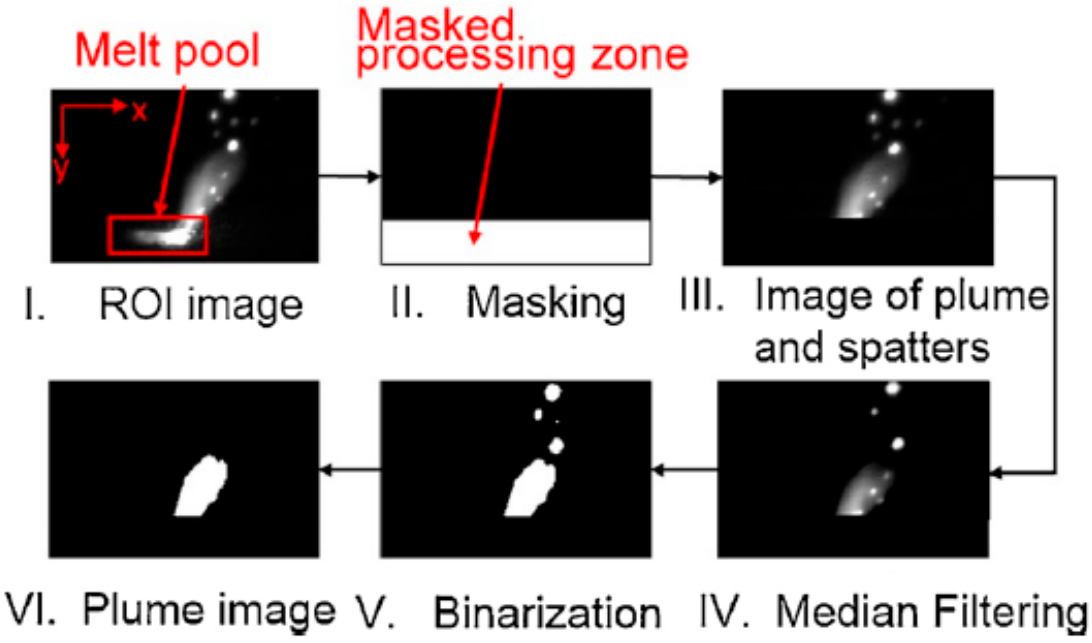

Figure 1.4 Computer Imaging of Plume Isolation [8]

Research and experiments are being conducted to measure certain characteristics of the plume with a variety of measurement methods and correlate them to defects [8]. The hope of this is to be able to in-situ monitor the plume and use the data recorded in real time to predict defects within the LPBF part.

1.2.1.3 Spatter

Much like the plume, spatter is a common reaction to the melting process of LPBF. Spatter refers to the particles of molten material that are ejected from the melt pool through the plume and away from the melting laser. It has been found that the cause for spatter in LPBF is the surface tension and recoil pressure of the melting and evaporating powder material also referred to as the Marangoni effect [9]. In addition, some experimental results show that the gas entrainment from Bernoulli's effect can also be considered as the cause of spatter [8]. Spatter has been found to increase the potential of defects of LPBF parts. As molten material lands on areas of non-melted powder the local thickness of the powder can change resulting in porosity or lack of fusion in the parts. This can be prevented with a controlled flow of inert gas such as argon or nitrogen in the build chamber that moves expelled spatter away from the build while simultaneously eliminating oxygen from the high heat reaction [9, 10]. Figure 1.5 displays the spatter being expelled from a LPBF build and them removed from the area by an inert gas flow.

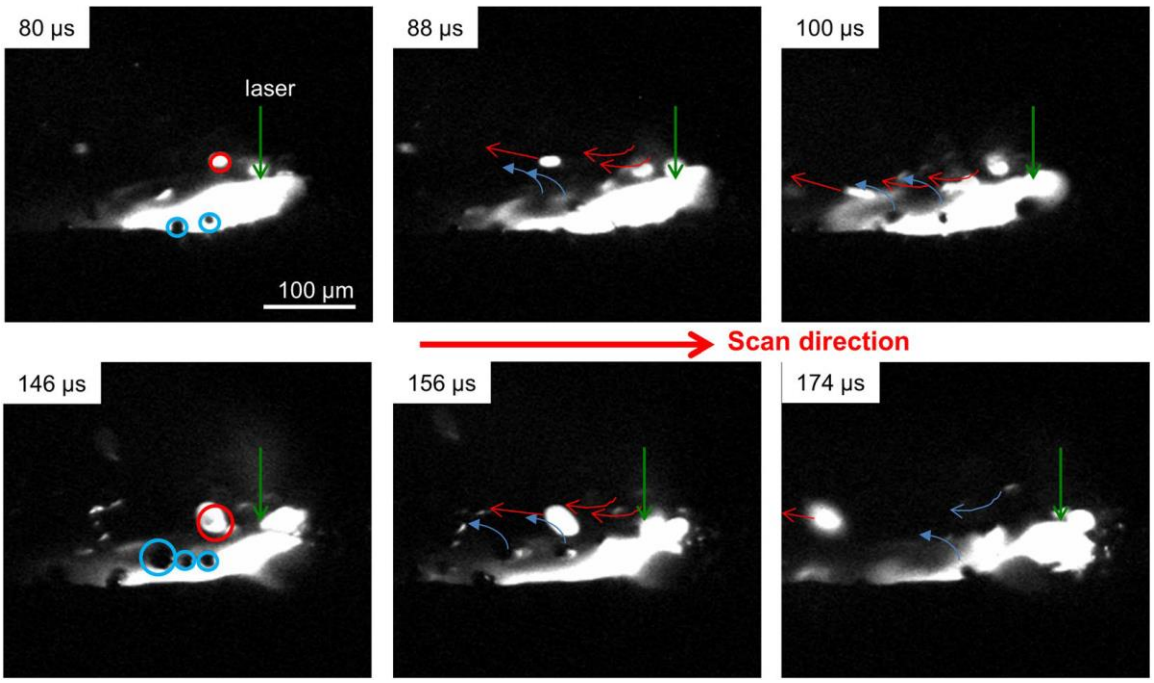

Figure 1.5 Spatter Expelled from Melt Pool and Removed by Inert Gas Flow [10]

In the images, the green arrow represents the laser melting location and the red and blue circles surround expelled hot and cold particles as they are removed from the melt pool area. Directional arrows were added in that trace the movement of some of the red and blue expelled particles respectively.

1.2.2 Microstructure

LPBF parts typically consist of columnar grains because of the rapid solidification process that occurs during the build. Columnar grains are elongated and are much more likely to cause failures than the more uniform equiaxed grains. Equiaxed grains typically occur when material has been subject to a heat treatment process. Figure 1.6 displays example geometries of columnar and equiaxed grains.

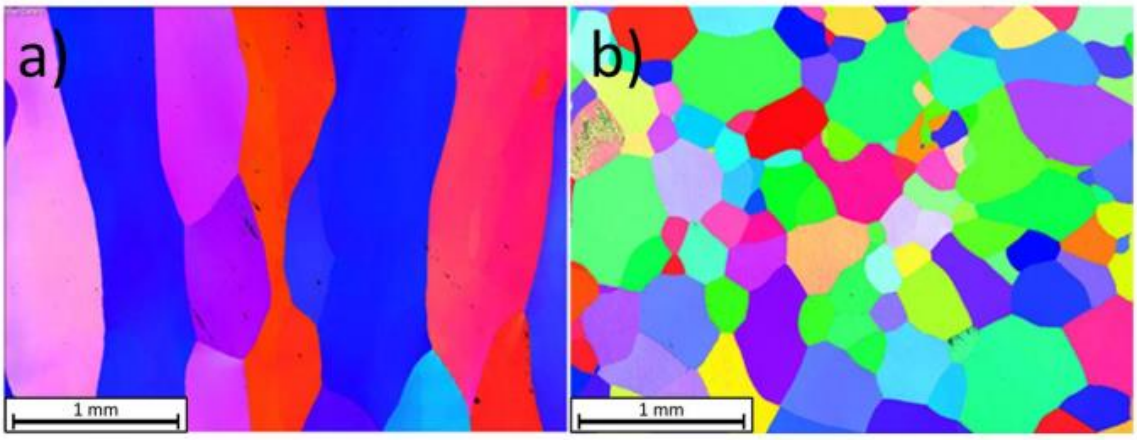

Figure 1.6 Microstructure for a) Columnar Grains b) Equiaxed Grains [11]

Cracks can develop along the long edges of columnar grains which will lead to potential defects and failures of the parts. Common practice to prevent this is to heat LPBF parts after they are build which recrystallizes the grains from columnar to equiaxed making the material much stronger and more reliable under loading. Before any sort of prost processing, larger LPBF parts will have shorter columnar grains since they will have a quicker cooling rate due to more material being able to convect the heat away compared to smaller parts which will hold their heat longer and continue develop their crystal structure.

1.2.3 Rosenthal Heat Transfer

The Rosenthal solution is 3D solution of the heat transfer for a traveling point heat source on a large group of material. This solution assumes that uniform material properties and a steady-state solution for the heat transfer [12, 13]. Figure 1.7 displays the 3D geometric representations of the Rosenthal solution.

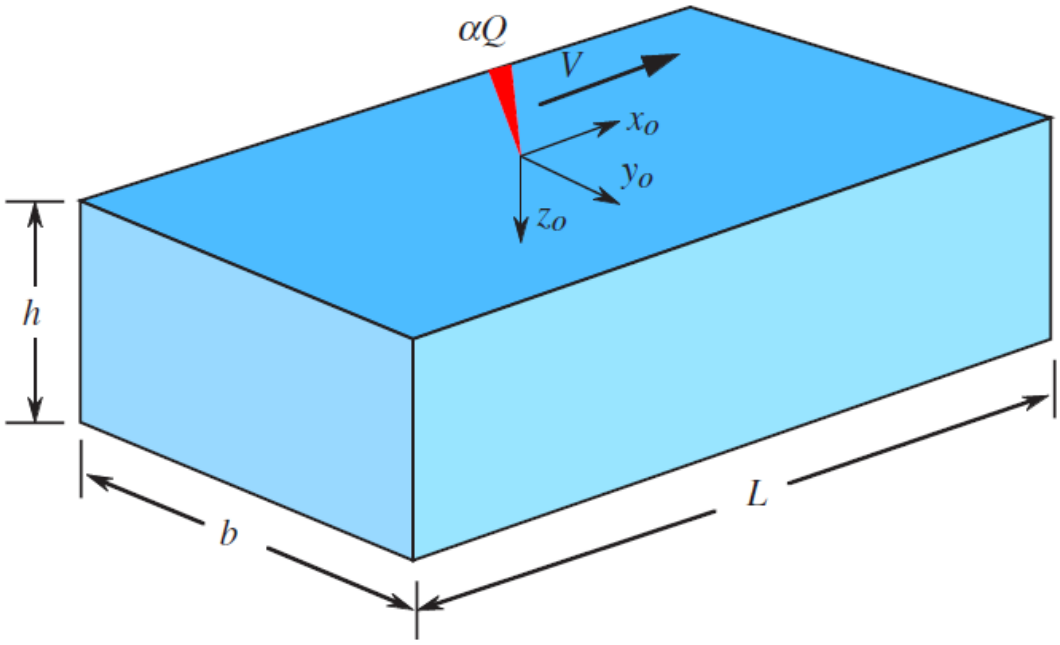

Figure 1.7 Geometry of Rosenthal Heat Transfer Solution [14]

Based on the geometry in Figure 1.7, the calculation of the dimensionless temperature $\bar{T}$ as a result of a point heat source traveling at a constant velocity is shown in Equation 1.1.

$$\bar{T} = \frac{e^{-\left(\bar{x}_0 + \sqrt{\bar{x}_0{}^2 + \bar{y}_0{}^2 + \bar{z}_0{}^2}\right)}}{2\sqrt{\bar{x}_0{}^2 + \bar{y}_0{}^2 + \bar{z}_0{}^2}}$$

Where the dimensionless coordinates $\bar{x}_0$, $\bar{y}_0$, and $\bar{z}_0$ are

$$\bar{x}_0 = \frac{x_0}{2k/\rho cv} \qquad \bar{y}_0 = \frac{y_0}{2k/\rho cv} \qquad \bar{z}_0 = \frac{z_0}{2k/\rho cv}$$

Equation 1.1 Rosenthal Dimensionless Temperature [15]

The dimensionless temperature $\bar{T}$ can also be written in the form

$$\bar{T} = \frac{T - T_0}{\left({}^{\alpha Q}/_{\pi k}\right)\left({}^{\rho c v}/_{2k}\right)}$$

Equation 1.2 Alternate Rosenthal Dimensionless Temperature [15]

In Equation 1.1 and Equation 1.2, T represents the temperature of interest, T_0 is the preheating temperature, α refers to the absorptivity of the laser heat source, Q represents the power of the laser, k is the thermal conductivity, ρ refers to the material density, c is the specific heat capacity, and v represents the velocity of the laser [15, 13]. The dimensionless cooling rate ${\partial \bar{T}}/{\partial \bar{t}}$ of the solidifying material can be determined through the differentiation of the Rosenthal solution and is shown in Equation 1.3.

$$\frac{\partial \bar{T}}{\partial \bar{t}} = \frac{e^{-\left\{(\bar{x}-\bar{t})+\sqrt{(\bar{x}-\bar{t})^2+\bar{y}_0{}^2+\bar{z}_0{}^2}\right\}}}{2\sqrt{(\bar{x}-\bar{t})^2+\bar{y}_0{}^2+\bar{z}_0{}^2}} \cdot \left\{1 + \frac{(\bar{x}-\bar{t})}{\sqrt{(\bar{x}-\bar{t})^2+\bar{y}_0{}^2+\bar{z}_0{}^2}} + \frac{(\bar{x}-\bar{t})}{(\bar{x}-\bar{t})^2+\bar{y}_0{}^2+\bar{z}_0{}^2}\right\}$$

Equation 1.3 Dimensionless Cooling Rate [14, 13]

1.3 Processing Parameters

A processing parameter in LPBF is a setting that can be modified by the machine or by a material property for any individual build. The five most common processing parameters in LPBF are laser power, laser velocity, layer thickness, hatch spacing, and the scan pattern [16]. The laser power processing parameter refers to the power that the laser will be set to in order to properly melt the powder material, typically in watts (W). Laser velocity refers to the speed at which the laser scans the individual layers to create the 3D part, typically measured in millimeters per second (mm/s). The layer thickness refers to the amount of powder that will be spread across the build platform each time a

layer has finished being scanned and a new layer needs to be melted. The typical measurement for layer thickness is micrometers (µm) and can be influenced by the material properties such as the powder particle size. Hatch spacing refers to the distance between side-by-side laser paths also measured typically measured in µm. The laser scan pattern processing parameter is the pattern in which the laser sweeps across and fill in the 2D geometry for that layer of the LPBF build. Figure 1.8 displays a diagram of each of the major processing parameters used in LPBF.

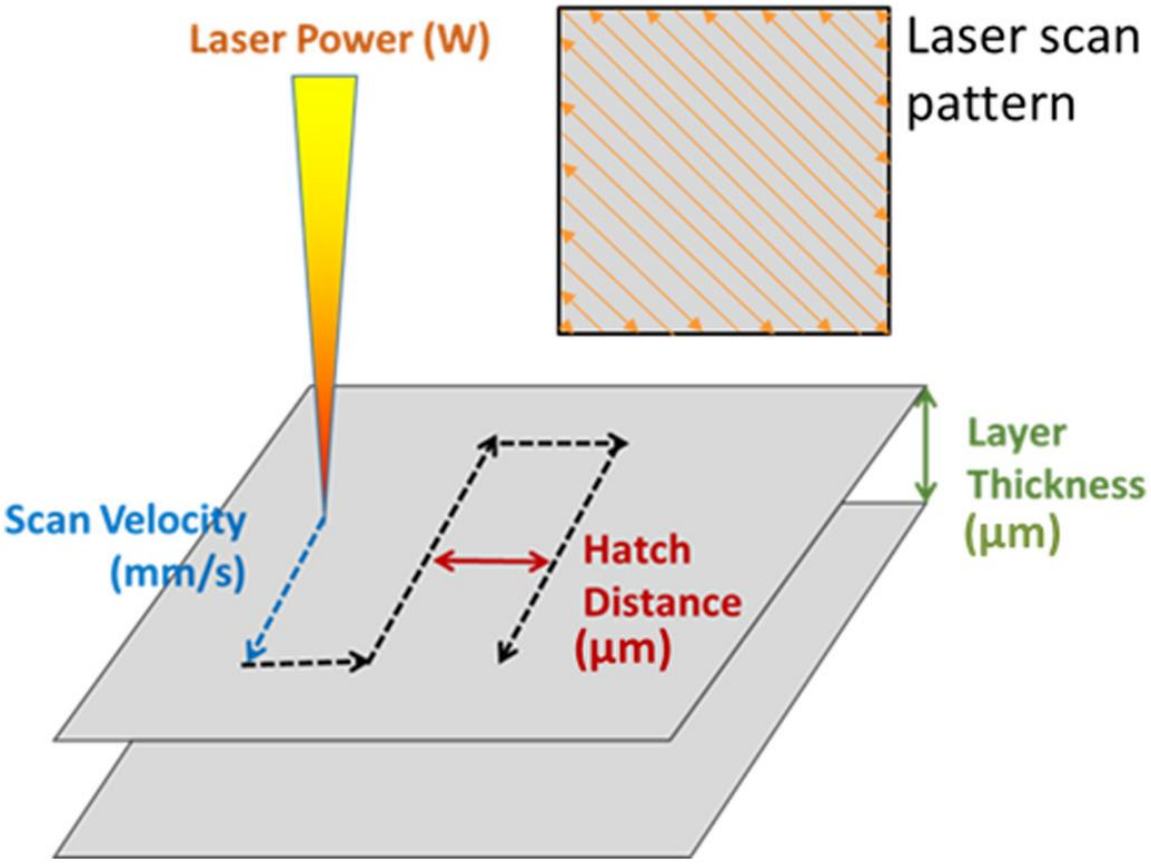

Figure 1.8 Common Processing Parameters in LPBF [16]

The two processing parameters that are focused on in this thesis are the power and the velocity of the laser. These two parameters are the main focus because they have been

found to influence the quality of LPBF parts more than the others and are typically the easiest parameters to change [17].

1.4 Post Processing

1.4.1 Hot Isostatic Pressing

One methods of post processing in LPBF is hot isostatic pressing (HIP). HIP is a material treatment process that applies extreme temperatures up to thousands of degrees Celsius inside of a pressure chamber, filled with an inert gas, which applies uniform or isostatic pressure up to hundreds of MPa to the parts. A typical HIP system is shown in Figure 1.9.

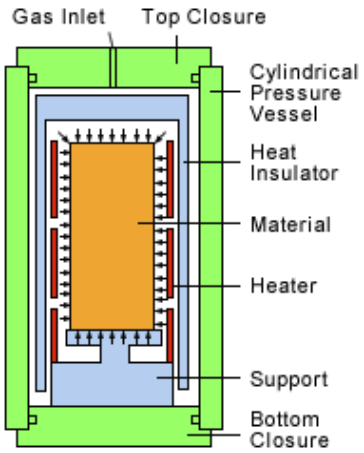

Figure 1.9 Common HIP Device [18]

The method of HIP has been proven to significantly increase the strength and fatigue life of parts since it closes and seals pores and other inherent defects within LPBF made parts by allowing the microstructures to grow to more equiaxed grains. Closing

pores and other defects reduces the number of potential crack initiation and growth locations within the LPBF parts [19]. Since HIP applies uniform pressure, the LPBF parts can maintain their initial geometries compared to some common hot pressing methods which apply uniaxial pressure with a press. The ability to eliminate internal defects and maintain the initial shape are why HIP has become commonplace in many LPBF post processing routines.

1.4.2 Other Post Processing

Machining is a common post processing technique for LPBF parts. Machining a LPBF part can help the part maintain critical tolerances, add specific threading, or add other critical features. It can also be used to remove support material that was added to the build during the print. Machined off support material has been found to maintain material properties at the connection sites once they are removed compared to common breakaway support material which leave rough surfaces and potential crack initiation sites [20].

Many other post processing techniques focus on surface finishing of the LPBF parts. Typical surface finishing methods include polishing, shot peening, and chemical soaking. A newer method being developed is laser surface finishing LPBF. Scanning the finished part's edges with a laser has been found to improve surface conditions and prevent surface crack formation [21].

1.5 Defects in Additive Manufacturing

Defects, especially pores, present within AM builds have been found to reduce the effectiveness and decrease the fatigue life of the printed parts. These pores have been

found to contribute to internal cracks initiation and crack growth, especially in metal additive parts [22]. Most defects in AM can be attributed to improper build conditions, material variations, and processing parameters. Since defects are known to be correlated with a reduction in the fatigue life of the AM part [22], it is important to reduce or eliminate these defects in order to obtain proper quality of AM parts. Even if the number of defects are reduced, it is still important to be able to confidently know if a printed part contains any defects before it is put into use.

1.5.1 Defects in Laser Powder Bed Fusion

Most of the defects found in LPBF are direct results of incorrect processing parameters or material purity. Proper power and velocity of the laser are critical in LPBF AM. Too much or too little laser power as well as too fast or too slow laser velocity will lead to defects in the finished parts [23]. Material conditions such as the powder layer thickness, melting temperature, and powder particle size can also lead to defects if not properly considered for the most optimum build. Some common defects in LPBF consist of lack of fusion, balling, and keyholing.

Lack of fusion occurs when side by side beads of the build material are not fully melted together causing internal gaps in the finished part. It typically occurs when the scanning velocity of the laser is high and the power of the laser is too low to fully melt the scan pattern. It can also be influenced by a hatch spacing being too large. Figure 1.10 displays the presents of lack of fusion in a LPBF build.

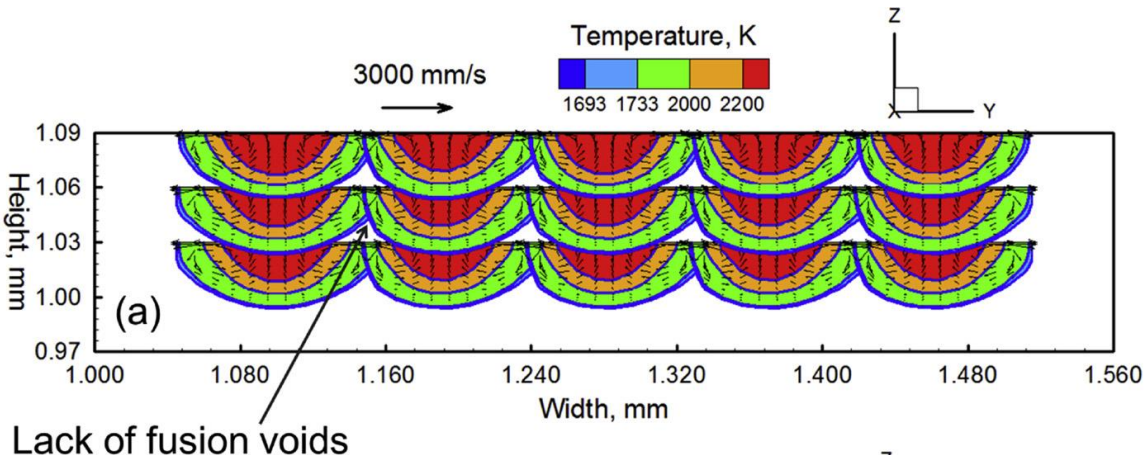

Figure 1.10 Lack of Fusion of a LPBF Build [24]

Balling occurs when the scan speed of the laser is too fast which causes the melt pool to not penetrate deep enough into the material resulting in gaps of un-melted material between layers of the build.

Keyholing porosity occurs when the power of the laser is too high or the scan speed is too low resulting in pores build beneath the surface i.e. too much energy is transferred into the material. Figure 1.11 displays the results of an experiment in which two scenarios of a LPBF spot weld recorded visually using high speed x-ray imaging in real-time. For test case **a**, the laser power was set to proper quantity and for test case **b**, the laser power was set to much higher with the goal of causing a defect. Both cases were recorded by high speed x-ray to monitor the reaction [25].

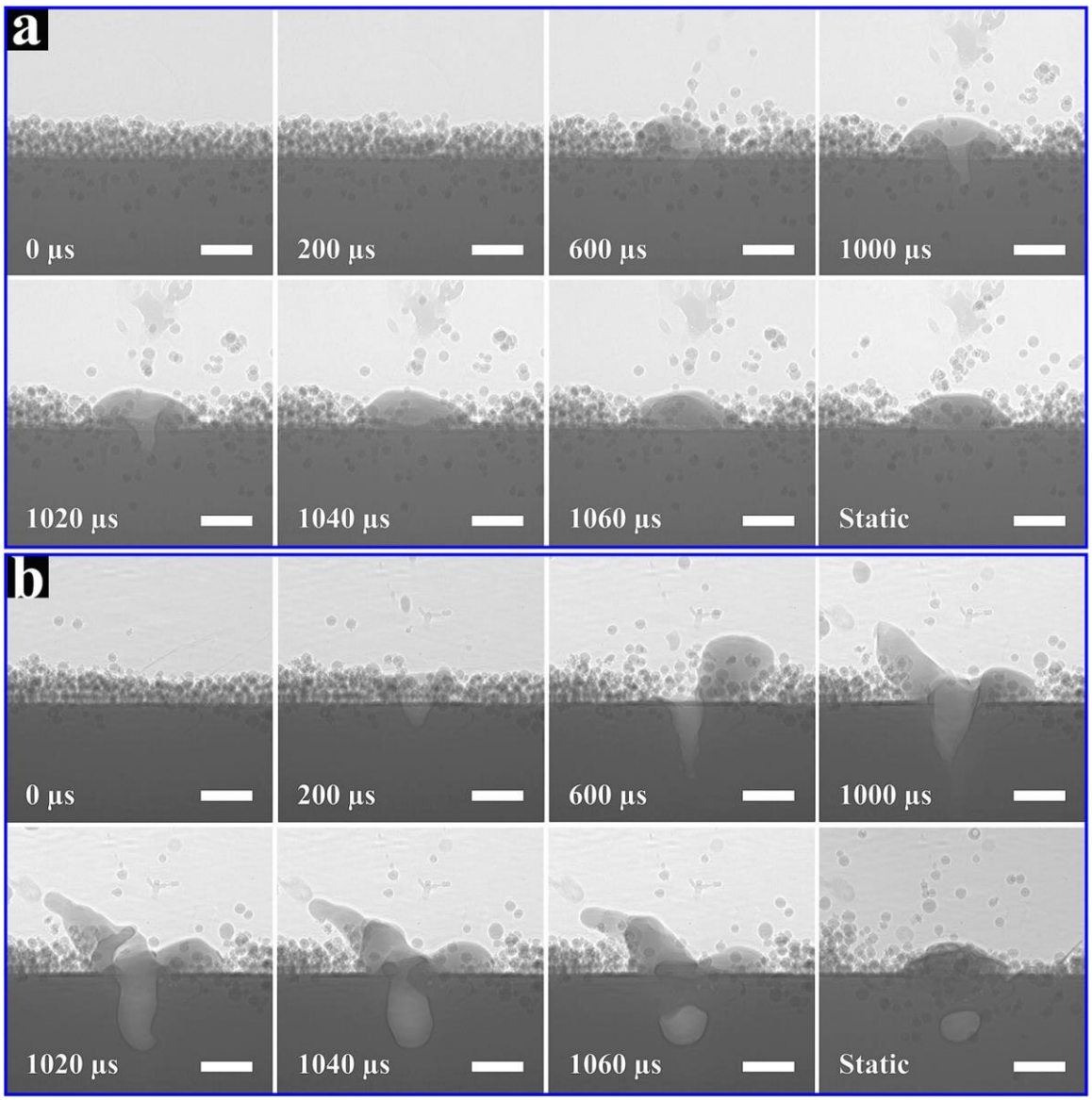

Figure 1.11 LPBF with High Speed X-Ray Monitoring [25]

In Figure 1.11 it is clear that the result of test case **a** show a good weld with no apparent defects within the build. The result of test case **b** show a void that developed below the surface of the build layer which is visual representation of keyholing.

Figure 1.12 displays a summary map of common LPBF defects as they relate to the laser power and velocity processing parameters.

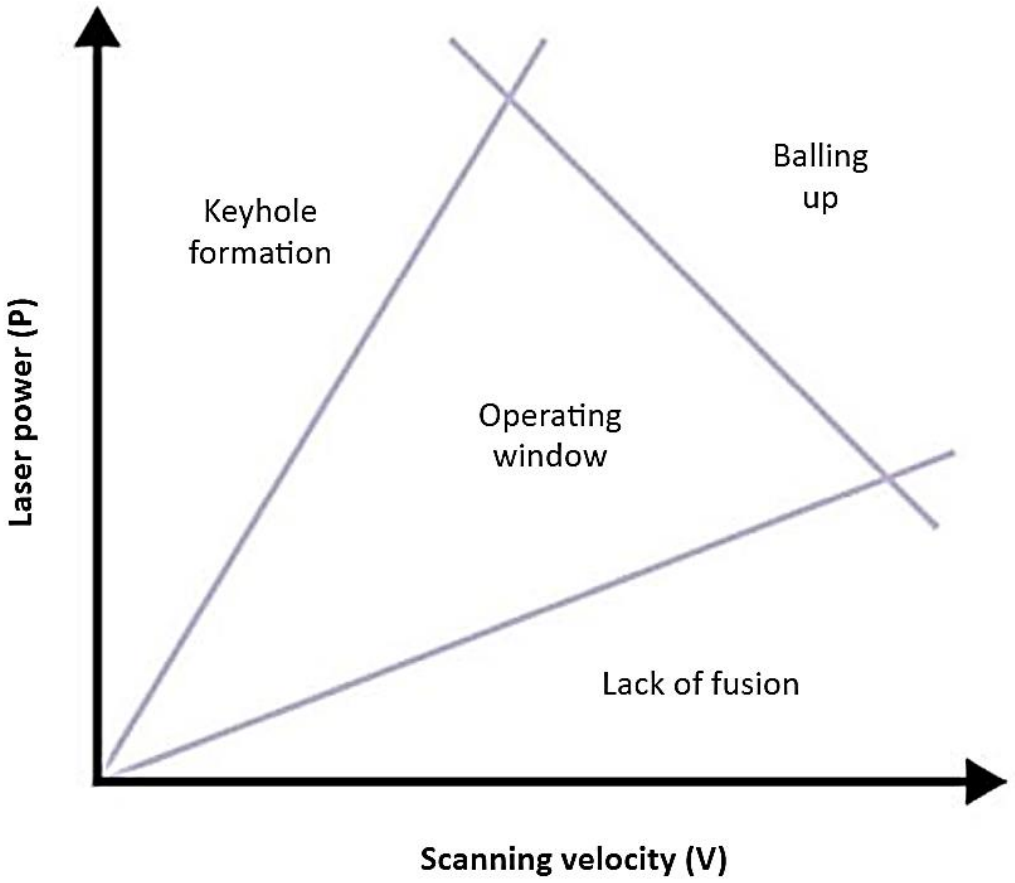

Figure 1.12 LPBF Defect Categorization by Processing Parameters [26]

When setting up the processing parameters for a LPBF build, the key is to balance the two to keep the melting within the operating window.

1.6 Defect Detection

Detecting defects within LPBF parts is a critical step in the manufacturing process. If a part containing defects is released to perform as intended the possibility of component failure is much higher and could result in catastrophe. Defects within a LPBF

build can be found either during the build with in-situ monitoring methods or after the build is completed.

1.6.1 Post Build Defect Sensing

1.6.1.1 CT Scanning

One common way to detect defects and pores of finished LPBF parts is computed tomography (CT) scanning. CT scanning is a technique that utilizes x-ray images taken from multiple different angles to generate a 3D model of desired information. CT scanning can detect voids and other defects within a LPBF parts. Figure 1.13 displays the results of a CT scan of a LPBF part.

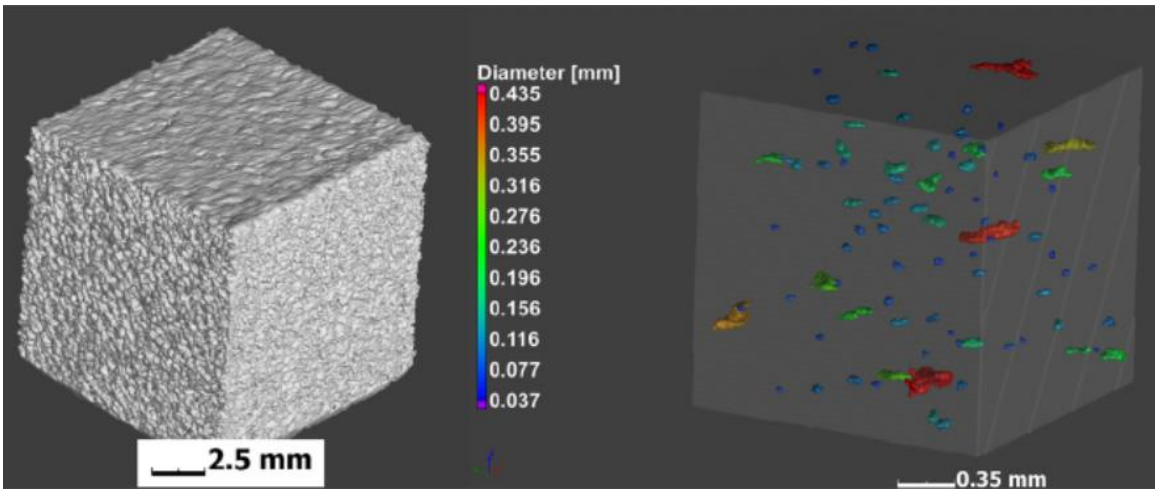

Figure 1.13 CT Scan of LPBF Part [27]

CT scanning has the ability spatially locate voids within the LPBF parts as well as measure the size of the voids. A few issues with CT scanning LPBF parts is that the process is time consuming and often expensive. Because of this, faster methods and the

ability to predict defects present in LPBF parts as they are being build has been the focus of a lot of recent research.

1.6.2 In-situ Defect Sensing

A variety of sensing techniques can be utilized to predict the presence of defect forming conditions during the build. These sensing techniques can be broken down into two classification; local and global sensing. Local sensing techniques typically evaluate conditions in real time that deal with part quality such as the melt pool geometry, plume, or spatter. Local sensing devices include high speed video, photo detectors, spectrometers, and thermal imagers. Global sensing techniques typically evaluate conditions layer-by-layer and deal with build area, build geometry, flatness, and volumetric defects. Global sensing devices include high resolution imaging, laser line scanning, and thermal imagers [28]. Figure 1.14 shows a matrix that classifies different local and global sensors as well as what they are able to measure [29].

Process Observation	Sensor	Defect Type					
		Process Deviation	Distortion	Geometry	Bed Flatness	Metallurgical	Volumetric Defects
Local	High Speed Video	Defect Generation Understanding					
	Thermal Imaging					X	X
Global	High Resolution Imaging		X	X	X		
	Laser Line Scanner		X	X	X		
	Thermal Imaging					X	X
	Photogrammetry (UNCC)		X	X			
	Projection Moiré (UNCC)		X	X	X		

EWI

Figure 1.14 Sensing Methods Matrix for LPBF [29]

High success rates have been recently found for predicting defects based on in-situ monitoring a LPBF build with the use of a local sensing method of high speed pyrometry [30]. Pyrometry is a measurement method that determines temperature based on radiation emitted from a particular system or reaction.

1.6.2.1 Spectroscopy

Spectrometers are instruments that measure intensities of light within an observable spectrum. During a build in LPBF the plume of radiation is emitted at the melt location and has been found to correlate with the process quality of the laser melting. Diodes can be used to analyze the radiation given off by the plume by measuring the various types of waves that pass through the plume using a grating or prism technique [31].

Spatially resolved acoustic spectroscopy (SRAS) is being researched as a nondestructive in-situ method for defect detection in LPBF. SRAS has been used in the past to determine surface roughness, grain size and orientation information within metals. The process of SRAS consists of two lasers. One laser generates surface acoustic waves (SAW) onto the build through a grating and a second laser collects the perturbation caused by the wave which enables the surface of the part to be mapped [32].

More recent work has shown that spectroscopy, when utilized in LPBF can have a relatively high success rate when predicting defects in certain materials and certain build conditions. The scenarios that had the most success in predicting defects in LPBF were Inconel material builds that had some sort of overhanging feature [33].

Spectroscopy can also be used to determine the temperature of a material based on the radiation it gives off which can be useful for determining some properties in LPBF. Temperature and the wavelength intensity of radiation are known to have an inverse relationship based on the principals of Wien's Displacement Law [34]. Based on an in-situ spectroscopy reading, the temperature of the LPBF process can be calculated to determine if defect inducing scenarios are occurring in the build.

1.6.2.2 Line to Continuum Ratio

The line to continuum ratio is a published LPBF in-situ collected spectroscopy data analysis procedure. The modified ratio consists of spectroscopy readings taken at two different wavelengths to reduce noise and better identify anomalies. The calculation for the line to continuum ratio is shown in Equation 1.4. The line to continuum ratio is intended to relate to the electron temperature and energy density of the processing parameters. Readings of the line to continuum ratio have been found to directly correlate to the number of pores within a LPBF part [35].

$$S_{Line-to-Continuum} = \frac{S_{520nm} - S_{530nm}}{S_{530nm}}$$

Equation 1.4 Line to Continuum Ratio [35]

In Equation 1.4, S_{520nm} refers to the measured spectral intensity at the 520 nm wavelength and S_{530nm} is the measured intensity at the 530 nm wavelength.

1.7 Thesis Contributions

In this research, spectroscopy was used to monitor the build chamber of a LPBF build during the print to determine if anomalies in the recorded data correlate to defects located within the LPBF parts.

1. Investigated the effect processing parameters have on in-situ collected spectroscopy data during a single bead LPBF print.
2. Developed a formula for estimating spectral intensity given off during a LPBF build based on processing parameters.

3. Identified the effect of geometry on spectral intensity collected in-situ during a LPBF build.

4. Manipulated raw spectroscopy data to investigate correlation between anomalies and defects with LPBF parts.

Chapter 2 Effects on Spectroscopy Data of LPBF Single Beads with Varied Processing Parameters (Variable Experiment)

2.1 Introduction

An experiment was created with the goal of determining the effects of processing parameters of LPBF on spectroscopy intensity during a build. A series of fifteen individual single bead welds were printed, each with varying power and velocity of the laser. During the builds, a system consisting of three diodes was used to collect intensities of different wavelengths. Changes within these data sets is hypothesized to correlate directly to the variations in the processing parameters. These changes and the measured intensities are used to develop a rough equation of estimated spectral intensity given off by a LPBF build at a given processing parameter set. The experimental results found in this experiment will also be compared to the line to continuum for each of the processing parameter combinations to determine the similarities between the results of the two methods.

2.2 Theory

Theory suggests that there is a direct correlation between spectral intensity spikes and defects within LPBF printed parts. In order to understand what would qualify as a spike in the spectral intensity data, a baseline or control set of values would have to be obtained. A function of estimated spectral intensity could be derived with its inputs being the power and velocity processing parameters which would help to develop models that

identity when an anomaly has occurred. If these models continue to develop, scientists will be able to determine immediately or at least be able to examine precise locations within the build for defects based on the correlating intensity spikes recorded when that section was printed.

The effects on the cooling rate of the material are also impacted by the power and velocity processing parameters. Since the power is related to the length of the melt pool, as it decreases across cases the cooling rate should increase since the melt pool size decreases. Similarly, as the velocity increases, the melt pool depth will decrease resulting in a smaller melt pool cross-sectional area that will also increase the cooling rate.

2.3 Experiment Setup

2.3.1 Build

The build for this experiment consists of fifteen individual weld bead segments approximately 0.4243in in length printed on a 1in by 1in build plate. Figure 2.1 displays a CAD rendering of the build plate and the weld bead lines as well as the dimensional locations of each of the fifteen print locations in inches.

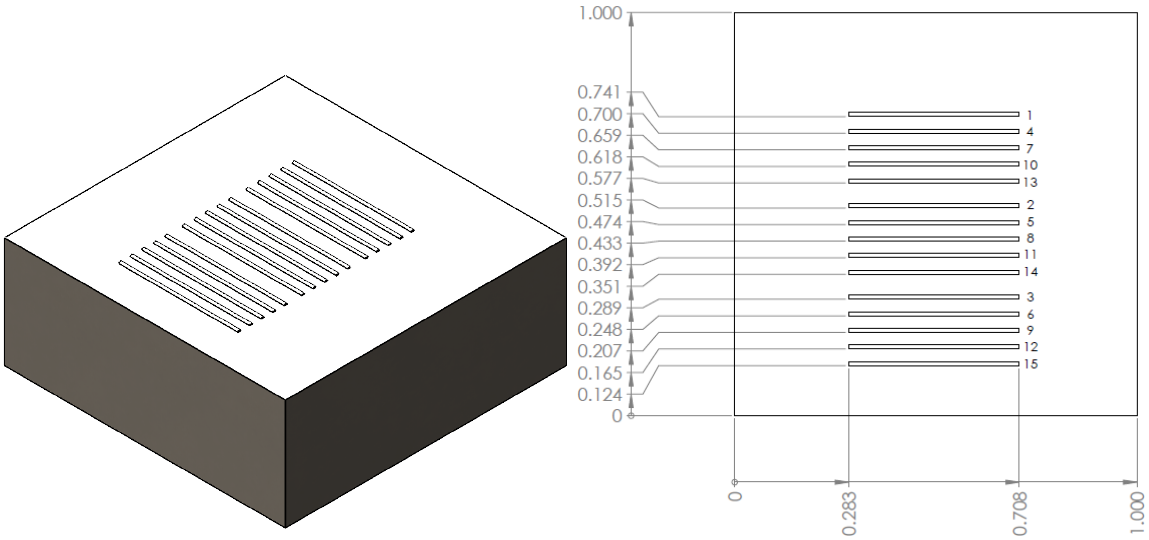

Figure 2.1 Variable Experiment Build Plate CAD Renderings

The numbers displayed on the right side of the weld bead lines in Figure 2.1 represent the order that the weld beads were printed in. They were printed in this way as to not have the line that is currently printing affect the solidification of the line that was printed previously. Each of the lines were printed left to right inside the LPBF machine and the adjustments made to the processing parameters were made as the machine moved its laser from the end of a printed line to the start of the next. An image of the completed build is shown in Figure 2.2.

Figure 2.2 Variable Experiment Build Plate Photograph

One thing to note in the image of the build are the singe marks located on the build surface that were left as a result of spatter from the printing process expelling small particles into the air of the build chamber.

2.3.2 Machine

The machine used to print the series of individual bead welds is an early adaptation of the Open Additive PANDA laser powder bed fusion machine developed at Universal Technology Company, LLC where the experiments for this work were performed. These particular machines are outfitted with an adjustable laser up to 500 W and has a build volume of 4in by 4in by 2in. Figure 2.3 shows an Open Additive laser powder bed fusion machine similar to the machine that the individual weld beads were printed in.

Figure 2.3: Open Additive PANDA LPBF Machine [36]

The Open Additive machine shown in Figure 2.3 would also be equipped with an assortment of diodes monitoring the intensity of the build chamber and collecting data as the machine prints. The system of diodes would be recording the intensity for multiple wavelengths during the build.

2.3.3 Material

The material that was used for the individual weld beads is nickel super alloy 718 powder. Alloy 718 is a nickel-chromium alloy that typically consists of a high chemical purity, low porosity, high stacking density, and flows very easily [34]. The previously

listed properties are why this material is very common in powder based additive manufacturing process due to its fine powder particles and its material properties after it is printed [37]. Table 2.1 lists some of the mechanical properties of alloy 718.

Table 2.1 Material properties for Alloy 718 [38]

Property	Value
Density	$\rho = 7451\ {}^{kg}/_{m^3}$
Specific Heat Capacity	$c = 600\ {}^{J}/_{kg \cdot K}$
Thermal Conductivity	$k = 26.6\ {}^{W}/_{m \cdot K}$
Melting Temperature	$T_m = 1610\ K$

2.3.4 Spectroscopy

Three diodes were used to collect spectral intensity readouts throughout this experiment of different wavelengths. One of the diodes was left without a filter resulting in the ability to measure the intensity of the visible broadband light spectrum. The other two diodes have filters on them pertaining to the 520 nm and 530 nm wavelengths. These two wavelengths were chosen because the material, Inconel 718, has a high chrome composition percentage and 520 nm and 530 nm filters capture the chrome intensity peaks when alloy 718 is melted [39]. The data collected by these diodes were exported into a csv file for later analysis.

2.3.5 Processing Parameters

The processing parameters pertaining to each of the fifteen individual lines are shown in Table 2.2 below.

Table 2.2 Processing Parameters of Single Bead Experiment

Print Line	Power (W)	Velocity (mm/s)
1	450	500
2	450	1000
3	450	1500
4	375	500
5	375	1000
6	375	1500
7	300	500
8	300	1000
9	300	1500
10	225	500
11	225	1000
12	225	1500
13	150	500
14	150	1000
15	150	1500

Each of the machine the power values were kept constant for three beads before being stepped down by 75 W for the next group of prints. The velocity would quickly be modified by the LPBF machine in between lines as the print location was moved from the end of the pervious line to the start of the next. Figure 2.4 shows the location of each of the single bead prints as well as the processing parameters combination used to print it. All fifteen of the individual lines were printed left to right.

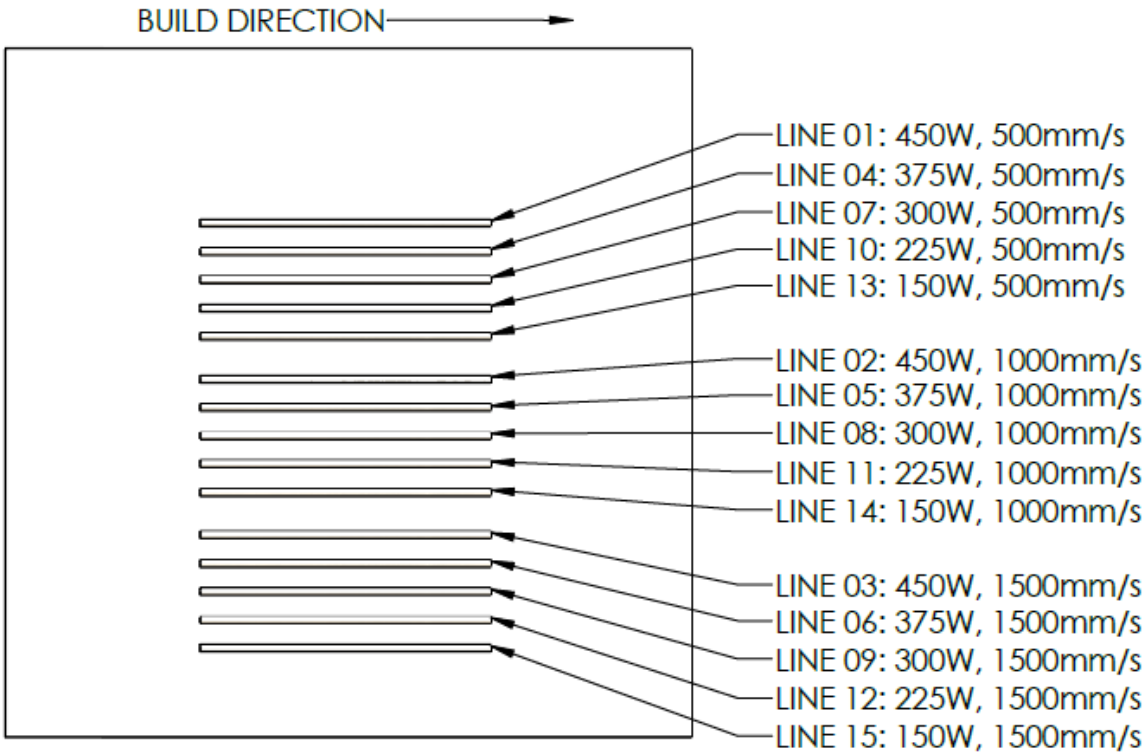

Figure 2.4 Variable Experiment Build Parameters

2.4 Analysis

The analysis of the fifteen individual lines consisted of the following process. The spectroscopy data relating to the printing was isolated from all of the non-printing data and saved into individual sets. Then, each of the print sets was analyzed for the individual properties such as average value and standard deviation based on normal distributions. Lastly, the average values were used to generate a function that returns the average intensity values based on the processing parameter inputs (power and velocity). This formulation was generated using all three of the spectral intensity wavelengths measured during the printing.

2.4.1 Cooling Rate Calculation

Using Equation 1.1 and Equation 1.3, the Rosenthal cooling rates were calculated for each of the power and velocity processing parameter combinations used in this experiment. Figure 2.5 displays the calculated Rosenthal cooling rates as a function of the normalized melt pool depth.

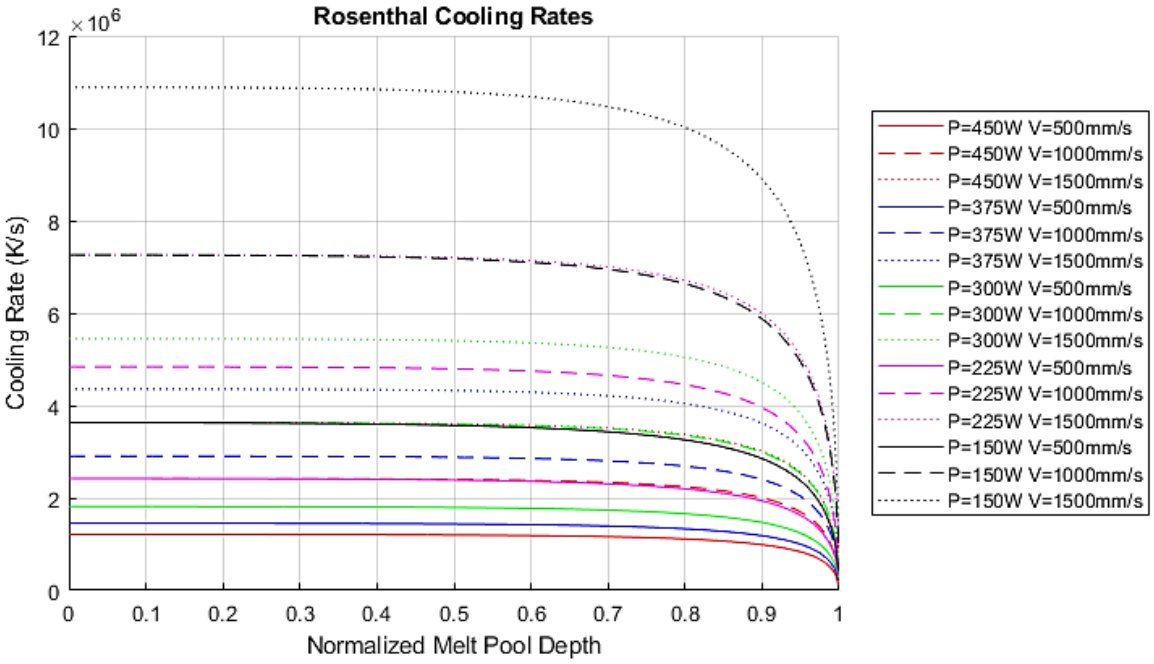

Figure 2.5 Variable Experiment Cooling Rate vs. Normalized Melt Pool Depth

Based on Figure 2.5 it appears that in general, the cooling rate increases as the power decreases. Reducing the power processing parameter will result in less melted material which will solidify faster. It also appears that the cooling rate will increase as the velocity processing parameters increases. As the velocity increases, the melt pool depth will decrease also resulting in less melted material which will cool faster.

2.4.2 Isolating Build Intensity Data

To isolate the intensity data pertaining to only one single bead, the broadband intensity data is used. The broadband is used because the sections of non-build and build data are much more defined. Figure 2.6 shows the raw data for the broadband intensity data.

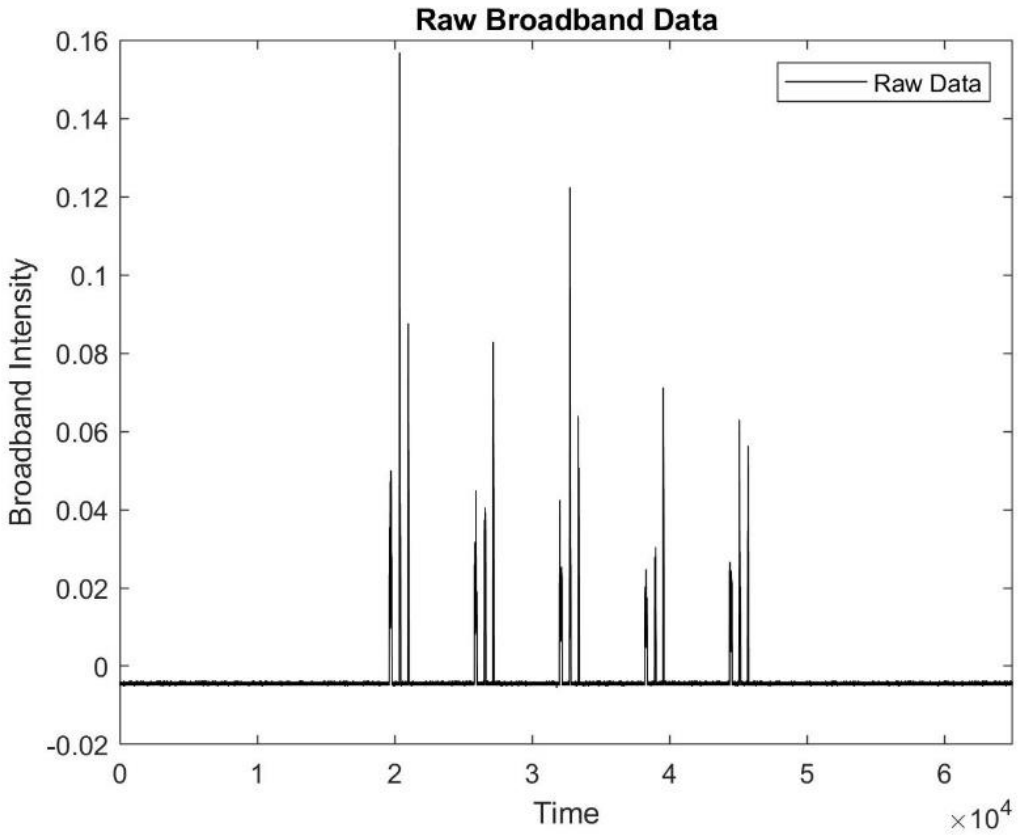

Figure 2.6 Variable Processing Parameter Raw Broadband Intensity Data

Examining Figure 2.6, it is clear to see the fifteen individual locations pertaining to the printing locations apart from the non-printing sections. Since the intensity spikes are well defined the start and end points could be easily found and recorded. These start and end points were used later to analyze the 520 nm and 530 nm data sets since their start and

end points are less defined. Figure 2.7 shows the raw data for 520 nm and 530 nm wavelengths with the start and end points less defined because of noise recorded by the diodes when the laser is not printing.

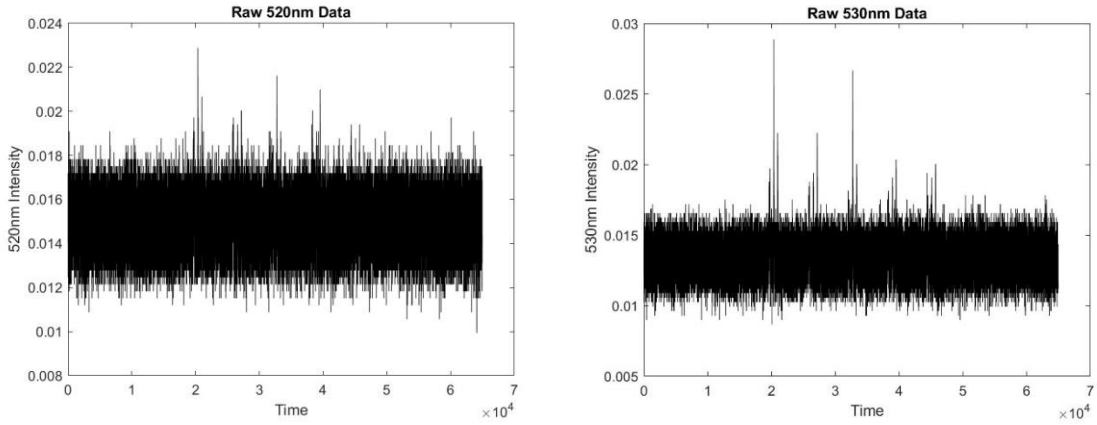

Figure 2.7 Variable Processing Parameter 520 nm and 530 nm Raw Intensity Data

Once the start and end points were found for the broadband data sets, they were used to isolate the printing locations of the broadband, 520 nm, and 530 nm spectral intensity sets. Figure 2.8 shows the spectral intensity data from each of the fifteen individual weld beads of the broadband data based on their processing parameters.

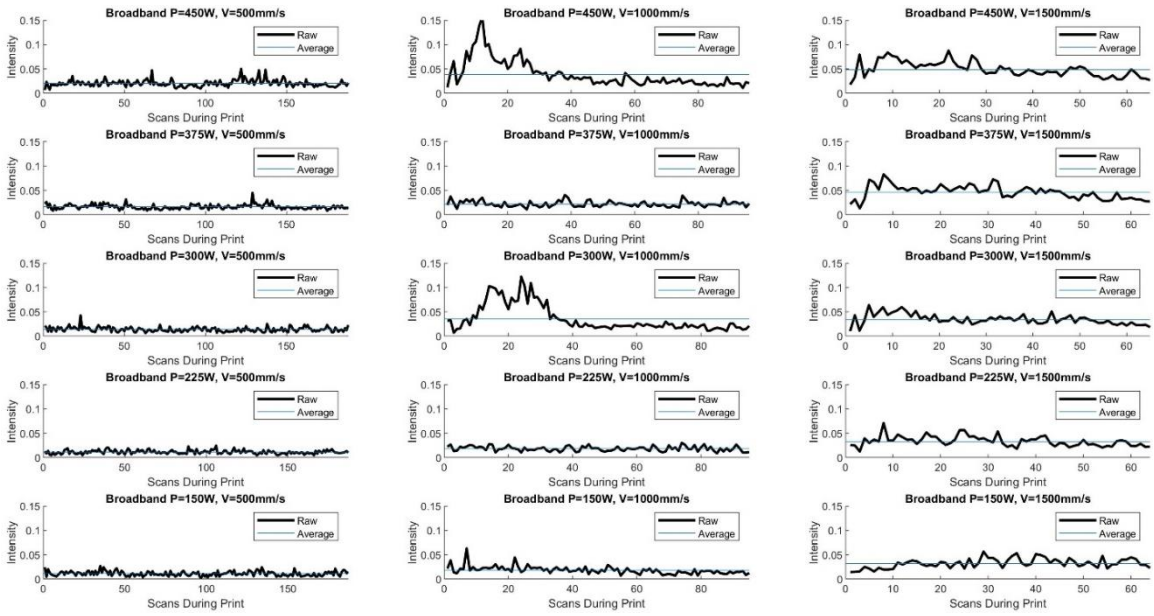

Figure 2.8 Variable Processing Parameter Original Broadband Build Data

A general trend can be observed in Figure 2.8. As the power increases across the processing parameter cases, in general the intensity is higher. This is due to the fact that increasing power increases the amount of total energy in the system which while being dissipated as heat or light, can be observed as a higher intensity measured from a spectral diode. The same trend of increasing intensity can be observed as the velocity increases however, intuitively, increasing the velocity should decrease the amount of total energy in the systems which should lower the intensity captured by the diode.

Within two of the data sets shown in Figure 2.8 however, large intensity spikes can be observed. The two spikes occur in the P=450 W, V=1000 mm/s and P=300 W, V=1000 mm/s weld bead data. These two spikes fall outside of the general trend however, the majority of the lines in Figure 2.8 fall into the trend previously described. Because of this, the two data sets that show these intensity spikes would be modified for

future calculations. This modification consisted of considering only the second half of the data sets because they appear to follow the same trend of the rest of the data sets in the broadband spectrum and would eliminate some of the error caused by the large spikes in the data. These appears to be no visible reason that these two beads contain spikes in the intensity data. Further investigation is required to determine the cause of the spikes.

Considering only the second half of the P=450 W, V=1000 mm/s and P=300 W, V=1000 mm/s intensity data sets does eliminate a significant amount of information, however, the remainder of both sets still include at least forty-five intensity readout data points which is adequate enough for much of the calculation in this experiment. Figure 2.9 shows the spectral intensity data from each of the weld beads of the broadband data with the updates to the P=450 W, V=1000 mm/s and P=300 W, V=1000 mm/s intensity data sets.

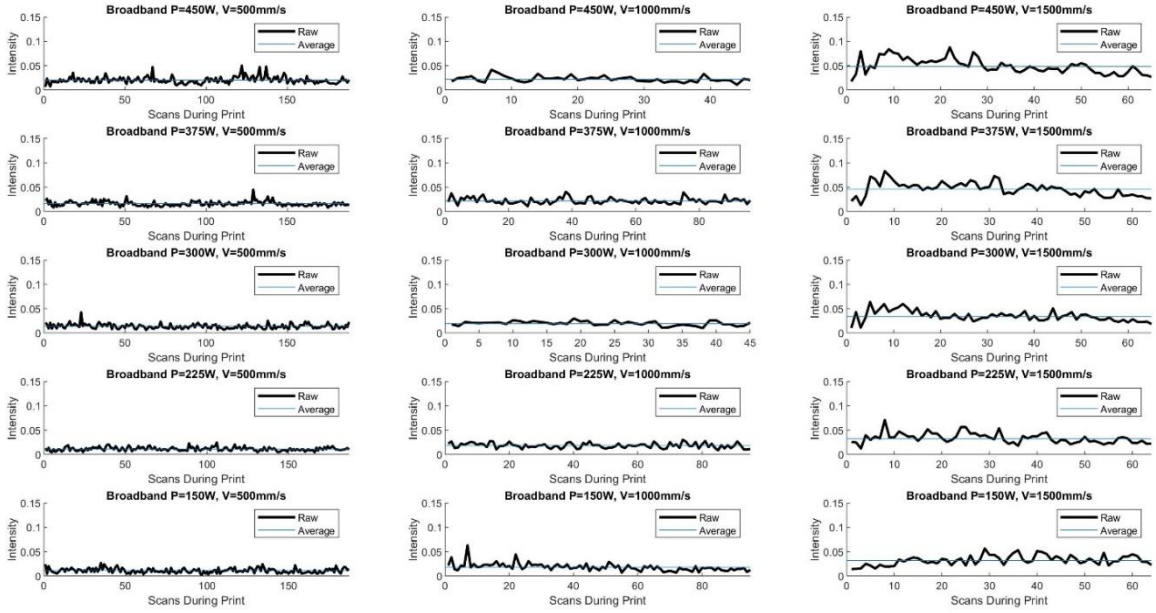

Figure 2.9 Variable Processing Parameter Updated Broadband Build Data

The general trend of increasing intensity as the power and velocity increase is much more visually present in Figure 2.9 as it is in Figure 2.8, when the intensity spikes are removed. It can able now be observed that the velocity processing parameter appears to have a greater impact on the fluctuation of intensity in the broadband spectrum. This is because a larger increase in the intensity can be seen as the velocity increased from left to right rather that power increasing from bottom to top in Figure 2.9.

The same individual line isolation was performed on the data recorded by the spectral diode filtered to the 520 nm wavelength. Figure 2.10 shows the original spectral intensity data from each of the fifteen individual weld beads of the 520 nm based on the varying processing parameters.

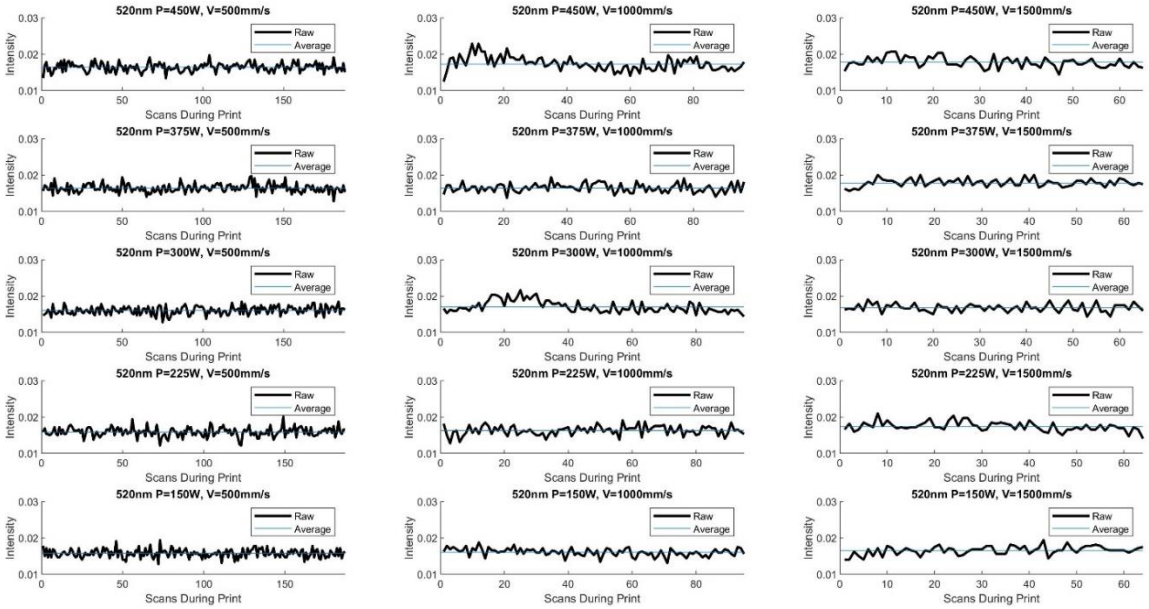

Figure 2.10 Variable Processing Parameter Original 520 nm Build Data

The same trend that is observed in the broadband data of Figure 2.8 and Figure 2.9 can also be seen in the 520 nm data of Figure 2.10. The spectral intensity increases as the

power and the velocity increase excluding the intensity spikes present in the P=450 W, V=1000 mm/s and P=300 W, V=1000 mm/s intensity data sets. The general trend is not quite as obvious in Figure 2.10 as it is in Figure 2.8 however. The amount of intensity difference between processing parameter changes in the 520 nm data is notably less than what is seen in the broadband data from Figure 2.8. Figure 2.11 shows the updated version of the 520 nm spectral intensity sets pertaining to the varying processing parameters while only considering the second half of the P=450 W, V=1000 mm/s and P=300 W, V=1000 mm/s intensity data sets matching what was done in the broadband.

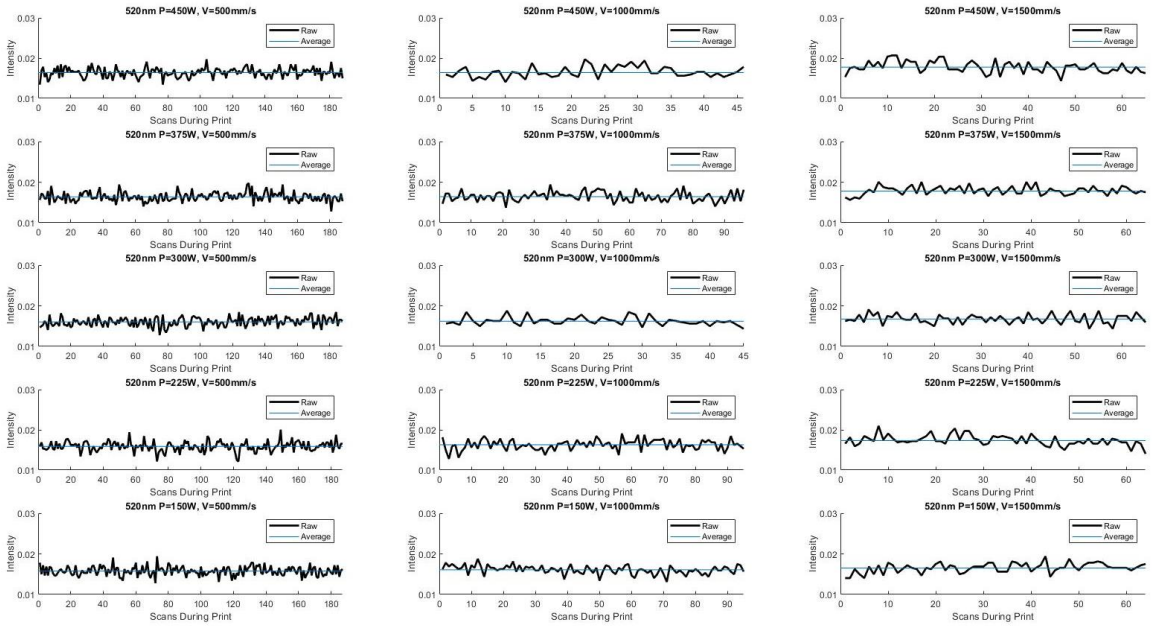

Figure 2.11 Variable Processing Parameter Updated 520 nm Build Data

Similar to what was observed in Figure 2.9, Figure 2.11 shows a much more defined trend that the intensity increases as the power and velocity increase across the cases. It also displays that velocity processing parameter again appears to have a slightly larger impact on the intensity values as it increases than the power processing parameter. These

are the same trends in the 520 nm intensity data that were observed in the broadband intensity data sets, before and after the intensity spikes were removed.

The same individual analysis of the 530 nm intensity data sets was performed with and without the intensity spikes being removed. Figure 2.12 shows the spectral intensity data from each of the fifteen individual weld beads of the filtered 530 nm wavelength based on the varying power and velocity values before the intensity spikes are removed.

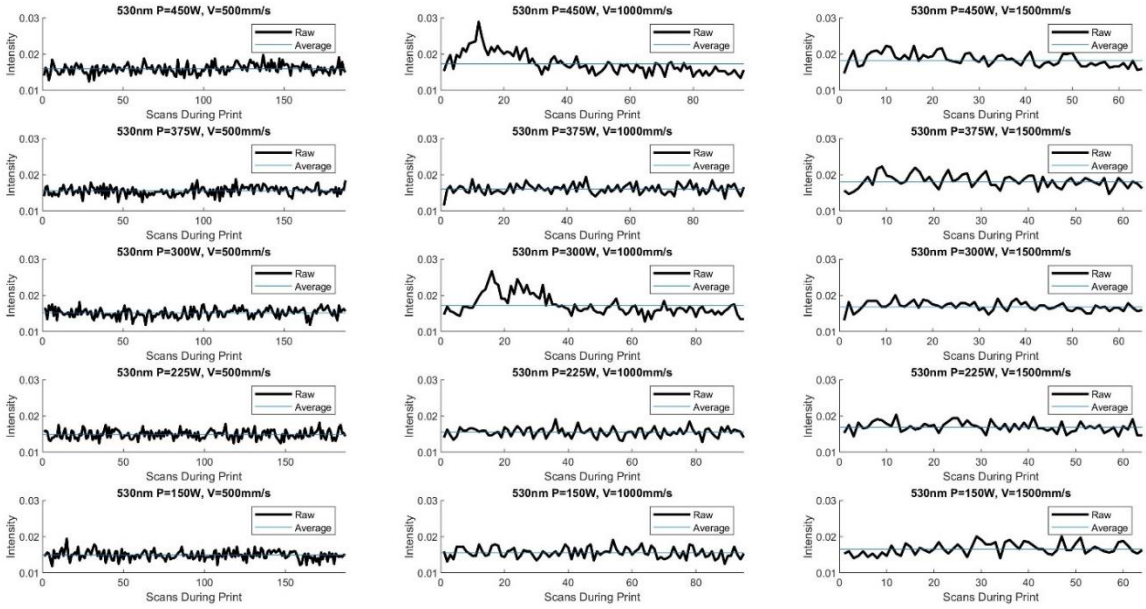

Figure 2.12 Variable Processing Parameter Original 530 nm Build Data

It can again be seen that the intensity tends to be greater as the power and the velocity processing parameters increase across all of the cases in the 530 nm intensity data. Also observed is the same two intensity spikes present in the P=450 W, V=1000 mm/s and P=300 W, V=1000 mm/s data sets. Figure 2.13 displays the intensity data of the filtered

530 nm wavelength of the builds with the intensity spikes in the P=450 W, V=1000 mm/s and P=300 W, V=1000 mm/s sets removed.

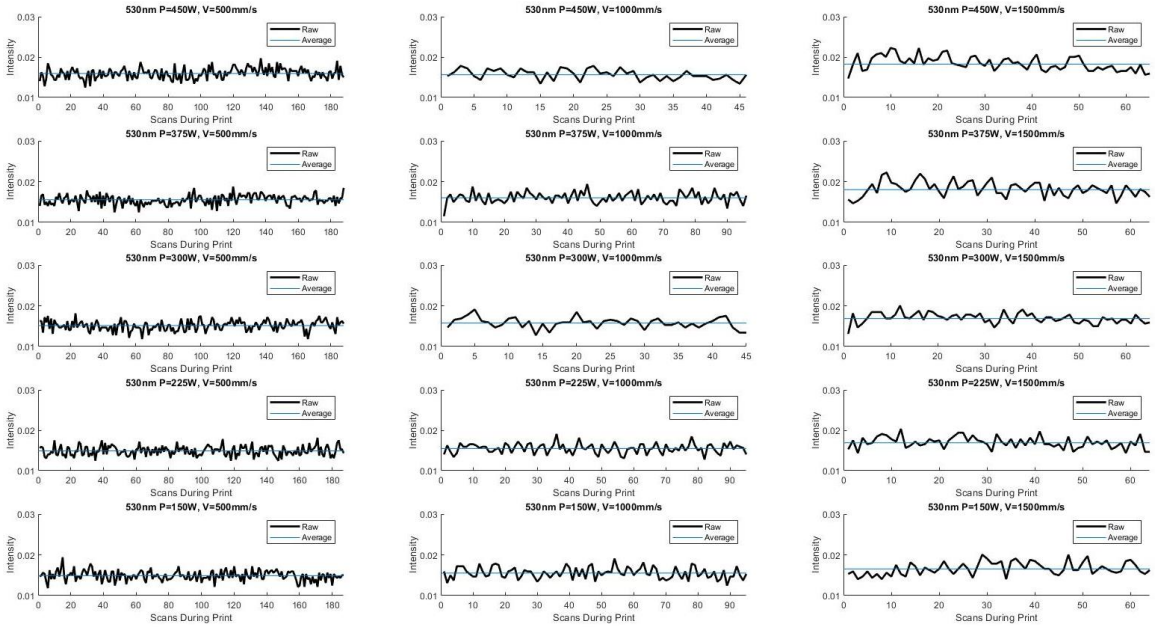

Figure 2.13 Variable Processing Parameter Updated 530 nm Build Data

Unsurprisingly, when the intensity spikes in the P=450 W, V=1000 mm/s and P=300 W, V=1000 mm/s intensity data sets were removed, the same trend in the 530 nm data can be observed as is present in the 520 nm and broadband data sets. Again, it appears in Figure 2.13 that the intensity increases as both the power and velocity processing parameters increase with the velocity seeming to have a slightly larger impact on the change in intensity.

With all of the individual intensity data sets isolated for each of the fifteen weld beads and all three filtered diodes, each individual line's properties can be calculated. The intensity spikes that are present in the P=450 W, V=1000 mm/s and P=300 W, V=1000 mm/s intensity data sets will be used as is, however the updated versions, where

the intensity spike locations are removed, will also be considered and the results of both will be compared in later sections.

2.4.3 Intensity Values

The main values that are collected from each of the individual printed lines are the mean and standard deviation values. For this experiment, the mean and standard deviation values were found by submitting the intensity data from each weld bead to a normal distribution. Figure 2.14 displays a generated normal distribution plot of the broadband intensity data pertaining to the P=450 W, V=500 mm/s printed line.

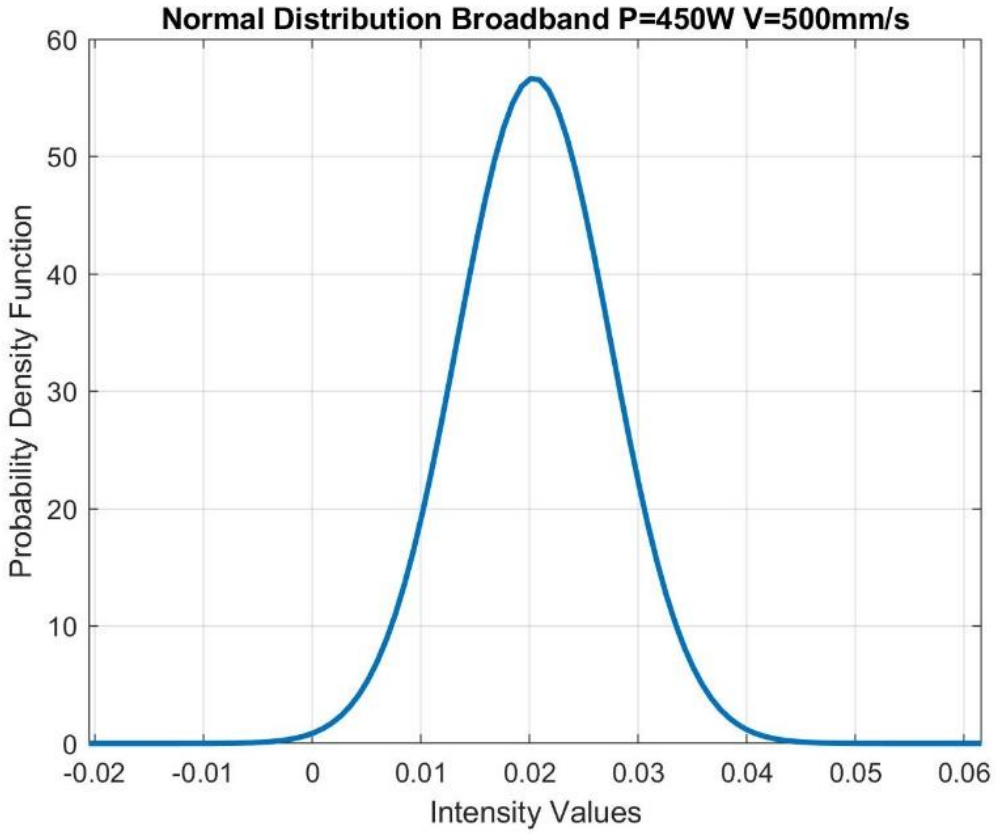

Figure 2.14 Normal Distribution of Broadband Intensity for P=450 W, V=500 mm/s

Figure 2.14 places the average intensity value for the P=450 W, V=500 mm/s printed line slightly larger than 0.02 which visually matches the data values for this line that are shown in Figure 2.8 and Figure 2.9. Each of the other individual intensity data sets were subjected to the same analysis both before and after the intensity spikes in the P=450 W, V=1000 mm/s and P=300 W, V=1000 mm/s sets were removed. These mean and standard deviation values would be recorded for future analysis.

Figure 2.15 shows the average broadband intensity of each of the fifteen individual weld beads during their printing. The left shows the original average intensity values including the intensity spikes in the P=450 W, V=1000 mm/s and P=300 W, V=1000 mm/s sets, and the right shows the mean intensity values after the spikes were removed. The horizontal axis of Figure 2.15, which shows the printed lines in order from one to fifteen can be referenced to the processing parameters shown in Table 2.2.

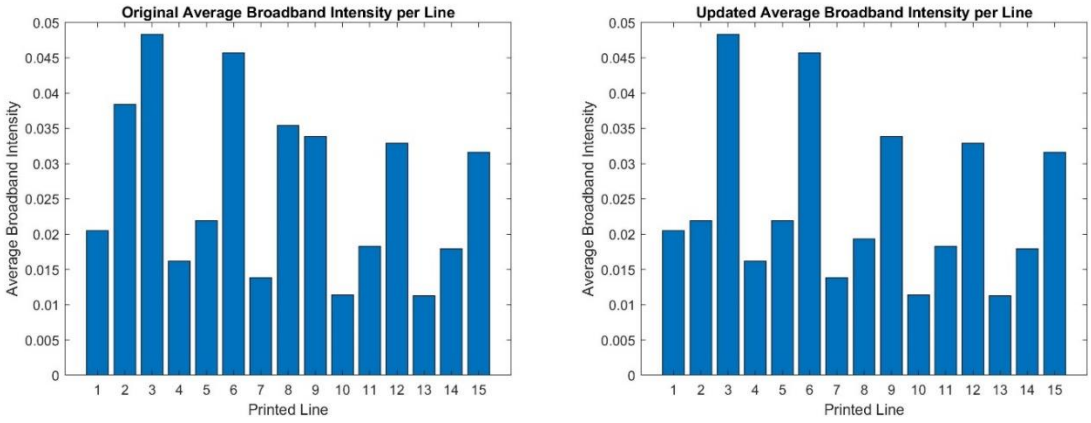

Figure 2.15 Variable Processing Parameter Average Broadband Intensity

As expected, it can be seen in Figure 2.15 that average broadband intensity increases as the power, velocity, or both processing parameters increase. This aligns with

the same general trend shown in the broadband data of the individual lines in Figure 2.8 and Figure 2.9. In the original average values in Figure 2.15, Printed Line 3, which corresponds to the largest values of the processing parameters used in this experiment (P=450 W and V=1500 mm/s), has the largest average spectral intensity of any of the lines. Conversely, Printed Line 13 has the lowest average spectral intensity since it was printed using the lowest processing parameters in this experiment (P=150 W and V=500 mm/s).

The right side of Figure 2.15, which shows the average broadband intensity values of each of the lines, displays a much more consistent behavior. As the power remains constant for three consecutive lines, the velocity increases from 500 mm/s to 1500 mm/s and the average intensity increases along with it. As the power is stepped down by 75 W, each group of three constant power print lines decrease for all three velocity values compared to the previous three with a higher power value. This affirms the trend that was shown before that the intensity will increase as the power and velocity processing parameters increase. Figure 2.15 also shows that the velocity processing parameter has more of an impact on the spectral intensity than the power. This can be seen by considering lines of the same velocity. For instance, in the updated average broadband intensity data, the lines pertaining to V=500 mm/s (lines 1, 4, 7, 10, and 13) with a drop of 75 W in power across, show a total change in value of about 0.01. When printed lines with the same power processing parameter are considered, for instance the lines with P=450 W (lines 1, 2, and 3) with an increase in velocity from 500 mm/s to 1500 mm/s

across, show a much greater change of about 0.0255. This affirms that the velocity processing parameter has a greater impact on the average intensity values than the power.

Figure 2.16 displays the average 520 nm intensity of each of the fifteen individual weld beads during their printing. The left was generated using the original 520 nm intensity data that includes the intensity spikes in the P=450 W, V=1000 mm/s and P=300 W, V=1000 mm/s data sets. The right considers the 520 nm intensity data with the two spikes removed.

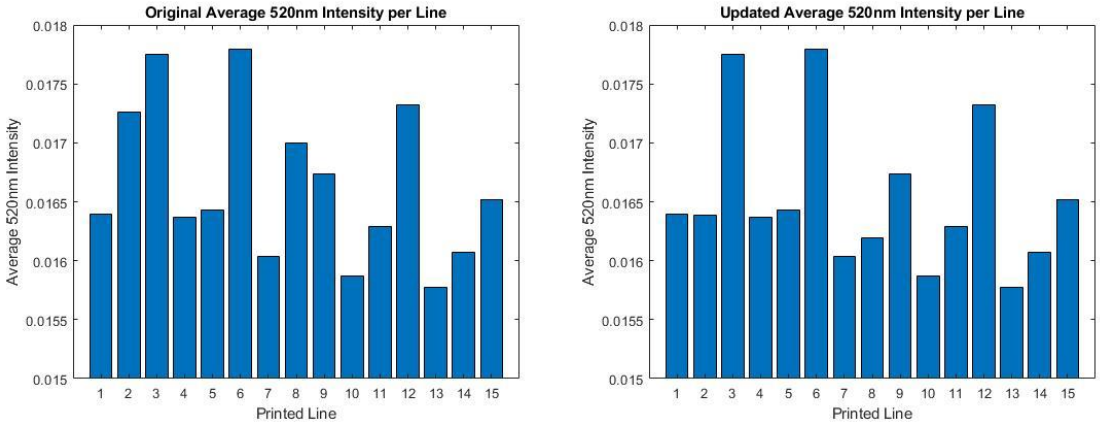

Figure 2.16 Variable Processing Parameter Average 520 nm Intensity

Similar to the average broadband data shown in Figure 2.15, the average 520 nm intensity data displayed in Figure 2.16shows that the average spectral intensity increases as the power and velocity processing parameters increase. It also shows the same periodic trend in the updated average 520 nm intensity data but with less visible difference in values as processing parameters change. However, it still shows that the velocity has a much greater impact on the intensity values than the power processing parameter since

there is a greater change in intensity over the range of velocity values than there is in the range of power values.

Figure 2.17 shows the average 530 nm intensity of each of the fifteen individual weld beads during printing. Similar to the previous figures, the left was generated using the original 530 nm average intensity values that include the intensity spikes in the P=450 W, V=1000 mm/s and P=300 W, V=1000 mm/s data sets and the right considers the 530 nm intensity data with the two spikes removed.

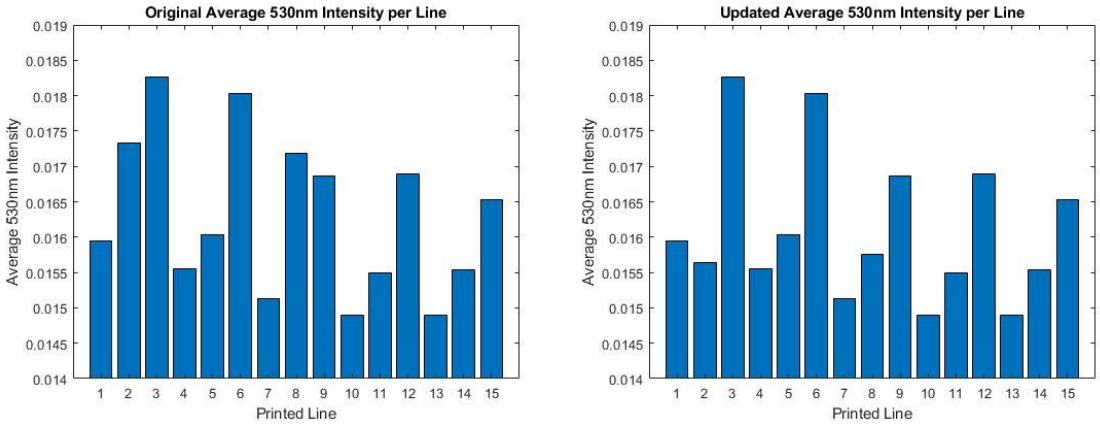

Figure 2.17 Variable Processing Parameter Average 530 nm Intensity

Similar to the average broadband intensity and average 520 nm intensity data, the average 530 nm intensity data shown in Figure 2.17 follows the general trend of increasing intensity values corresponding to larger power and velocity processing parameter values. It also shows the periodic same trend in the updated average 530 nm intensity values and the visualization that the velocity processing parameter has a greater effect on the intensity values than the power does. The individual quantitative impact of each of the varying processing parameters is shown in the following section.

2.4.4 Generating Equation of Processing Parameters

Once the average intensity values were found for each of the individual weld beads in each of the spectral data sets, plots relating the power and the velocity to the average values were generated. These were generated to give a better understanding of each of the processing parameters would influence the average intensity values individually. They would be generated twice, once with the original intensity data including the intensity spikes present in the P=450 W, V=1000 mm/s and P=300 W, V=1000 mm/s data sets, and again with the spikes removed.

Figure 2.18 shows the original and the updated average spectral broadband intensity as it relates to the power processing parameter on the left and right respectively. The data points corresponding to the varying velocity parameters are shown in alternate colors for clarity. The bars on the data point correspond to the normal standard deviation that was determined earlier for each specific printed line.

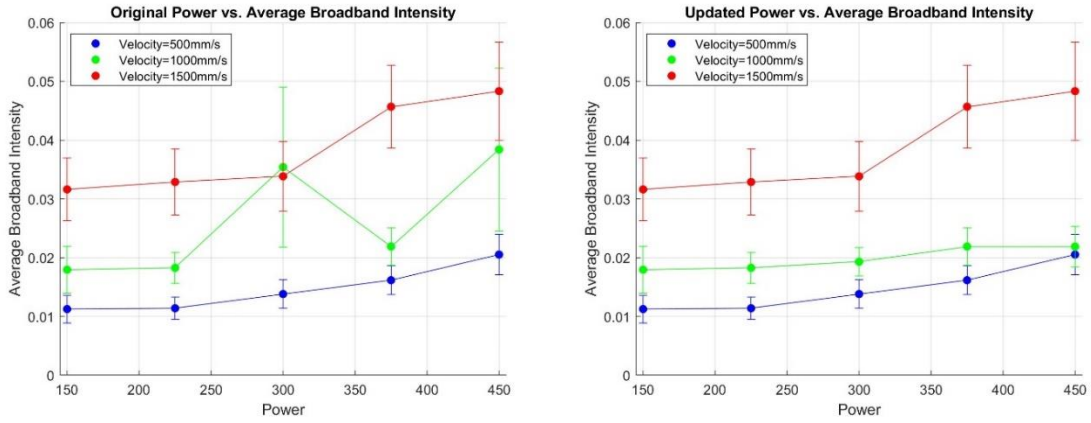

Figure 2.18 Variable Processing Parameter Power vs. Average Broadband Intensity

In the original broadband intensity of the left of Figure 2.18, it can be seen that most of the points follow the general trend described earlier. As the power and velocity increase, the average spectral intensity increases however, the intensity spikes that are included have a significant impact on this trend. The data points that correspond to the P=450 W, V=1000 mm/s and P=300 W, V=1000 mm/s broadband intensity data are uncharacteristically greater than the rest of the values that follow the general trend and show a much larger standard deviation compared to the rest of the broadband intensity data sets. Considering the broadband data once the intensity spikes are removed however, the average broadband intensity values that correspond to the P=450 W, V=1000 mm/s and P=300 W, V=1000 mm/s prints fall into the previously described trend of steadily increasing values as the power and velocity processing parameters increase and have much more contained standard deviations.

Figure 2.19 shows the average 520 nm intensity as a function of the power processing parameter. The left figure displays the analysis performed using the original intensity that includes the spikes in the P=450 W, V=1000 mm/s and P=300 W, V=1000 mm/s intensity. The left shows the analysis performed once the spikes in the P=450 W, V=1000 mm/s and P=300 W, V=1000 mm/s data were removed. Again, the data points corresponding to the varying velocity parameters are shown in alternate colors for clarity and the bars on the points correspond to the standard deviation of each of the intensity data sets.

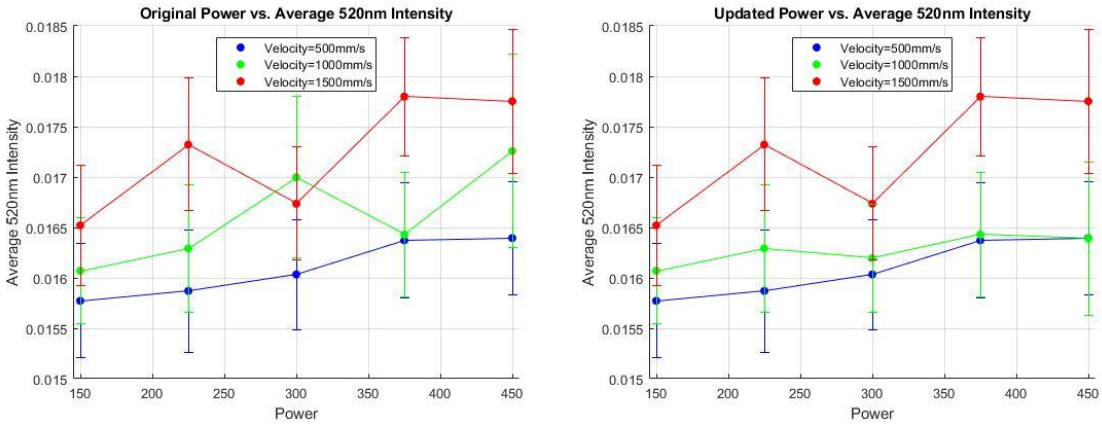

Figure 2.19 Variable Processing Parameter Power vs. Average 520 nm Intensity

Similar to Figure 2.18, Figure 2.19 shows a general trend of increasing average 520 nm spectral intensity as the power and velocity processing parameters increase. Also, like the average broadband intensity data, the original average 520 nm intensity data shows the two spikes corresponding to the P=450 W, V=1000 mm/s and P=300 W, V=1000 mm/s points with large standard deviations. It also shows that once the spikes were removed, the points fall back into the general trend of increasing average intensity as the power and velocity processing parameters increase.

One difference between the average 520 nm intensity points and the average broadband intensity points is the 520 nm shows a significant spike in average intensity for the average intensity point corresponding to the processing parameters P=225 W and 1500 mm/s. This point spikes outside of the general trend similar to how the P=450 W, V=1000 mm/s and P=300 W, V=1000 mm/s points do, however, this spike only shows up in the average 520 nm data not the average broadband or average 530 nm results.

Because of this, the spike is kept as is for the 520 nm calculations and will be noted as a probable source of error.

Figure 2.20, which displays the original and updated average 530 nm intensity as it relates to the power processing parameter, shows the same spikes for the points corresponding to the P=450 W, V=1000 mm/s and P=300 W, V=1000 mm/s points in the original data.

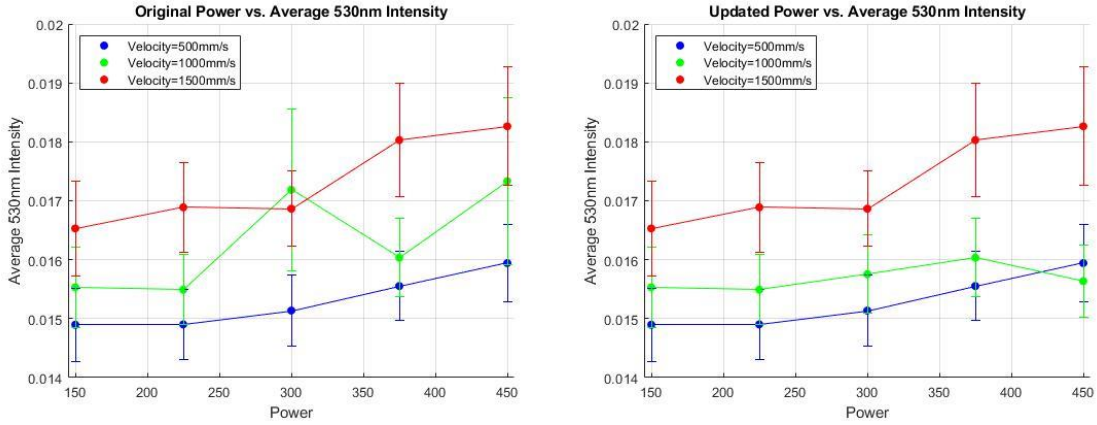

Figure 2.20 Variable Processing Parameter Power vs. Average 530 nm Intensity

Unlike the average 520 nm intensity in Figure 2.19, there no spike present for the point corresponding to the P=225 W and 1500 mm/s line. Similar to both the average broadband and 520 nm intensities, the general trend of increasing average intensity is present when the processing parameter values increase. Also similar is that when the spikes corresponding to the P=450 W, V=1000 mm/s and P=300 W, V=1000 mm/s data sets are removed, the average values and standard deviations related to these fall into the general trend previously described.

Figure 2.18, Figure 2.19, and Figure 2.20 all show a general trend of increasing average spectral intensity values as the power processing parameter increases. In all of the figures this trend does not appear to be a linear relationship, it appears that the power processing parameter and the average spectral intensity values have more of a quadratic relationship. This assumption is made because the average intensity values shown in Figure 2.18, Figure 2.19, and Figure 2.20 appear to increase by large amount as the power processing parameter increases. They also show that the average intensity values are affected more by the velocity processing parameter since the overall amount of average intensity change across the varying power is noticeably less than the overall change over the range of the velocity.

Similar to the plots relating the power to the average intensity values, plots relating the velocity to the average intensity values were generated. These were generated to give a better understanding of how the velocity processing parameter influences the average intensity values individually. Figure 2.21 shows the average spectral broadband intensity as a function of the velocity processing parameter. The left displays the interaction before the spikes corresponding to the P=450 W, V=1000 mm/s and P=300 W, V=1000 mm/s parameters were removed and the right shows the results after. The data points corresponding to the varying power values are shown in alternate colors for clarity. The bars attached to each point again represent the standard deviation found in the intensity data for each of the printed lines.

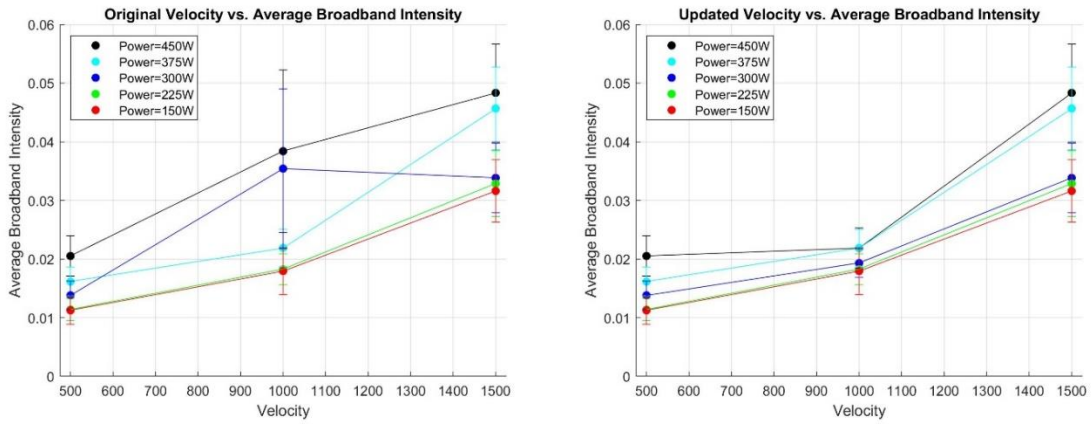

Figure 2.21 Variable Processing Parameter Velocity vs. Average Broadband Intensity

As expected, the results shown in Figure 2.21 follow the general trend where average broadband intensity increases as the velocity processing parameter increases excluding the two spikes in the data for the P=450 W, V=1000 mm/s and P=300 W, V=1000 mm/s average intensity points. However, once the intensity spikes were removed, it can be seen that the velocity has less of an impact on the increase in average intensity from 500 mm/s to 1000 mm/s as it does for 1000 mm/s to 1500 mm/s. This observed behavior leads to the assumption that the relationship between the velocity and the spectral intensity is quadratic, meaning that as the velocity processing parameter increases, the average intensities will increase by more and more.

This same analysis that was performed on the relationship between the velocity processing parameter and the average broadband intensity values would be performed using the average 520 nm and 530 nm intensity values.Figure 2.22 displayes the average 520 nm spectral intensity values as they realte to the velocity processing parameter. The left displays the origional 520 nm intensity data values and the right displays the data

after the spikes present in the P=450 W, V=1000 mm/s and P=300 W, V=1000 mm/s data were removed.

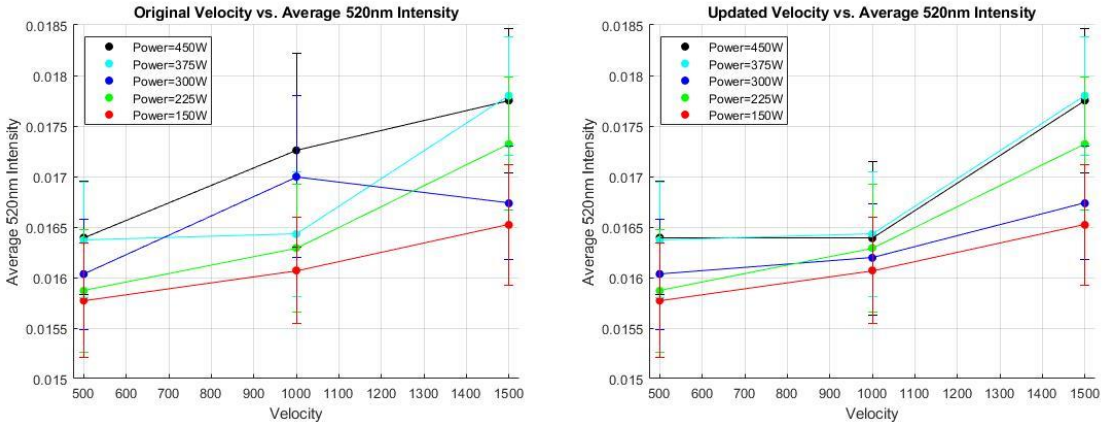

Figure 2.22 Variable Processing Parameter Velocity vs. Average 520 nm Intensity

Visually from the original data, it can be determined that the same trend of increasing intensity with increasing velocity can be observed for the average 520 nm intensity values. The same two outlying points corresponging to the P=450 W, V=1000 mm/s and P=300 W, V=1000 mm/s intensity data are present. Once the data was updated, the relationship between the velocity and the average 520 nm intensity can be assumed to be quadratic similar to the average broadband intensity and velocity relationship in Figure 2.21.

Much like the average broadband and 520 nm intensity relationships with the velocity, the average 530 nm intensity as it relates to the velocity processing parameter, displayed in Figure 2.23, shows the same increasing quadratic relationship between the average intensity values and the velocity.

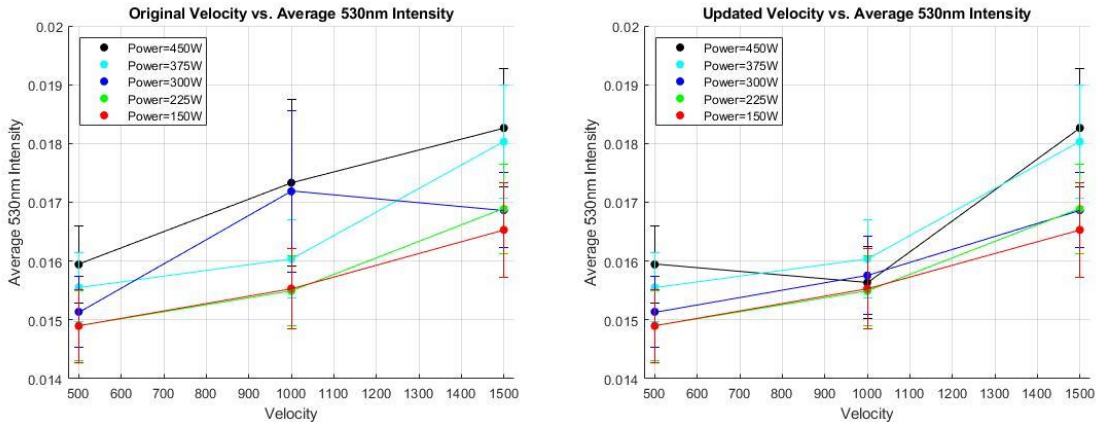

Figure 2.23 Variable Processing Parameter Velocity vs. Average 530 nm Intensity

This again, excludes the two spikes in the P=450 W, V=1000 mm/s and P=300 W, V=1000 mm/s intensity data that were removed for the updated velocity and average 530 nm intensity relationship shown on the right of Figure 2.23.

Once the relationships between average spectral intensity values and the individual processing parameters were found, a best fit equation is generated. This generated equation will encompass both the power and velocity individually as they relate to the average spectral intensity values found for each of the spectrums utilized in this experiment. It will return an expected value for the spectral intensity based on a function of two input variables. Mathematically, it will take the form of the following:

$$I = f(P, V)$$

Equation 2.1 General form of Intensity, Power, and Velocity Relationship

Where I is the spectral intensity, P is the power processing parameter and V is the velocity processing parameter.

In order to generate a formula for the spectral intensity as a function of power and velocity, the trends from the power vs intensity and the velocity vs. intensity would need to be combined to determine their effect together on the intensity rather than individually. This was performed using *MATLAB's* built in function "x2fx." This built in function takes a vector of input values and a vector of result values and fits them to a 2 variable input equation using a regression method [40]. In this case the resultant values are the average intensity and the 2 input variables are the power and velocity processing parameters. This built in function was utilized for analysis of all of the data sets, broadband, 520 nm, and 530 nm. The determined function of input variables power and velocity is shown in the Results section below. This equation is in a polynomial form since the interaction between the processing parameters and the average intensity values is observed to be quadratic. The polynomial equation is used to generate surface plots relative to the calculated average intensity values shown in the Results section.

2.5 Results

Results for the effects of processing parameters on spectroscopy data of LPBF print include the generated formula for estimating the spectral intensity value based on processing parameters, referred to as Harvey's Theorem. It will also include the figures generated of the surface fitting of to the average intensity values using Harvey's Theorem. The results of these sections will be compared to the calculated Rosenthal cooling rate solutions at the surface of the melt pool depth $d = 0$ to determine if the average intensities found in this experiment align with the theoretical thermal properties.

2.5.1 Harvey's Theorem

Harvey's Theorem is a polynomial equation that estimates the spectral intensity reading of a diode in a laser powder bed fusion build. The theorem was generated using a regression analysis via a built in *MATLAB* function that takes the inputs from multiple variables and results and fits them to an equation of two variables. Equation 2.2 displays the polynomial form of Harvey's Theorem. Table 2.3 displays the corresponding constant values that are used in Harvey's Theorem for each of the spectrums observed in this experiment before the intensity spikes in the P=450 W, V=1000 mm/s and P=300 W, V=1000 mm/s data were removed.

$$I = C_1 + C_2P + C_3V + C_4PV + C_5P^2 + C_6V^2$$

Equation 2.2 Harvey's Theorem

Table 2.3 Original Constants of Harvey's Theorem

Constant Values	Broadband	520 nm	530 nm
C_1	0.005063487043570	0.015151897006090	0.014016518106429
C_2	-0.000040157196660	0.000001817270813	-0.000001746899867
C_3	0.000013362230845	0.000000281992541	0.000001395640105
C_4	0.000000030586629	0.000000001589939	0.000000002487003
C_5	0.000000100477363	-0.000000000345941	0.000000007278783
C_6	0.000000000653073	0.000000000189149	-0.00000000005618

Table 2.4 displays the constant values that are used in Harvey's Theorem for each of the spectrums observed in this experiment after the intensity spikes in the P=450 W, V=1000 mm/s and P=300 W, V=1000 mm/s data were removed.

Table 2.4 Updated Constants of Harvey's Theorem

Constant Values	Broadband	520 nm	530 nm
C_1	0.028782256552995	0.016343600291313	0.016168880964123
C_2	-0.000052789909466	0.000001379390090	-0.000001905818887
C_3	-0.000038858022540	-0.000002394831290	-0.000003609582990
C_4	0.000000030586629	0.000000001589939	0.000000002487003
C_5	0.000000097056517	-0.000000000904263	0.000000005029613
C_6	0.000000026763200	0.000000001527561	0.000000002446432

Comparing the constant values in Table 2.4 and Table 2.3, the constants in the original data do not differ much from the updated constant values. However, the values that are shown in Table 2.4 are assumed to be more accurate since the spikes in the P=450 W, V=1000 mm/s and P=300 W, V=1000 mm/s data sets are not considered. The estimated intensity values that are calculated using Harvey's Theorem based on the original and updated intensity values will be compared in later sections for their reliability.

2.5.2 Estimating Intensity Values

The following figures were generated using the above equation and constants located in Table 2.3 and Table 2.4 to create an estimated intensity surface relative to the average spectral intensity points. In the figures, the red dots represent the average spectral intensity values in 3D space based on the power and velocity processing parameters. The blue surface is the estimated intensity values generated by Harvey's Theorem for the original and updated data sets.

Figure 2.24 displays the relationship between the average broadband intensity, power, and the velocity in 3D space as well as the surface that represents the estimated

values of the intensity based on Harvey's Theorem and processing parameters. The left displays the results based on the original data that includes the spikes in the P=450 W, V=1000 mm/s and P=300 W, V=1000 mm/s data, and the right shows the results based on the updated data.

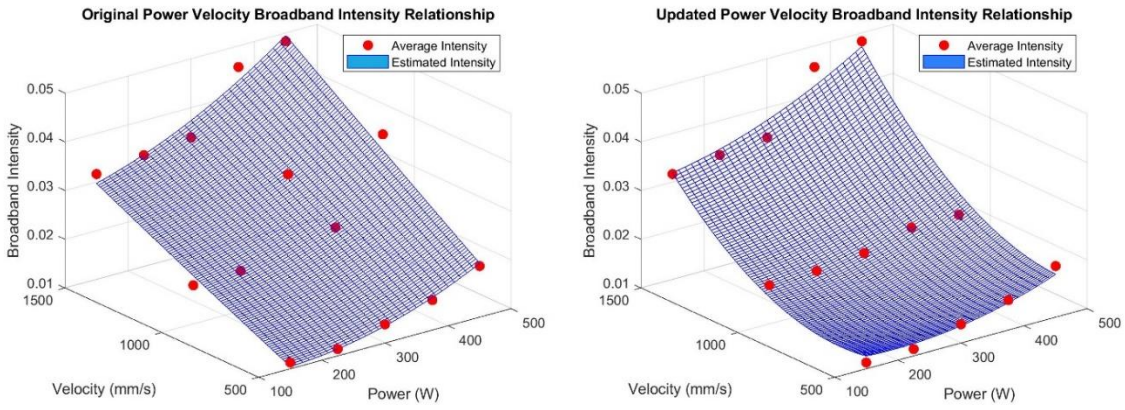

Figure 2.24 Variable Processing Parameter Power Velocity Broadband Intensity Relationship

Visually it can be seen that the generated surface shown in original data in Figure 2.24 aligns fairly well with all but two of the average broadband intensity values that are represented by the red dots. The points representing the average broadband intensity values corresponding to the processing parameters P=450 W, V=1000 mm/s and P=300 W, V=1000 mm/s appear to be separated more from the estimated surface in the original data. Whereas the surface that was generated using the updated intensity data on the right side of Figure 2.24 appears to align much more closely with the average broadband intensity values. This observation will be quantitatively analyzed in the Error of Estimation section below.

Figure 2.25 shows the average 520 nm intensity, power, and velocity relationship in 3D space as well as a surface that represents the estimated values of the intensity based on Harvey's theorem and the processing parameters. Again, the red dots represent the average spectral intensity values in 3D space based on the power and velocity processing parameters and the blue surface is the estimated intensity values generated by Harvey's Theorem. The left side of Figure 2.25 shows the relationship regarding the original data that includes the spikes in the P=450 W, V=1000 mm/s and P=300 W, V=1000 mm/s data and the right side displays the relationship after they are removed.

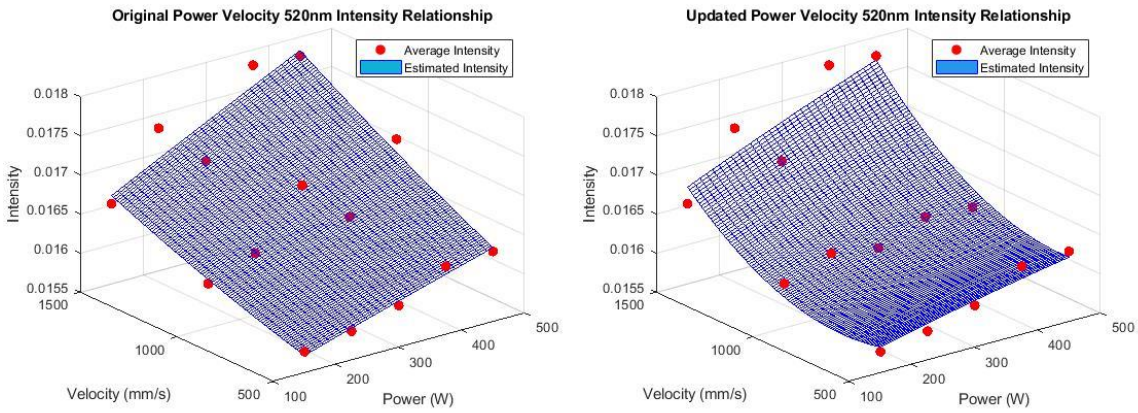

Figure 2.25 Variable Processing Parameter 520 nm Power Velocity Intensity Relationship

Similar to the broadband surfaces, the 520 nm surface generated by the original 520 nm data aligns relatively close to the average intensity points with the same significant outlier points corresponding to the processing parameters P=450 W, V=1000 mm/s and P=300 W, V=1000 mm/s. Once they were removed there was an improvement in the alignment between the estimated surface and the average intensity points. The

comparison between the power, velocity, and average 520 nm intensity points will also be quantitatively analyzed in the Error of Estimation section below.

Figure 2.26 displays the relationship between the original and updated average 530 nm intensity, power, and velocity in 3D space as well as the surface that represents the estimated values of the intensity based on Harvey's theorem as a function of the processing parameters. The left of Figure 2.26 displays the relationship based on the original data and the right side shows the relationship after the spikes present in the P=450 W, V=1000 mm/s and P=300 W, V=1000 mm/s are removed. Again, the red dots represent the average 530 nm spectral intensity values and the blue surface represents the estimated 530 nm intensity values as function of the processing parameters.

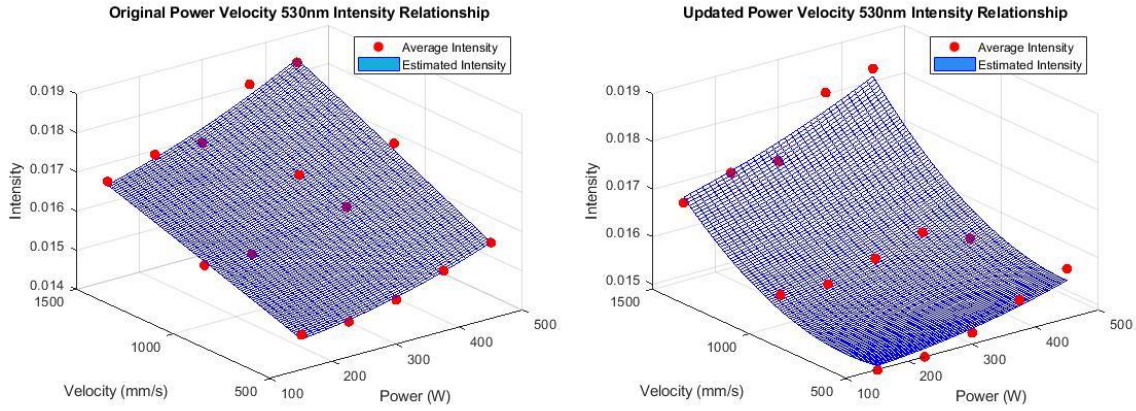

Figure 2.26 Variable Processing Parameter 530 nm Power Velocity Intensity Relationship

Similar to the broadband and 520 nm estimated intensity surfaces, the 530 nm estimated intensity surface generally follows the shape set by the average 530 nm intensity points

especially once the spikes pertaining to the P=450 W, V=1000 mm/s and P=300 W, V=1000 mm/s data sets are removed.

Visually from Figure 2.24, Figure 2.25, and Figure 2.26, it can be seen that the estimated surfaces generated using Harvey's Theorem follow the general shape of each of the fifteen individual average intensity points. However, the theorem is not perfect and has an amount of error that will be calculated in the next section. It can also be confirmed that the velocity processing parameter has more of an effect on the intensity values. This determination is based on the observation that the overall intensity increases by a significantly larger amount across its range compared to the overall change in intensity over the range of power values.

2.5.3 Error of Estimation

Once the surfaces were generated based on the estimated intensity formula referred to as Harvey's Theorem for each of the spectrums observed in this experiment, the percent error would be calculated between the estimation and the recorded average intensity values. The method used for calculating the percent error between the average intensity points and the estimated intensity values is shown in Equation 2.3.

$$\%_{error} = \left|\frac{value_{experimental} - value_{estimated}}{value_{estimated}}\right| \times 100$$

Equation 2.3 Percent Error Calculation [41]

In Equation 2.3, the $value_{experimental}$ refers to the average intensity values that were determined by analyzing the spectroscopy data both before and after the spikes in the P=450 W, V=1000 mm/s and P=300 W, V=1000 mm/s data sets are removed. The

$value_{estimated}$ refers to the estimated intensity values determined by Harvey's Theorem and the processing parameters at each individual average intensity point.

Figure 2.27 displays the calculated percent error between each of the average broadband intensity values and the estimated broadband intensity values for both the original data and the updated data once the spikes in the P=450 W, V=1000 mm/s and P=300 W, V=1000 mm/s data sets are removed.

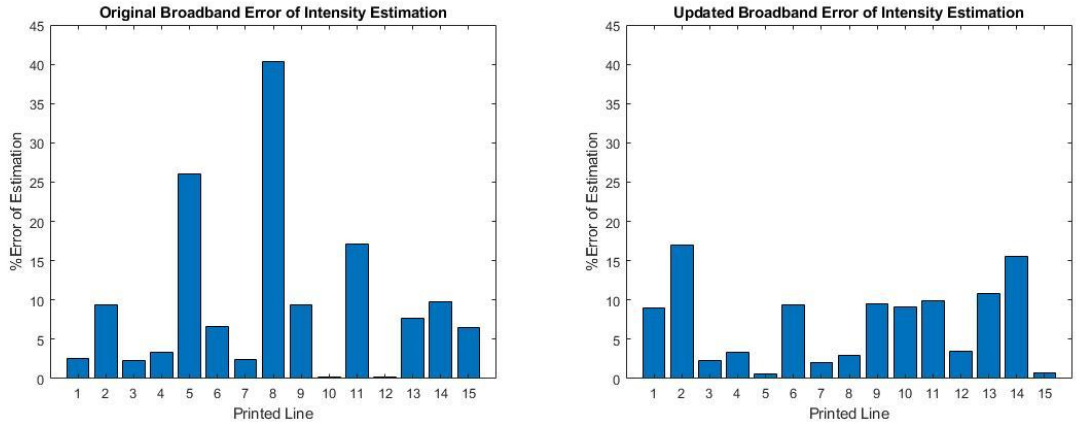

Figure 2.27 Error of Broadband Intensity Estimation

Unsurprisingly, the highest source of error in the original broadband data comes from the lines corresponding to the P=300 W, V=1000 mm/s data sets that include one of the intensity spikes. Once the spikes in the data are removed, it can be seen that the maximum amount of percent error decreases from approximately 40% to less than 20%. The removal of the spikes in the intensity data proved to be an acceptable approach in developing an equation that estimates the intensity as a function of the processing parameters since the calculated percent error was reduced by over half the original.

Figure 2.28 displays the original and updated calculations of the percent error between the estimated 520 nm intensity and the measured average 520 nm intensity values based on the varying processing parameters.

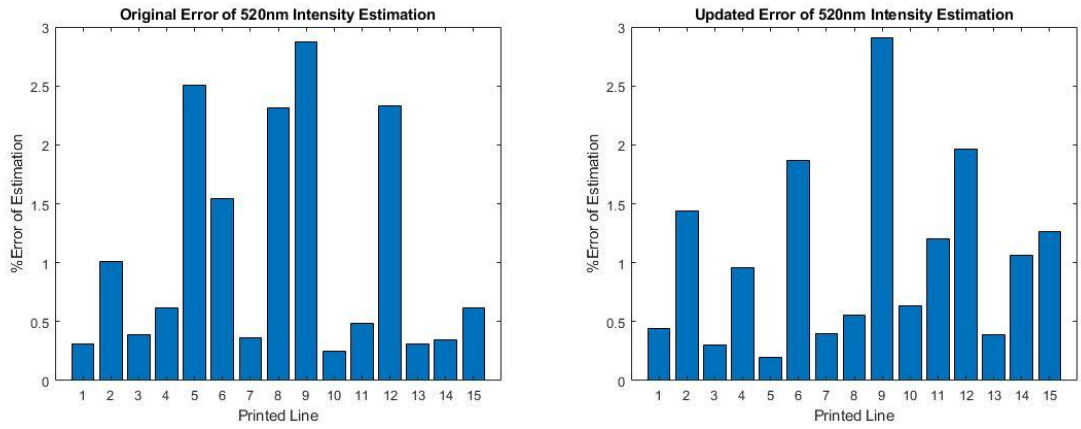

Figure 2.28 Error of 520 nm Intensity Estimation

Unlike the percent error calculation for the broadband intensity, the calculated percent errors in the 520 nm intensity values do not significantly decrease once the spikes in the P=450 W, V=1000 mm/s and P=300 W, V=1000 mm/s data sets are removed. However, all of the calculated percent errors for all of the lines in the 520 nm data are less than 3% for both the original and updated data sets. Relating this back to Figure 2.10, which displays the original 520 nm intensity data sets for each of the processing parameter combinations, the two spikes present in the P=450 W, V=1000 mm/s and P=300 W, V=1000 mm/s intensity data sets do not deviate as much as the spikes present in these data sets for the broadband and 530 nm intensity. So it is unsurprising that the reduction in calculated percent error between the average intensity values and the estimated

intensity was less for the 520 nm data compared to the broadband and 530 nm intensity calculations.

Figure 2.29 shows the calculated percent error between the measured average 530 nm intensity and the estimated 530 nm intensity values found using Harvey's Theorem. The left displays the calculated percent error using the original data that includes the spikes in the P=450 W, V=1000 mm/s and P=300 W, V=1000 mm/s data and the right shows the calculated percent error once the spikes were removed.

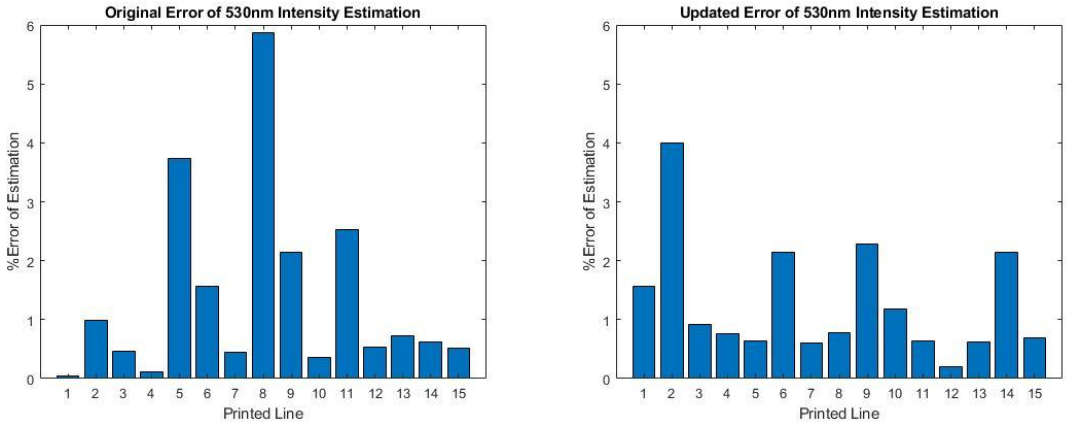

Figure 2.29 Error of 530 nm Intensity Estimation

Once the spikes in the P=450 W, V=1000 mm/s and P=300 W, V=1000 mm/s data sets are removed, the maximum amount of percent error between the average 530 nm intensity values and the estimated intensity drops from approximately 6% to 4%. This drop is significantly more than what was found in the 520 nm intensity examination but much less than the error drop-off observed in the broadband intensity analysis.

In all the three spectrums measured in this experiment, the percent error between the measured and calculated intensity values were reduced once the spikes in the P=450

W, V=1000 mm/s and P=300 W, V=1000 mm/s data sets were removed. Table 2.5 lists the average percent error pertaining to the original data in the broadband, 520 nm, and 530 nm as well as the updated data.

Table 2.5 Original and Adjusted Average Percent Error

Average %Error	Broadband	520 nm	530 nm
Original Average %Error	9.5902	1.0835	1.3776
Updated Average %Error	7.0362	1.0390	1.2798

It is clear to see that a significant reduction in average percent error shows up in the broadband data once the intensity spikes in the P=450 W, V=1000 mm/s and P=300 W, V=1000 mm/s data sets are removed. The 520 nm and 530 nm data sets also show a reduction in average percent error once the spikes in the data were removed however the amount of reduction is less than 1% average in both cases.

Another method to calculate the accuracy of estimated intensity values based on the processing parameters is finding the coefficient of determination between the measured average spectral intensity values and the estimated intensity. The coefficient of determination or R-Square (R^2) is a calculated value between 0 and 1 that measures how well a regression line fits data. It is a very common way to measure the strength of a model. Equation 2.4 displays the formula for calculating the coefficient of determination adjusted to take into account the number of independent variables in a model [42].

$$R^2 = 1 - \frac{(n-1)}{[n-(k+1)]}\left(1 - \left[1 - \frac{\sum_{i=1}^{n}(x_i - \hat{x_i})^2}{\sum_{i=1}^{n}(x_i - \bar{x})^2}\right]^2\right)$$

Equation 2.4 Coefficient of Determination (R^2) [42]

In Equation 2.4, n is the sample size, in this case fifteen for each spectrum observed, k is the number of independent variables, 2 in this experiment for the power and velocity, x_i is the measured average intensity points based on the data, $\widehat{x_i}$ is the estimated intensity value calculated from Harvey's Theorem at the given point, and $\bar{x}$ is the average value of all of the measured intensity data.

The adjusted version of the calculation for the coefficient of determination is used in this experiment because it allows the regression model to be quadratic or polynomial instead of being limited to linear. Earlier in this experiment, it was found that the power and the velocity processing parameters affect the intensity values in a non-linear relationship. Table 2.6 lists the calculated coefficients of determination between the measured average intensity values and the estimated values for each of the processing parameter combinations in this experiment. Both the original intensity data, as well as the intensity data once the spikes in the P=450 W, V=1000 mm/s and P=300 W, V=1000 mm/s data sets are removed are shown.

Table 2.6 Original and Updated Coefficient of Determination R^2 Values

R^2	Broadband	520 nm	530 nm
Original R^2 Value	0.8886	0.8408	0.8871
Updated R^2 Value	0.9626	0.8633	0.9260

Based on the results in Table 2.6, it can be seen that the strength of the model generated using original intensity data for all three observed spectrums is fairly high since the coefficients of determination are greater than 0.84. However, after the spikes in the P=450 W, V=1000 mm/s and P=300 W, V=1000 mm/s data sets are removed, the

strength of the model increases greatly for both the broadband and 530 nm estimation formulas. The strength of the 520 nm estimation model also increases, but it increases by less than both the broadband and 530 nm. These results are promising in the sense that Harvey's Theorem can predict the expected spectral intensity measured in a LPBF build with an accuracy of 96% when looking at the broadband light spectrum intensity, 86% when looking at the 520 nm wavelength intensity, and 93% when measuring the 530 nm wavelength.

2.5.4 Line to Continuum

Similar to the process of isolating individual processing parameter effects on the average spectral intensity, the individual processing parameter effects on the line to continuum ratio were generated into the plots shown in Figure 2.30. The line to continuum ratio is a published analytical method developed by researchers at Penn State University [35].

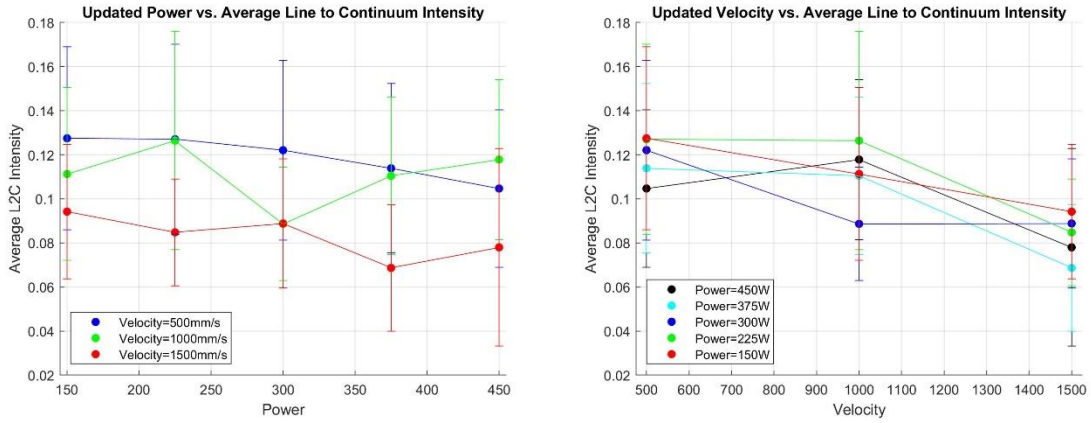

Figure 2.30 Variable Experiment Power and Velocity vs Line to Continuum

Based on the plots shown in Figure 2.30, the line to continuum ratio appears to have an inverse trend compared to the single wavelength analysis. As the power or the velocity processing parameters increase, the line to continuum tends to decrease or stay relatively the same.

2.5.5 Summary of Trends Based on Varying Processing Parameters

A summary of trends observed in this experiment based on the processing parameters as well as their effect on known physical properties of LPBF are shown in Figure 2.31. In Figure 2.31, the first four rows are the results round in this experiment and the last four are from experiments performed to determine the effect of processing parameters on melt pool geometry and cooling rates [7].

Reaction	As Power Increases	As Velocity Increases
Broadband Intensity	↑	↑
520nm Intensity	↑	↑
530nm Intensity	↑	↑
Line to Continuum	↓	↓
Melt Pool Length L	↑	-
Melt Pool Depth d	↑	↓
Melt Pool Area	↑	↓
Cooling Rate	↓	↑

"↑" = Increases	"↓" = Decreases	"-" = No Change

Figure 2.31 Summary of Effects on Trends by Varrying Power and Velocity

Visually it can be seen that none of the spectroscopy results nor the line to continuum results completely agree with the known effects the processing parameters have on the physical properties of LPBF. As both the power and velocity increase the spectral intensities increase and the line to continuum decrease. These behaviors are not matched by any of the physical properties in LPBF that are known to react to the changes in processing parameters. These physical properties refer to the melt pool dimensions such as the length and depth of the pool, the melt pool also known as the thermal gradient in LPBF and the cooling rate of the solidifying material.

2.6 Discussion

The general relationship between spectral intensity, power, and velocity processing parameters can be observed in all of the figures based on the data collected in Chapter 2. The spectral intensity of the broadband, 520 nm, and 530 nm spectrums will increase or decrease as either the power, velocity, or both processing parameters increase or decrease in a LPBF build respectively. Alternatively, it was found that the line to continuum ratio will decrease or remain about the same as the power or velocity processing parameters increase.

Intuitively, the observed effect of the velocity processing parameter makes sense when considering the calculated cooling rates. Since it's known that as the velocity processing parameter increases in a LPBF build, the melt pool depth will be reduced and the overall length will remain constant. Since there is less melted material as the velocity increases, the cooling rate for the lines will be quicker. When the cooling rate is faster, the average temperature across the solidifying line will decrease. The increasing spectral

intensity and increasing cooling rate are in agreement as the velocity processing parameter increases in a LPBF build.

When considering the cooling rate with a varying power processing parameter, it is expected that the cooling rate will decrease as the power increases. As the power increases, melt pool dimensions also increase resulting in more molten material and more time needed for it all to cool. The results in this experiment show that the spectral intensity increases as the power processing parameter increases. This disagreement can possibly be attributed to the optical emissions of cooling material that is still glowing. Since the power increases the cooling rate of a melted line, the readings captured by the spectral diode could have been interfered with the previous lines still cooling and giving off intensity.

Increasing the power has also been found to increase the size of the plume above the melt pool in a LPBF build [8]. When a larger, denser plume appears above the melt pool, the optical emissions of this reaction have been known to produce higher light intensity. This also could have interfered with the measurements taken by the diodes during the build. In either case, it was found that the velocity processing parameter influences the spectral intensity recorded during a LPBF much more than the power processing parameter.

This relationship between the power, velocity, and spectral intensity was analyzed first by individual effects of each of the processing parameters on the measured intensity values. Then by analyzing the combined effect both of the processing parameters have on the spectral intensity measured. This analysis lead to the development of a spectral

intensity estimating formula with two input variables; power and velocity referred to in this document as Harvey's Theorem.

As stated before, the estimated intensity values generated by Harvey's Theorem are not exact in that there is some slight deviation between the surface and some of the points representing the average spectral intensity values measured in this experiment. This can be attributed to a number of things. The most probable is that fact that there are only fifteen data sets to analyze and try to draw conclusions from. There are an infinite number of combinations of the processing parameters that could be utilized in repeating this experiment. Repeating this experiment with a great deal more combinations of processing parameters would generate more accurate results and could possibly eliminate some of the error found in the current fifteen data sets such as the unexplained spikes in the P=450 W, V=1000 mm/s and P=300 W, V=1000 mm/s data sets. Another source of the error could be the result of the experimental setup or experiment situations. Some of the lines could have had more, less, or differently sized powder particles at the printing locations. There could have been some slight variations in the power or velocity as the machine changes printing locations rapidly. Another source of error could have been noise recorded on a line that was printed while the previous line was still cooling causing the intensity reading to be a combination from two sources rather than the current melt pool.

The numerical estimation of spectral intensity based on processing parameter inputs would greatly benefit from collecting a larger sample size of combinations as well more build geometries being considered. This project analyzed fifteen single beads with

varying processing parameters but AM builds generally consist of thousands of weld beads in contact with each other as well as layered on top of one another for multiple layers. Similar analysis performed on full LPBF builds would contribute greatly to the accuracy of the numerical estimation of spectral intensity measured during the builds.

2.7 Conclusion

The major take away from this experiment is the direct correlation between the processing parameters of a LPBF build and the spectral intensity recorded during the build process. When power or velocity increases or decreases in a LPBF build, the spectral intensity measured will also increase or decrease accordingly. The velocity processing parameter will affect the measured spectral intensity more than the power processing parameter however, their individual effects on the spectral intensity are significant as well as their combined effects. With all of the sources of error considered, it can be stated that the results from this experiment are significant and display a definite correlation between the power and velocity processing parameters of a laser powder bed fusion build and the spectroscopy data collected during the print. However, what the intensity reactions physically relate to in the LPBF process could not be determined in this experiment.

It also can be said that the foundation of a mathematical formula has been developed through this work that can be used to calculate the expected spectral intensity measured during a LPBF in the broadband visible light spectrum, the 520 nm wavelength, and the 530 nm wavelengths with a high degree of reliability. The results from this experiment would greatly benefit from more experiments of similar nature to

increase the sample sizes and the combinations of processing parameters that would lead to the development of better results.

2.7.1 Carryover to Big Little Experiment

The results from this experiment can carry over and impact the results collected from the Big Little Experiment. The most significant result that would be carried over is the estimated values for the intensity. Using Harvey's Theorem, the value for the intensity data of the big and little builds would be estimated and used to help identify spikes and low points in the spectral intensity data which is hypothesized to correlate to defects within the LPBF printed parts.

Chapter 3 Analysis of In-situ Spectroscopy Data of Laser Powder Bed Fusion Build (Big Little Experiment)

3.1 Introduction

An experiment was conducted with the goal of correlating in-situ collected spectroscopy data of a LPBF build to defects detected in the parts printed post build. This was performed by building two individual cuboids referred to as the “big” and “little” builds. These parts were printed side-by-side in a LPBF machine while a system of diodes would be constantly scanning the build chamber for intensities of different spectrums. This spectroscopy data would be analyzed and compared to CT scanning analysis data that was performed on the big and little cuboids after they were removed from the build plate. It is hypothesized that anomalies found in the in-situ collected spectroscopy date will have a correlation with a porosity analysis performed by the CT scanning post build. The anomalies of the in-situ collected spectroscopy data found was the primary focus of analysis during this experiment. A comparison between the results found by this analysis (single wavelength of 520 nm, 530 nm, and broadband) and the results found by using the documented method of the line to continuum ratio was also made.

3.2 Theory

The theory being tested in this experiment is the relationship between in-situ collected spectroscopy readings of a LPBF build and defects located within the build.

Based on the current understanding of defects in LPBF, too much energy will cause keyholing porosity in the build material and too little energy can result in lack of fusion porosity [43]. Changing the build geometry will also change the amount of porosity in the material because of the amount of material that heat can conduct through. The ability for the pores to be monitored using spectroscopy will be determined in this chapter.

3.3 Experiment Setup

3.3.1 Build

The build for this experiment consists of two individual cuboids that would be printed side by side in the build chamber. The larger of the two cuboids, which is referred to as the "big", has dimensions of 10mm by 10mm by 10mm. The smaller of the two, or the "little", has the dimensions of 3mm by 3mm by 10mm. These would be built by two-hundred twenty five layers of thickness of approximately 40μm. Figure 3.1 displays a CAD model and a dimensional drawing, in inches, of the big and little cuboids on the build plate.

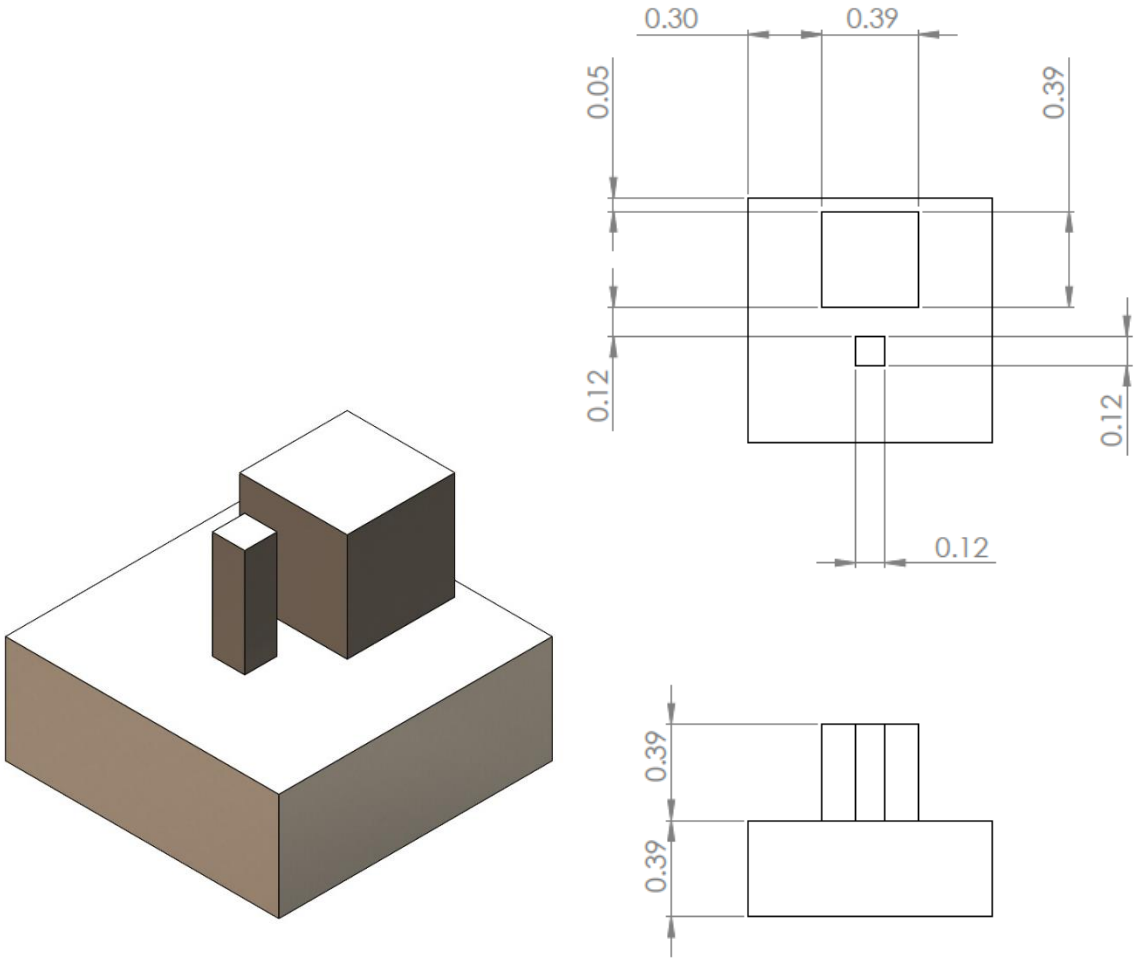

Figure 3.1 Big Little Experiment CAD Rendering

Figure 3.2 is an image of the big and little cuboids as well as the build plate they were removed from after the build was completed for analysis.

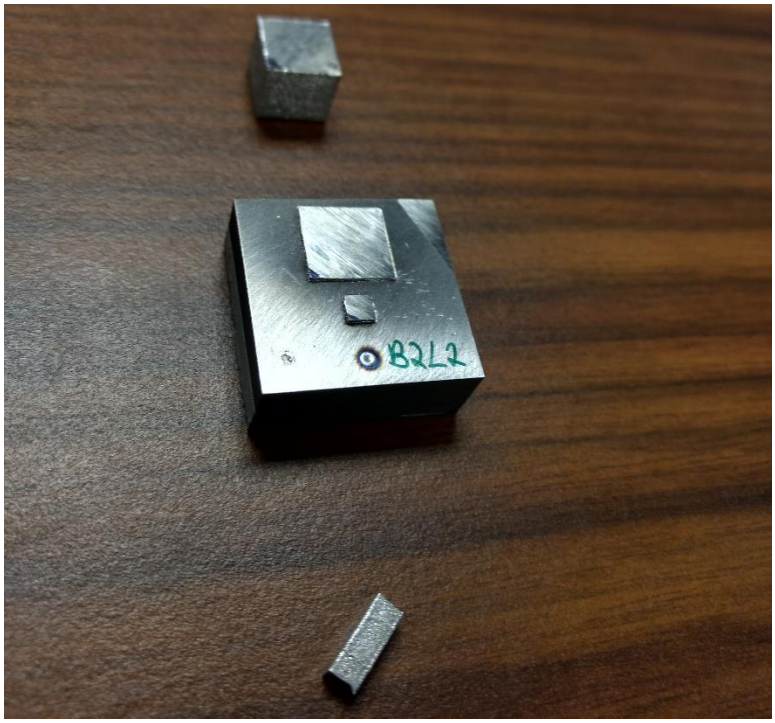

Figure 3.2 Big and Little Builds Removed from Build Plate

It can be seen in Figure 3.2 that some of the material from the big and little cuboids remained on the build plate during removal via wire saw. This will be considered later during the layer by layer analysis of the builds since some of the information pertaining to defects in the leftover sections will have been lost.

3.3.2 Machine

The machine used for the Big Little Experiment is the same early adaptation of the Open Additive Panda LPBF machine that was used to print the fifteen individual weld beads in the Variable Experiment. This machine is fitted with an adjustable laser up to 500 W with a build volume of 4in by 4in by 2in. It was also be equipped with the same assortment of diodes monitoring the intensity of the build chamber during the build.

Figure 2.3 shows an Open Additive laser powder bed fusion machine that was developed after the early adaptation used in this experiment for production.

3.3.3 Material

Similar to the variable experiment, Inconel 718 powder was used to print the big and little cuboids analyzed in this experiment. This material was used for its high chemical purity, low porosity, high stacking density, ability to evenly flow. Inconel 718 is a common material used in LPBF applications.

3.3.4 Monitoring Setup

Similar to the single bead experiment described earlier, the series of diodes for this experiment consisted of three sensors. One collecting broadband spectral intensity data, one with a filter to collect only the 520 nm wavelength intensity, and the third collecting only the 530 nm wavelength intensities. Again, the data collected from these diodes were exported into csv files for later analysis, each layer would produce an individual csv file containing the readings from all three diodes.

3.3.5 Processing Parameters

The processing parameters that were used to print both the big and little cuboids in this experiment were as follows, power P=400 W and velocity V=750 mm/s.

3.3.6 Scan Patterns

The scanning strategy consisted of printing each layer in side-by-side stripes covering the whole layer. For each new layer, the printing pattern was rotated 45° counterclockwise from the previous layer. The first layer started printing in the bottom right hand side of each of the parts when looking down from the top. The next layer

would start in the same location but the scan direction would be different by the 45°. After 2 successive layers starting at the same location, the start point would be moved by one corner in the counterclockwise direction. The scan patter would also be rotated by the same 45° as each layer prior. This pattern would continue to repeat eight times before the same pattern would reset. Figure 3.3 shows the eight different patterns that would be used to print the parts.

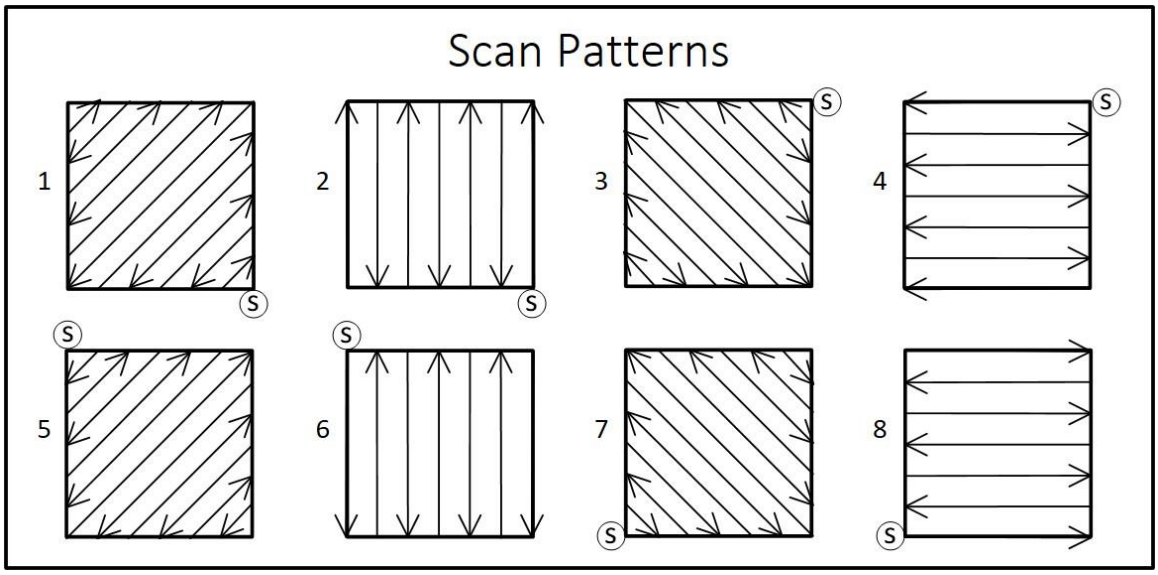

Figure 3.3 Scan Patterns of the Build

The circle encompassing the S in Figure 3.3 represents the corner where the layer print would begin and the arrows represent a general spread out representation of the each of the layer patterns.

The patterns shown in Figure 3.3 were used for both the big and little cuboids for each layer. The LPBF machine first used one of the above layer scanning strategies to print one layer of the big cuboid, then repeated the same scanning strategy for one layer

of the little cuboid. Once one layer was completed and a new layer of powder material was spread, the machine would apply the next scan pattern for the big and then the little cuboid. This repeated until both of the builds were finished.

3.4 Analysis

The extraction and analysis of the in-situ collected spectroscopy data was performed primarily on *MATLAB* due to its ability to import and process large amounts of data from csv files efficiently. The analysis consisted of first extracting the spectroscopy data from the csv files and then isolating the data pertaining to the printing of each of the cuboids from the data that corresponds to the time before and after the layer was printing. This was performed for all three spectral wavelengths that the diodes were monitoring intensity levels in. Once each of the individual layers were isolated for the big and little cuboids and for each of the three intensities used for measurement, the individual properties of each layer were determined. The main property of focus is the average spectral intensity of each of the layers of the builds. Much of the analysis for the Big Little Experiment is similar to the analysis performed in the Variable Experiment which determined spectral intensity properties of fifteen individual weld beads.

3.4.1 Extracting Spectroscopy Data

The spectroscopy data recorded during the build of the big and little cuboids was exported into csv files. Each layer printed during the build generated a single .csv file that consists of intensity data for both the large and small part. The different measured intensities, broadband, 520 nm, 530 nm were separated into different columns in the .csv file and each row was filled in by the corresponding spectral intensity at that point. Table

3.1 displays an example of the format of the .csv files that were generated as the parts were being printed.

Table 3.1 Example of .csv file Format

AIN0 - 520	AIN1 - 530	AIN2 - Broadband
0.016248	0.010879	0.00491
0.014353	0.01151	0.0046
0.014037	0.01151	0.0046
0.014984	0.012774	0.00491
0.016248	0.012458	0.00428

Using the built in *MATLAB* function “csvread” each of the spectral intensity data sets were imported into *MATLAB* for each layer as a matrix of dimension one by the number of intensity data points for that layer. This process was repeated for all two hundred twenty five printed layers and for all three of the spectrums used in this experiment.

One problem with the imported spectral intensity layer data is that it includes both the big and little builds in one data set as well as the time before, between, and after the actual printing. These instances where non-printing was recorded needed to be disregarded in the data analysis. Because of this, the big and little build intensity data sets needed to be separated from each other and then isolated to just the printing data to discard the data recorded before and after the parts were being printed. Figure 3.4 shows a plot of the broadband spectral intensity reading for the first layer of the builds.

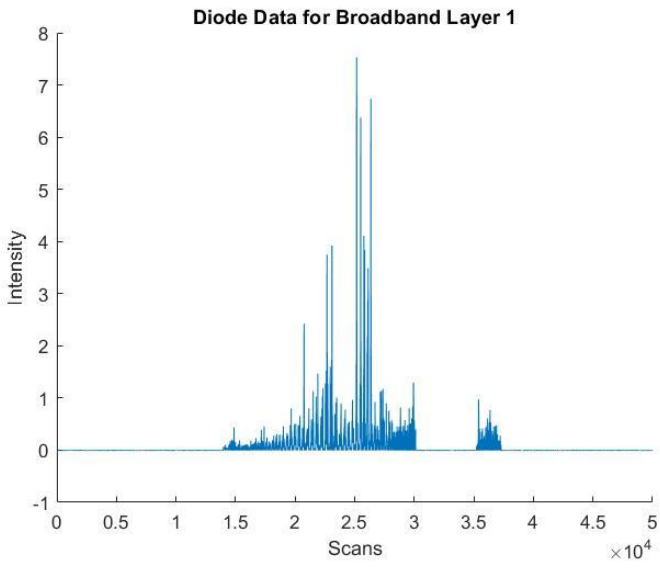

Figure 3.4 Diode Data for Broadband Layer 1

Observing Figure 3.4, it is clear at which points the big part starts being printed, then where it stops, and where the little part starts and stops being built. The next step in the data analysis was constructing a *MATLAB* script that would reduce each layer's data into two separate sets that consist only of the large and small active printing data sets respectively for each layer for each of the wavelengths used.

3.4.2 Separating Builds

A *MATLAB* function was created to separate and isolate the spectral intensity data for the big and little parts for each of the layers of the build. This function separates and isolates the data in five steps. The first step the function performs is copying a vector of the layer spectral intensity data. Figure 3.5 shows the copied intensity data set for the first layer recorded in the broadband spectrum.

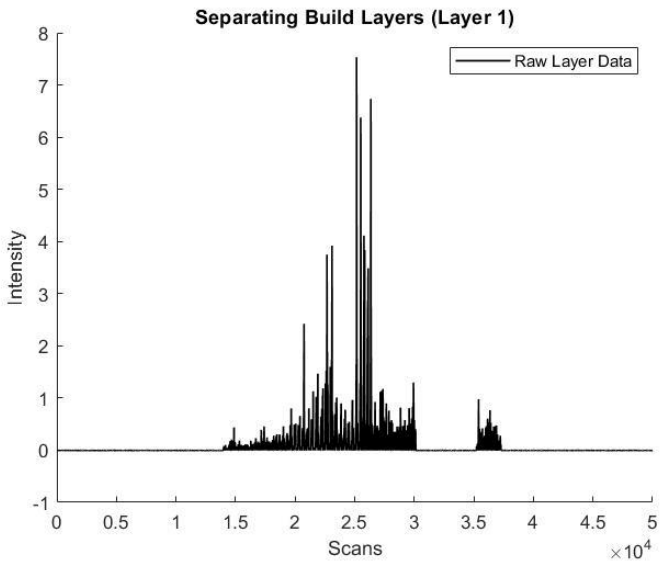

Figure 3.5 Separating Broadband Builds Layer 1 Raw Data

The second step the *MATLAB* function performed was generating a tolerance line to compare to the rest of the data. This tolerance line is referred to as the "Tline." The Tline is generated by taking the mode of the entire layer data set and adding 5% to it. Equation 3.1 shows the calculation used to generate the Tline of the data for each of the layers of the build.

$$Tline = mode(LayerDataSet) \times 1.05$$

Equation 3.1 Tolerance Line (Tline)

The mode was used in this calculation due to the large amounts of intensity readings equaling zero. The majority of these instances occur in the space before, between, and after the printing of the large and small parts. Since the goal is to eliminate these areas of the data, the extra 5% was added to the Tline calculation before anything was compared

to it. Figure 3.6 displays the original layer data pictured in black and the Tline, shown in green, laid over top of the original data.

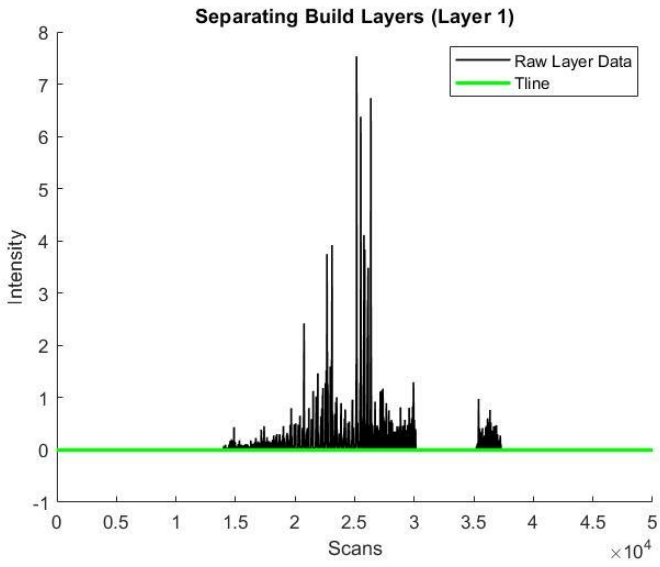

Figure 3.6 Separating Broadband Builds Layer 1 Tline

The third step for separation and isolation would take the layer data set and smooth it to reduce the noise. This was performed with the built in *MATLAB* function "smoothdata" which performs a Gaussian noise reduction to the data with a window of one thousand data points. Figure 3.7 displays the layer noise reduced broadband data set for the first layer of the build in red, laid over top of the original layer data set and the layer Tline.

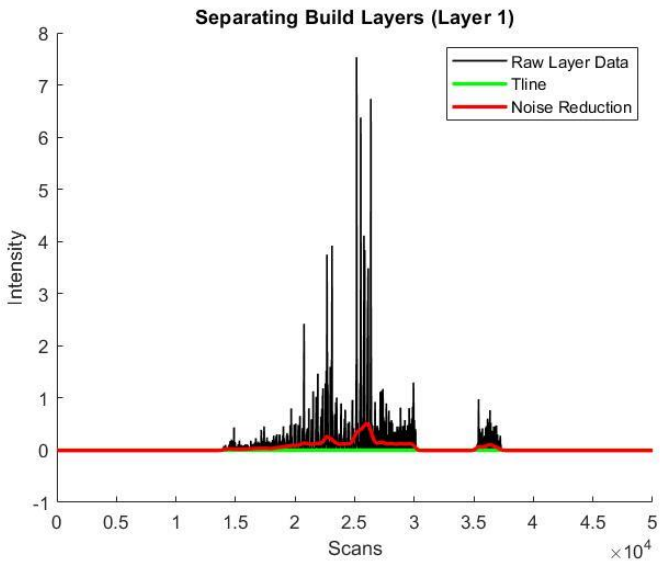

Figure 3.7 Separating Broadband Builds Layer 1 Noise Reduction

Observing Figure 3.7, the noise reduction plot of the layer data follows the general trend of the entire data set as it spikes and drops for the printing of the large and the small parts. Also by observation of Figure 3.7, the reduced data line is greater than the Tline only during the times when the large and small parts are being printed. This is key for the separation and isolation of the build intensity data sets.

The fourth step in the process is determining where the smoothed data is greater than the Tline. As mentioned above, the smoothed data is greater than the Tline only when the parts are being printed. With this knowledge, the big cuboid data set is isolated by recording the original layer intensity data from when the smoothed data first crosses over to greater than the Tline to when it first crosses back down to lower than the Tline. Similarly, the little cuboid data set uses the second time the smoothed data crossed to greater than the Tline and ends when it crosses back to less than the Tline. Figure 3.8

shows, in blue, the isolated intensity data sets of the large and small parts for first layer of the broadband spectrum.

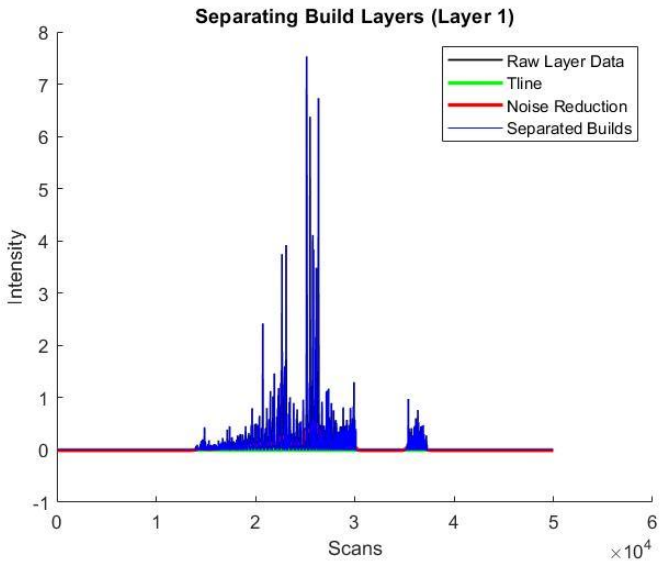

Figure 3.8 Separating Broadband Builds Layer 1 Separated Builds

Observing Figure 3.8, the intensity data sets for the large and small builds are clearly isolated from the instances before, between, and after the printing locations and are noticeably separate from each other.

The last process the created MATLAB function performed was representing the isolated and separated data sets into two easier to manage vectors. Two vectors were generated for each of the layers. The first consists of the spectroscopy data collected during the big part printing and the second consists of the data collected during the little part data set.

Similar to the analysis performed in the variable experiment, the start and end points for the printing locations are much more defined in the broadband data. Because of

this, the start and end points found during the broadband analysis were used for the 520 nm and the 530 nm intensity data sets. Figure 3.9 shows the raw 520 nm and 530 nm spectral intensity data for the first layer of the big and little cuboids respectively.

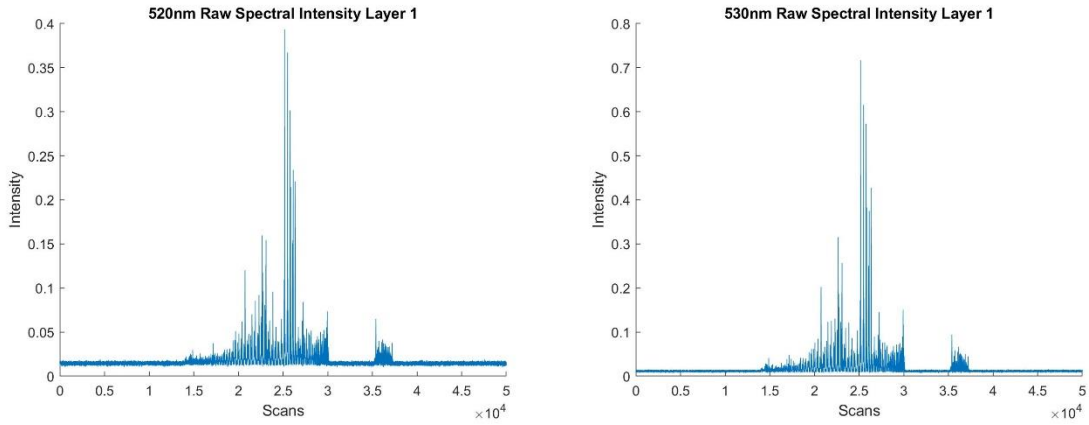

Figure 3.9 Raw Spectral Intensity for Layer 1 520 nm and 530 nm

It can be seen in Figure 3.9 that both the start and end points for the big and little cuboids are less defined due to the noise recorded around those instances by the diodes. Figure 3.10 displays the separated spectral build data for the big and little cuboids for the 520 nm and 530 nm wavelengths respectively.

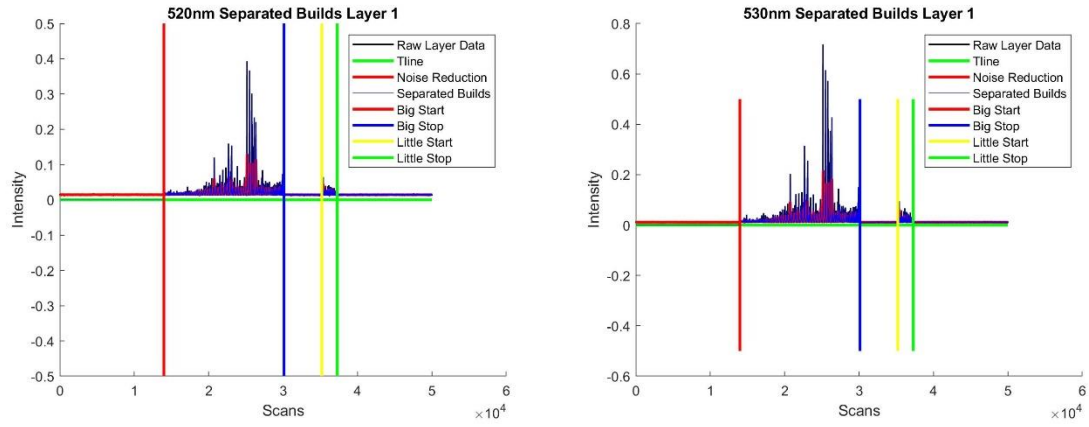

Figure 3.10 Separated Spectral Intensity for Layer 1 520 nm and 530 nm

It can be seen in Figure 3.10 that the start and end points found by analyzing the broadband data for the first layer align with the start and end points of the builds in the other two spectrums observed in this experiment. This analytical process would be repeated for the remaining two hundred twenty four layers of each of the builds in order to separate the spectroscopy data pertaining to only the building locations in each of the spectrums observed.

3.5 Layer by Layer Analysis

Once all two hundred twenty five spectroscopy layer data sets were isolated for the big and little cuboids in each of the spectrums, a layer by layer analysis was performed. The main analytical focus of the layer by layer analysis is the average spectral intensity measured across each of the layers. The average intensity of each layer was compared later to CT scans performed on the big and little parts that located defects within the builds.

3.5.1 Average Intensity per Layer

Figure 3.11 displays the average broadband intensities that were measured across each of the layers of the big and little builds. The left displays the average broadband intensities for the big cuboid and the right displays the little cuboid data.

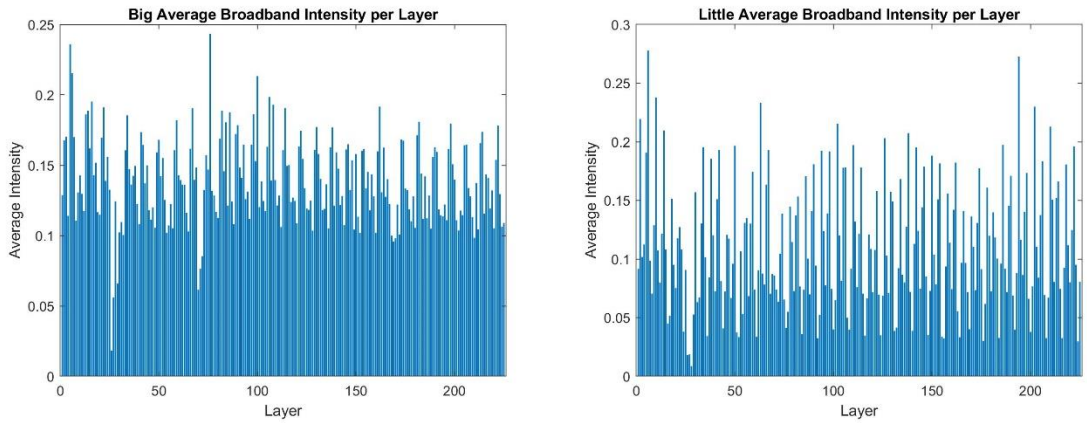

Figure 3.11 Average Broadband Intensity per Layer

Visually in Figure 3.11, it can be seen that there are two significant drop offs in the average broadband intensity data. The first drop off occurs during layer 26 of the builds. This can be attributed to a known error during the printing of the two parts were the machine spread an insufficient amount of powder for layer which resulted in an intensity phenomenon. Unfortunately, this layer was destroyed during the removal of the parts from the build plate so the broadband spectroscopy data would not be able to be compared to potential defects found at this layer. The second drop in intensity occurred at layer 70. This drop in intensity can also be attributed to a known error that occurred during the printing of the big and little. The error that occurred here is an extra thick spread of powder for the layer. Because there was an access amount of powder spread on this layer, the effect of this error can be seen the proceeding few layers average intensity measurements before the data appears to return to normal.

The rest of the average broadband layer intensity data for both the big and the little builds shows a large quantity of spikes and drop-offs of a much smaller magnitude

than the two errors in the printing. This pattern of spikes and drop-offs will be compared to the pore locations found during the CT scans of the big and little builds.

Figure 3.12 displays the average 520 nm intensity measured across each of the layers for the big and little builds on the left and right respectively.

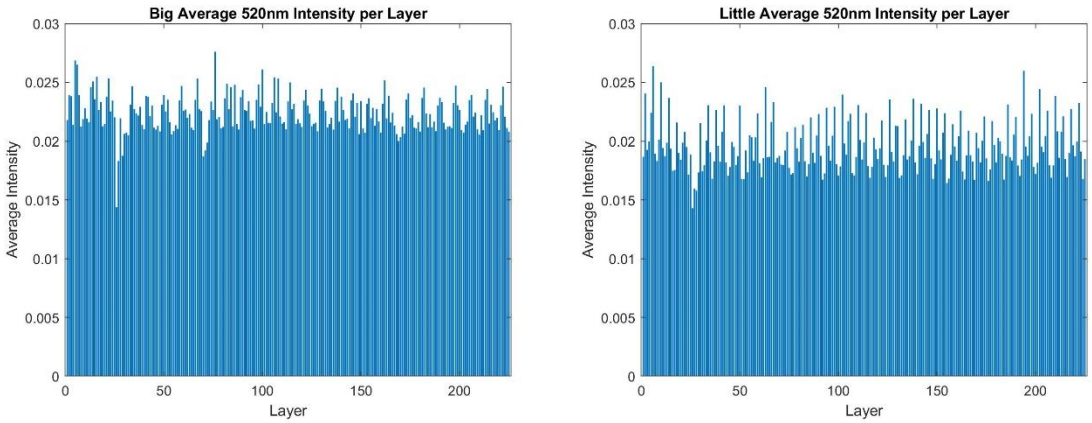

Figure 3.12 Average 520 nm Intensity per Layer

Similar to the average broadband intensity data, the average 520 nm data shows two drop-offs corresponding to the two printing error that were present in the build of the big and little cuboids. The magnitude of the drop-offs appear to be less significant in the average 520 nm intensity compared to the broadband.

The rest of the average 520 nm layer data consists of a number of spikes and drop-offs in in intensity that will be compared to the CT scan data to determine if there is a correlation between the shape and the number of pores in the layer.

Figure 3.13 shows the average 530 nm intensity measured across each of the build layers for the big and little cuboids. The left displays the average 530 nm layer intensity of the big build and the right displays the data pertaining to the little build.

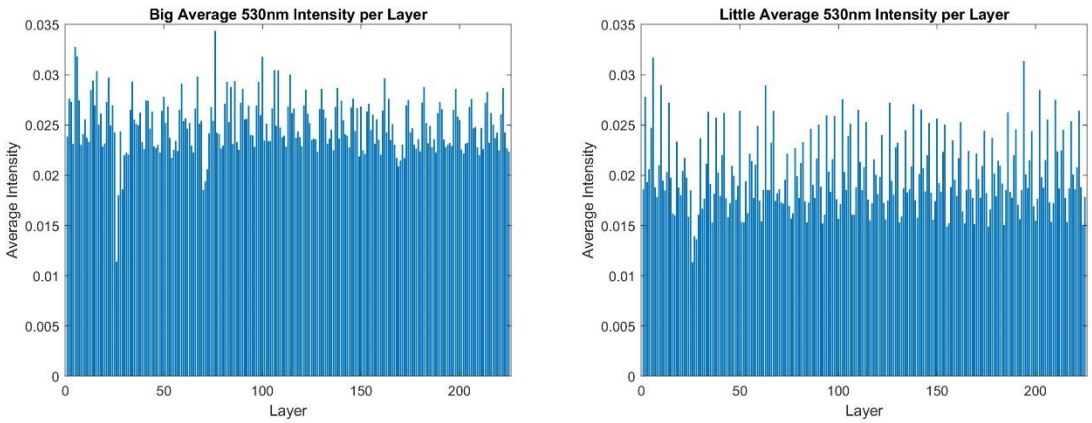

Figure 3.13 Average 530 nm Intensity per Layer

Similar to the average 520 nm and broadband layer intensity data, the average 530 nm layer intensity data shows two significant drop-offs corresponding to the two printing errors that occurred during the build. Also similar are the spikes and drop-offs in the remanding sections of the data that will be compared to the pore locations found by the CT scans.

In all of the average intensity per layer figures, it can be seen that the big part tended to have higher average intensity values than what was recorded for the little part. This difference in average intensities can be seen in Figure 3.11, Figure 3.12, and Figure 3.13 which display the average intensities recorded over each layer for each of the spectrums observed in this experiment.

Outside of the two major drop-offs in the average broadband, 520 nm, and 530 nm intensity per layer data, the rest of the data follows a series of spikes and drop-offs. This series will be compared to the pores located by CT scanning the big and the little

builds after they were removed from the build plate. The collection process of the CT data is displayed in the next section.

3.5.2 Line to Continuum Ratio per Layer

Similar to the average spectral intensity per layer analysis performed in the last section, the average line to continuum ratio vale was determined for each layer of the build. Figure 3.14 displays the average line to continuum ratio values for each layer of the big and little builds.

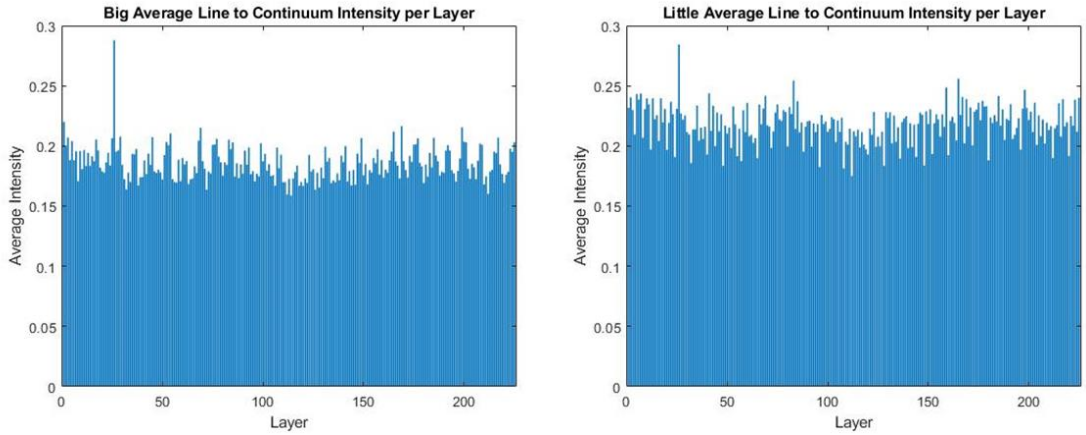

Figure 3.14 Average Line to Continuum Intensity per Layer

The line to continuum per layer appears to show the opposite trends than the average intensities per layer. The big build has a typically lower line to continuum compared to the little build. It also appears that drops in the average intensity per layer data are represented as spikes in the line to continuum per layer.

3.6 CT Data

The main property that needed to be extracted in the CT data is the number of pores found per layer. These values could be compared to the average spectral intensity

measured across each of the layer in the big and little for all three of the spectrums measured in this experiment.

3.6.1 Porosity Analysis

Once the big and little were removed from the build plate, they were both subjected to CT scanning to determine the porosity of the parts. Figure 3.15 displays the 3D model generated by the CT scanning porosity analysis of the big part.

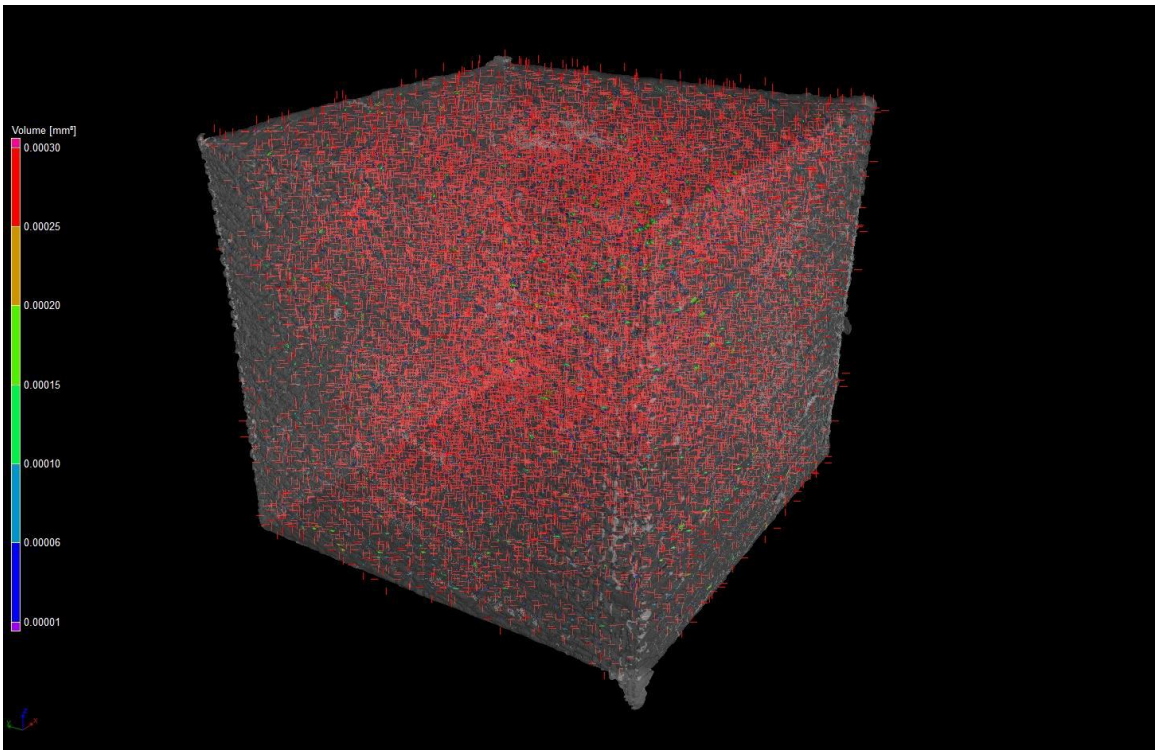

Figure 3.15 Big CT Porosity Analysis

Visually it appears that the pores present in the big cuboid are spread uniformly throughout the build. A dimensional analysis was performed that separates the location of pores by the z-dimension in the next section. Figure 3.16 displays the 3D generated CT porosity analysis for the little cuboid.

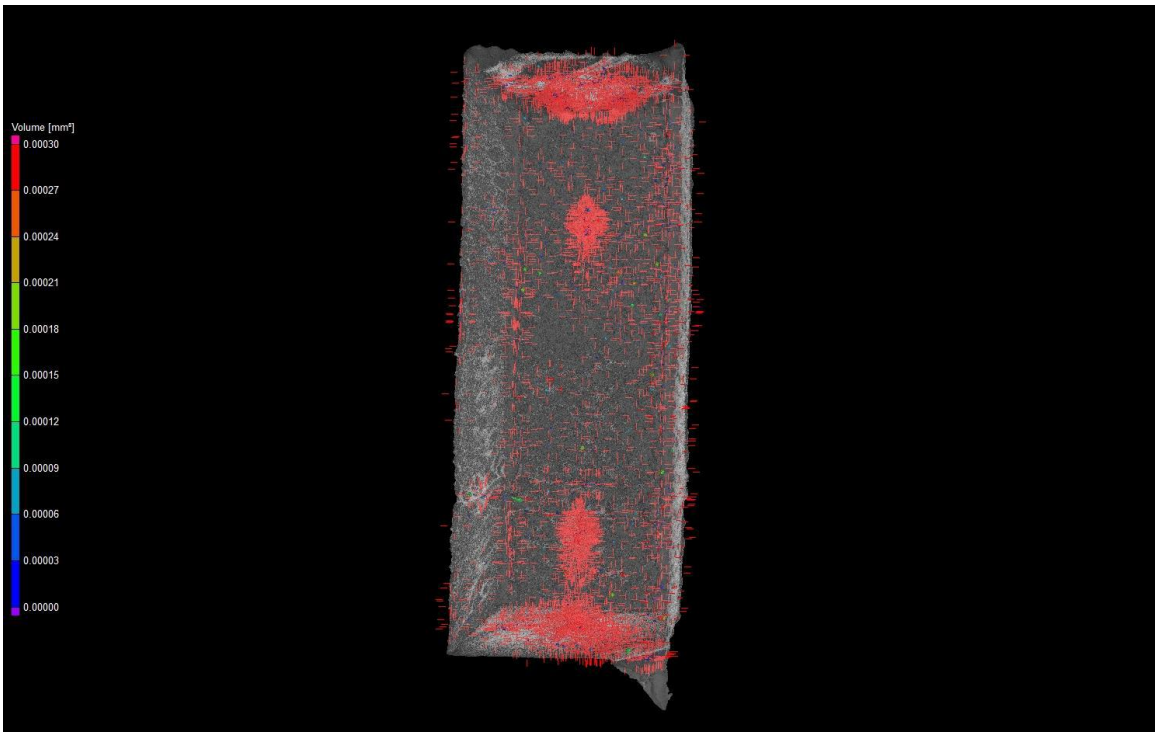

Figure 3.16 Little CT Porosity Analysis

Visually it can be seen that there are pore concentrations located within the little build near the top and bottom of the as well as two cluster groups in the center of the build. The same dimensional analysis for pore location in the little build is described in the next section.

3.6.2 Number of Pores per Layer

The format of the CT scan data was received as a measurement of the volume of a pore as well as the location in 3D space of its center in (x, y, z) coordinates. The main focus of analysis is only the z-coordinate of the pore location relative to the top of the big and little cuboids since the bottom of each had a significant portion lost when the parts were removed from the build plate.

One issue that arose is the extraction is that the CT scanning pore coordinates are accurate to within 0.01μm. Because of this, layer zones were created to organize the pore locations into two hundred twenty-five layers to be comparable to the layers in the spectroscopy data. These zones were created by dividing the 10mm height of the big and little cuboids by the two hundred twenty five layers of printing then using interpolation to create the z-dimension barriers for each of the layers.

Once the zones were created, a *MATLAB* script was generated to organize each pore found by the CT scans into its corresponding layer zone and record the number of pores in that zone. This was performed for both the big and the little builds. Figure 3.17 displays the distribution of the pores found by CT scanning the big build in terms of the printing layers.

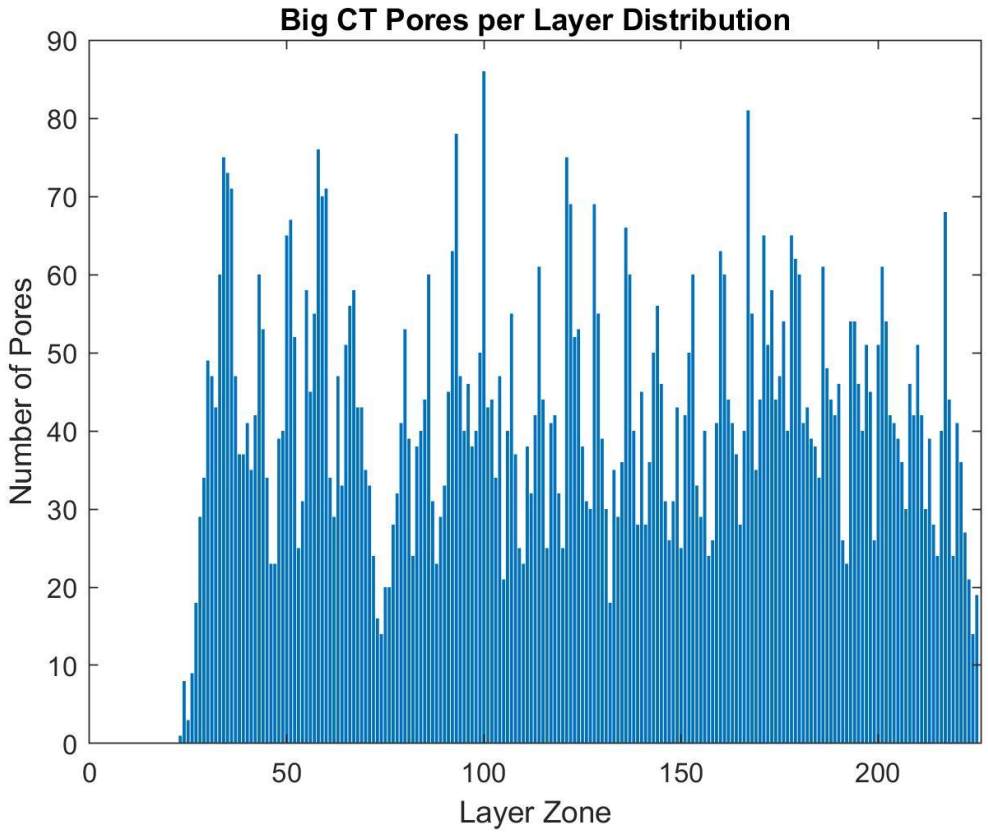

Figure 3.17 Big CT Pores per Layer

It can be seen in Figure 3.17 that a significant amount of data was lost in the lower sections of the build once it was cut off from the build plate. The rest of the pore distribution appears to spike and drop-off similar to the average intensity behavior observed in the previous section.

Figure 3.18 displays the distribution of the pores found by CT scanning the little build in terms of the printing layers.

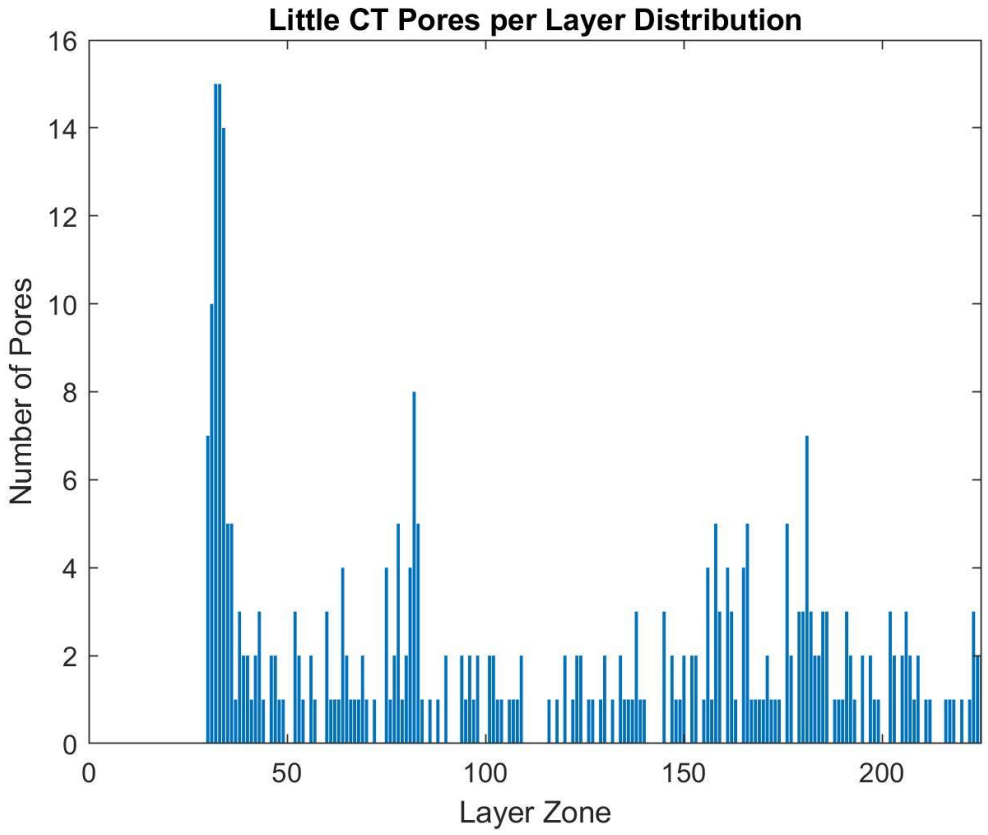

Figure 3.18 Little CT Pores per Layer

Similar to the pores per layer found in the big build, the little build pore distribution shows a significant loss of data in the lower section of the build. It also shows a series of spikes and drop-offs in the number of pores per build layer that will be compared to the average spectral intensities per layer. The magnitude of the number of pores in the little build is significantly less than that of the big build. The maximum number of pores in a layer of the little build is fifteen whereas the maximum in one layer of the big build is eighty six. This is likely due to the fact that the big cuboid has a larger cross-sectional area than the little build which give more space to contain pores.

The pore distributions for the big and little cuboids are comparable to the average broadband, 520 nm, and 530 nm spectral intensities that were recorded across the build layers since they both show a trend of spikes and drop-offs for a majority of the builds.

3.7 Results

The comparison results in this experiment fall into two categories. The first of which is a straight layer-by-layer analysis of the average broadband, 520 nm, and 530 nm spectral intensities to the number pores per layer determined by the CT scanning. The second category consists of a relative comparison where groups of average spectral layer data is compared multiple layer zones of the pore data using a Gaussian noise reduction.

3.7.1 Layer by Layer

The layer by layer analysis performed in this experiment focuses on the comparison between the average spectral intensity recorded across an entire layer of the big and little builds and the number of pores per layer zone found in the CT data. For the comparison, both the average intensity per layer and the CT pore per layer zone data would be normalized so that that the spikes and drops in the data could be seen in both data sets individually. Figure 3.19 displays the normalized broadband average intensity per layer for the big cuboid as the normalized pores per layer zone found by CT scanning the part post build.

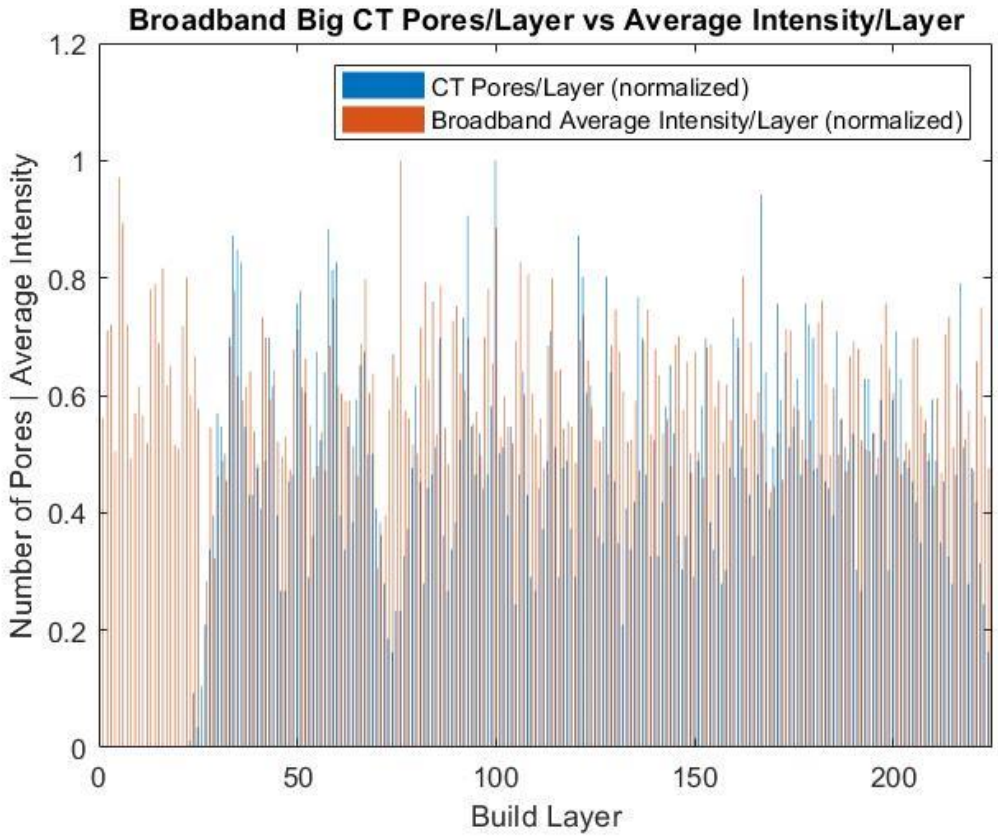

Figure 3.19 Big CT Pores vs Average Broadband Intensity per Layer

Visually it can be seen that the shape of both the average broadband intensity data and the pores per layer tend to contain similar spikes and drops in the same layer data. This is especially noticeable in the layers surrounding the second stop in the data, approximately layer 70. Both the average broadband intensity data and the pores per layer data show a significant drop in in the layers surrounding the printing error however, the CT pore data appears to show the drop a couple of layers after the average broadband intensity data. This same scenario can be seen for the rest of the spikes and drops in the both sets of data. The pores per layer spikes and drops appear two to three layers after they appear in the average broadband intensity data.

The same comparison was performed between the average broadband spectral intensity per layer for the little build and the pores per layer found by CT scanning the little cuboid. Figure 3.20 displays this comparison between the two sets after they were normalized.

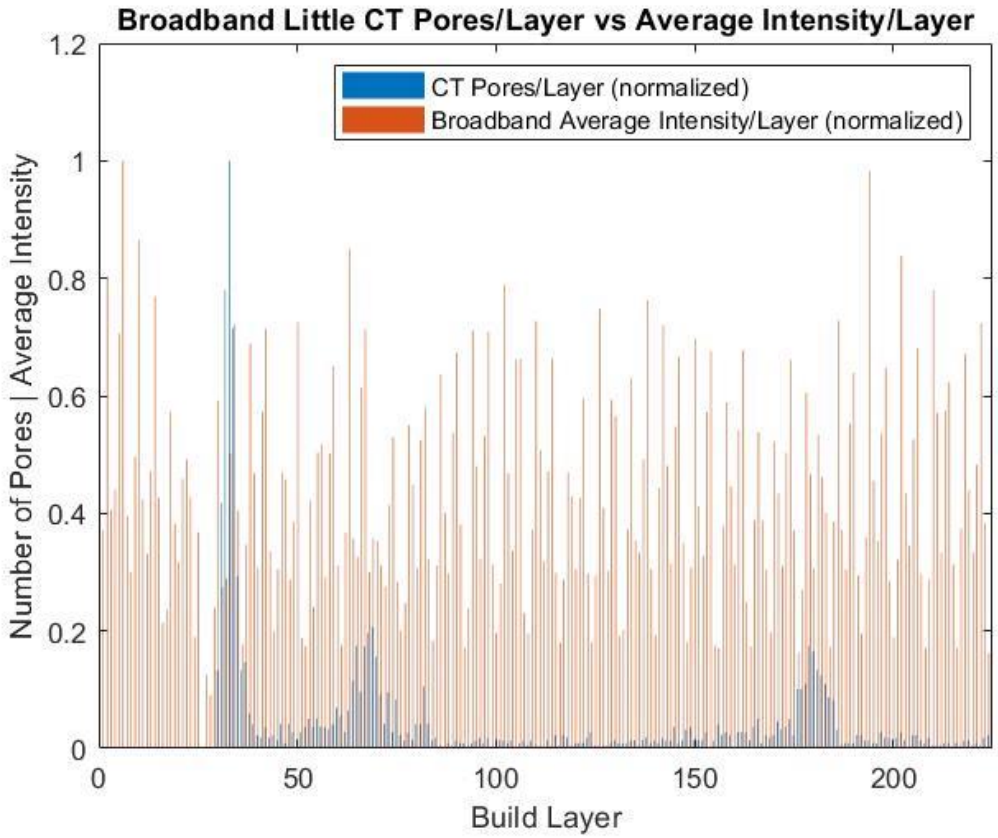

Figure 3.20 Little CT Pores vs Average Broadband Intensity per Layer

Though it is harder to see the similarities between the average broadband intensity data and the pores per layer in the little build, it does still follow the same general trend that was observed in the data comparison of the big cuboid. Both the average broadband intensity per layer and the pores per layer for the little build appear to spike and drop within a two to three layers of each other. However, even after both data sets were

normalized, the magnitude of the spikes and the drops are very different. The normalized average broadband intensity data contains higher differences in the spikes and the drops compared to the pores per layer found in the CT scan of the little build. Future comparative analysis of the big and little pore data with the average spectral intensities will be normalized and adjusted so that both sets of data have the same mean point in order to better compare the spikes and drops.

Figure 3.21 displays the comparison between the normalized average 520 nm intensity per print layer and the normalized number of pores per layer found by CT scanning the big build.

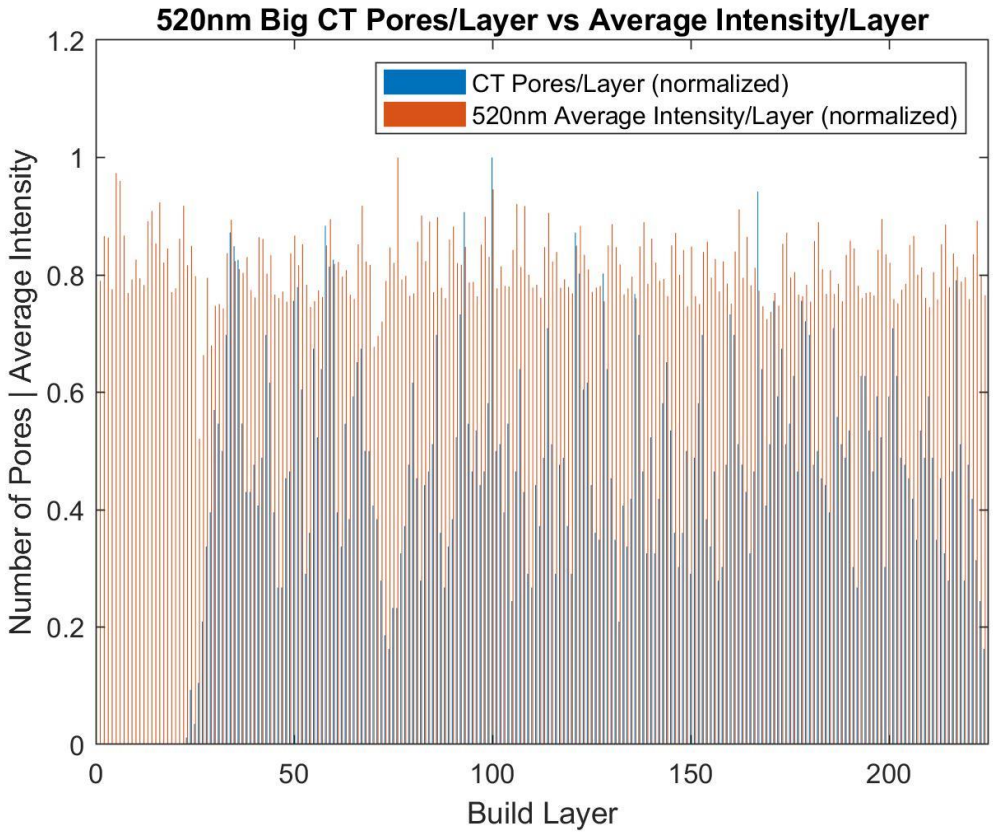

Figure 3.21 Big CT Pores vs Average 520 nm Intensity per Layer

Similar to the normalized average broadband intensity per layer for the big cuboid, the normalized average 520 nm intensity spikes and drops off at the same instances as the pores per layer found by CT scanning the big build. Again, the magnitude of the spikes and drops for each of the data sets are not equal in the normalized data but do appear to be related. This will be further explored in the relative comparison section later where the normalized data sets are adjusted to have the same average value.

The average 520 nm intensity per layer for the little build would also be compared to the number of pores per layer found by CT scanning the little build post-build. The normalized average 520 nm average intensity per layer and the number of pores per layer for the little build are shown in Figure 3.22.

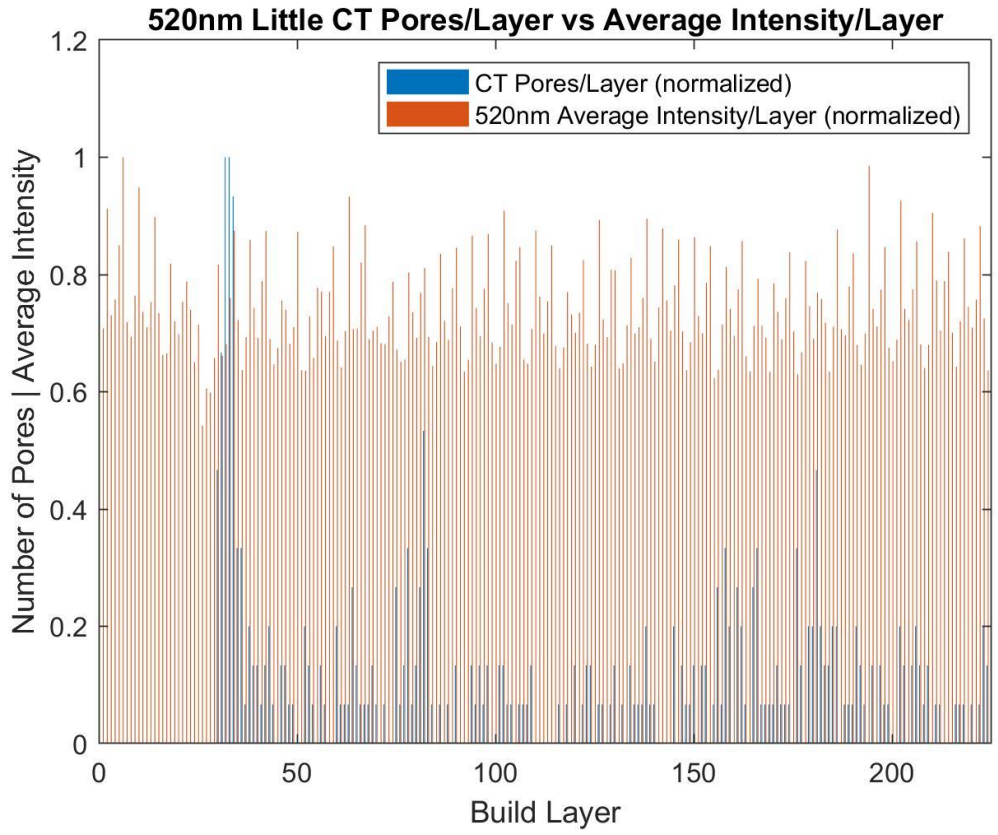

Figure 3.22 Little CT Pores vs Average 520 nm Intensity per Layer

Similar to the normalized average broadband intensity per layer for the little build, the normalized average 520 nm intensity per layer spikes and drops off at the same instances as the pores per layer found by the CT scanning. Again the magnitudes of the spikes and the drops in both sets vastly different and will benefit from an adjustment in future analysis.

The same comparison that was performed on the pores per layer found by CT scanning the parts and the average broadband and 520 nm intensity per layer would be performed using the average 530 nm intensity per layer. Figure 3.23 displays the comparison between the normalized average 530 nm intensity per layer and the

normalized number of pores per layer found by CT scanning the big cuboid after it was removed from the build plate.

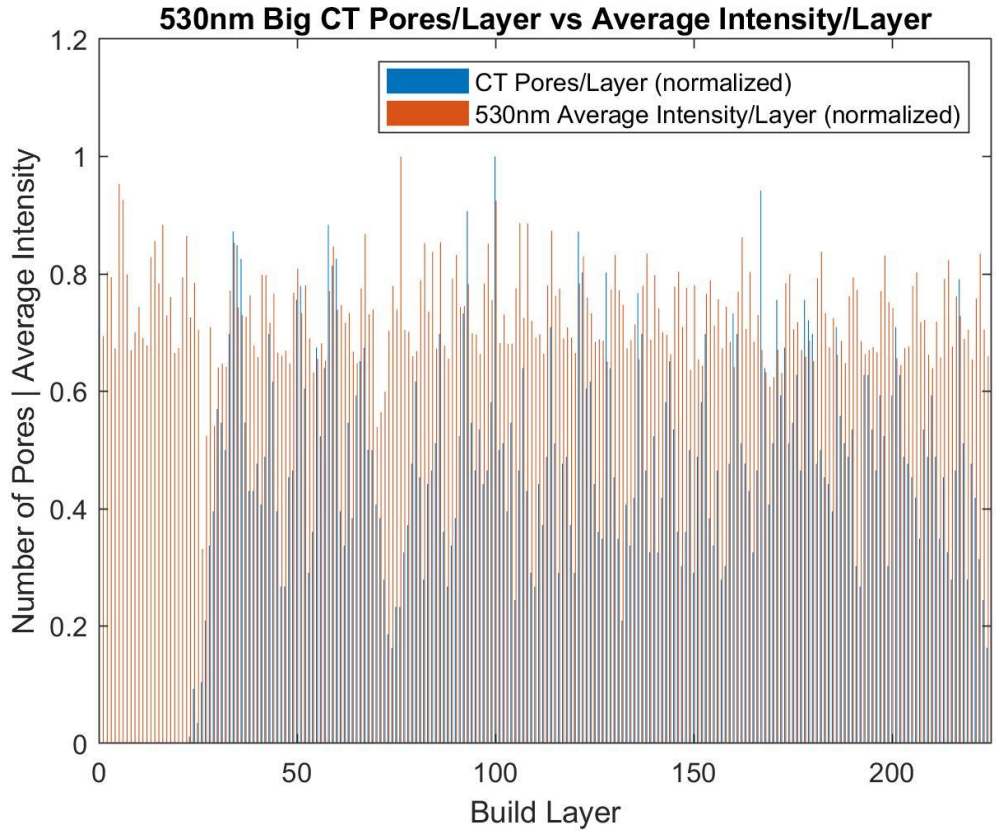

Figure 3.23 Big CT Pores vs Average 530 nm Intensity per Layer

Predictably, the normalized average 530 nm intensity data also follows the same general shape as the normalized pores per layer where spikes and drops occurs at the same instances, especially at the known printing error of layer 70. This relation will be further explored in the relative comparison section once both normalized data sets are adjusted to match average values.

The same analysis was performed using the normalized average 530 nm intensity per layer for the little build and the number of pores per layer for the little build. Figure 3.24 displays the comparison of both of these data sets after they had been normalized.

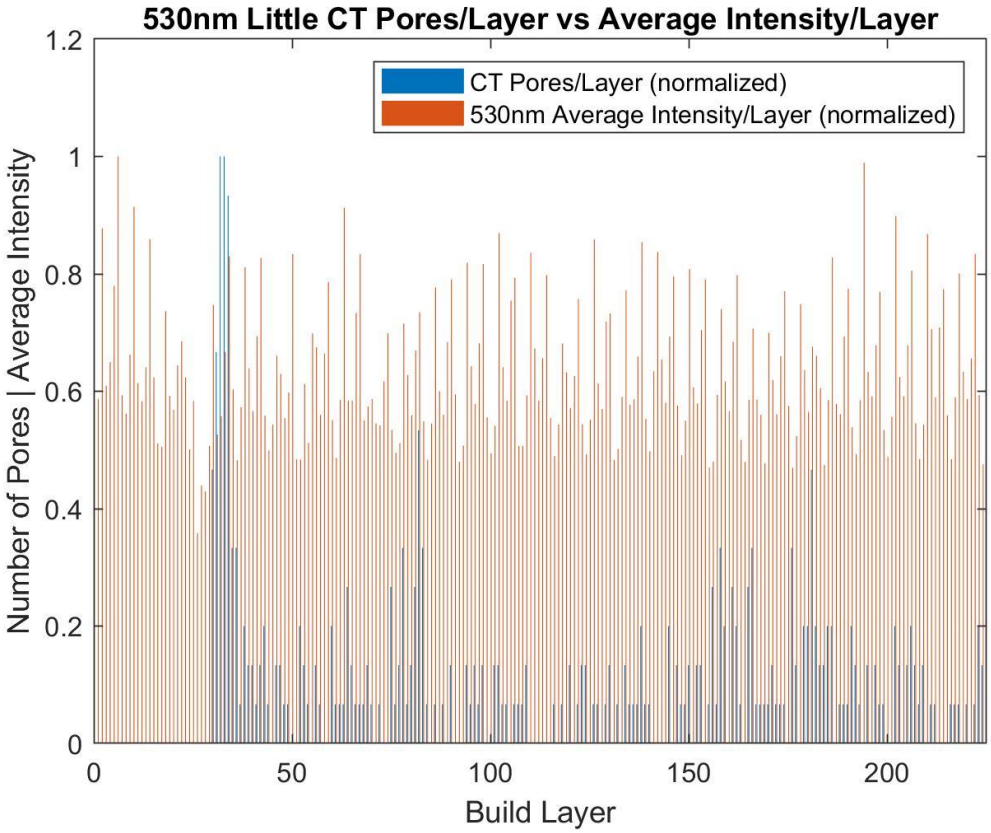

Figure 3.24 Little CT Pores vs Average 530 nm Intensity per Layer

Similar to the comparison of the number of pores per layer in the little build with the average broadband and 520 nm intensities per layer, the average 530 nm intensity per layer follows the same generally trend of matching the instances of spikes and drops with a difference in magnitude.

All of the normalized average spectral intensities per layer for all three of the spectrums observed in this experiment for both the big and little cuboids show spikes and drops in intensity at the same instances that the normalized number of pores per layer. Even though these corresponding spikes and drops occur at the same time, the magnitude of the spike or drop is much different between the spectral intensity and the number of pores per layer. As mentioned previously, the normalized data sets will be later adjusted to have the same average value so the spikes and drops would be easier to interpret.

3.7.2 Relative Comparison

The next step in the analysis was to adjust the normalized data for the number of pores per layer found by the CT scans of the parts and the normalized average intensities per layer. This was performed first by taking the difference between the average value of the entire set of normalized average values for each of the spectrums for both parts and the average number of pores per layer in both of the parts. Next, this calculated difference was added to each of the normalized number of pores per layer data points to bring the average values of both data sets together to better analyze the relationships of spikes and drops.

Both the normalized average spectral intensity per layer and the normalized and adjusted CT pores per layer data sets were “smoothed” in order to see the relative comparison of multiple layers. This was performed using the same Gaussian noise reduction used to separate the build data from non-printing spectroscopy data earlier in the data analysis. However, the noise reduction performed at this step utilized a window

of eight data points which corresponds to eight layers of data to give a relative relationship between multiple layers of average intensity and the number of pores.

Figure 3.25 displays the normalized, adjusted, and smoothed data for the average broadband intensity per layer and number of pores per layer for the large cuboid.

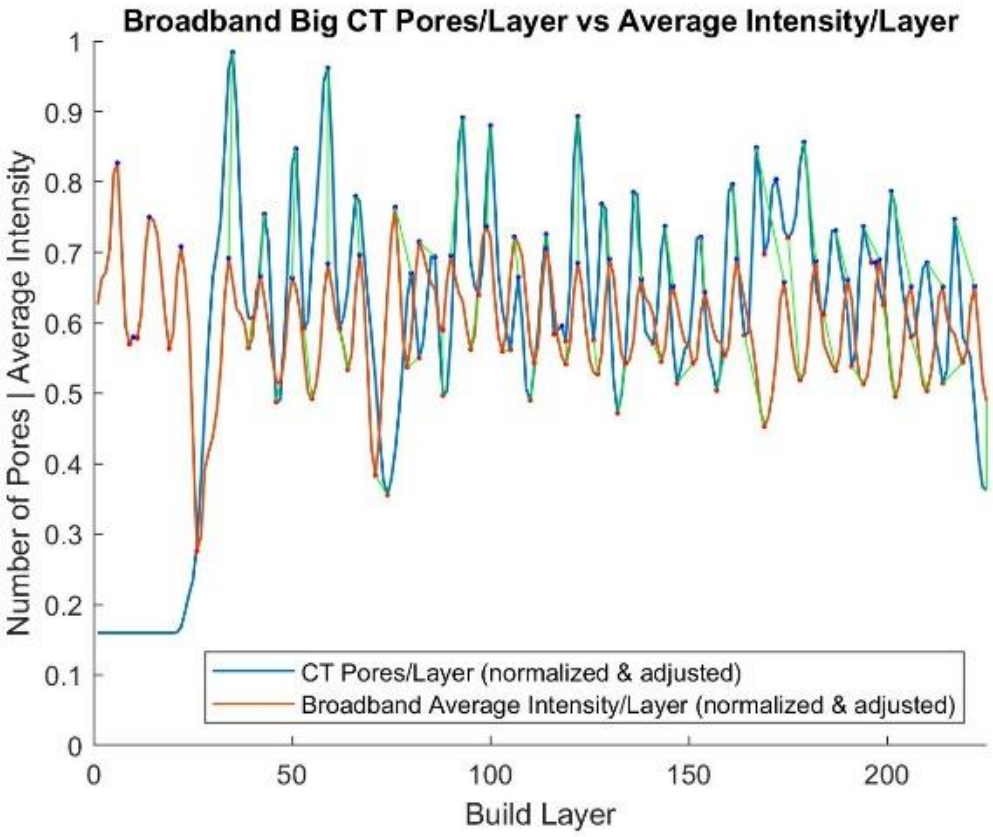

Figure 3.25 Big CT Pores vs Average Broadband Intensity Smoothed

Visually it can be seen that most of the spikes and the drops in each of the data sets appear to occur in the same relative window and most of them in each of the data sets correspond to a spike and drop in the other. This can be seen in the green lines which connect the corresponding spikes and drops in the average broadband intensity per layer

and the number of pores per layer. The green lines show a connection between most of the spikes and drops however, there are some points in both the pores per layer data and the average spectral intensity data that don't have a corresponding point in the other. This can be seen in the beginning group of layers where there measurements for the average broadband intensity has no pore data to be compared to since the bottom section of the big build was lost when removing it from the build plate. The only other non-matching spikes and drops occur in the CT collected pores per layer around layer 175. One extra spike and drop can be observed in the pores per layer in this window. This non-matched extra spike and drop is the only instance where this occurred in the comparison where there is material to compare.

For the little cuboid, the same relationship between the normalized, adjusted, and smoothed data for the average broadband intensity per layer and number of pores per layer can be seen in Figure 3.26.

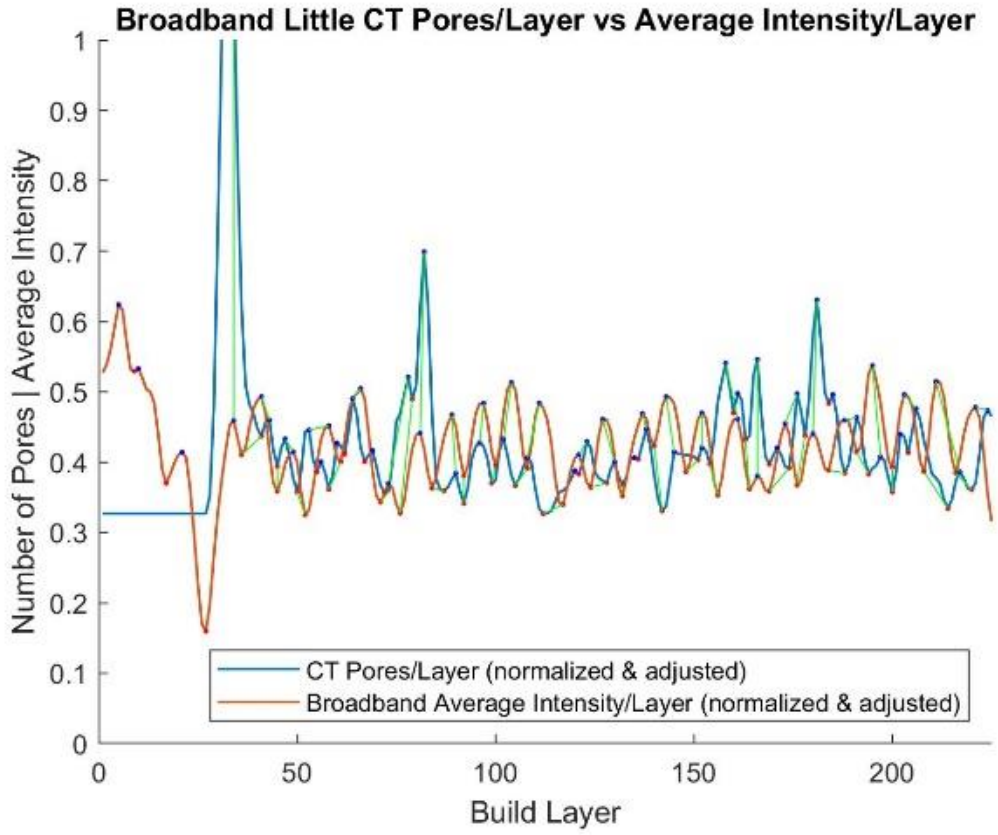

Figure 3.26 Little CT Pores vs Average Broadband Intensity Smoothed

Again, all of the peaks and drops in the CT pores per layer, excluding one extra spike and drop around layer 175 and the lost section of the build, show a corresponding spike and drop in the broadband average intensity per layer. Each corresponding spike and drop in the pores per layer and the average broadband intensity layer are connected by the green lines in Figure 3.26.

The same comparison that was performed using the average broadband intensity per layer for the big and little builds was also performed using the average 520 nm intensity. Figure 3.27 displays the normalized, adjusted, and smoothed data for the average 520 nm intensity per layer and number of pores per layer for the large cuboid.

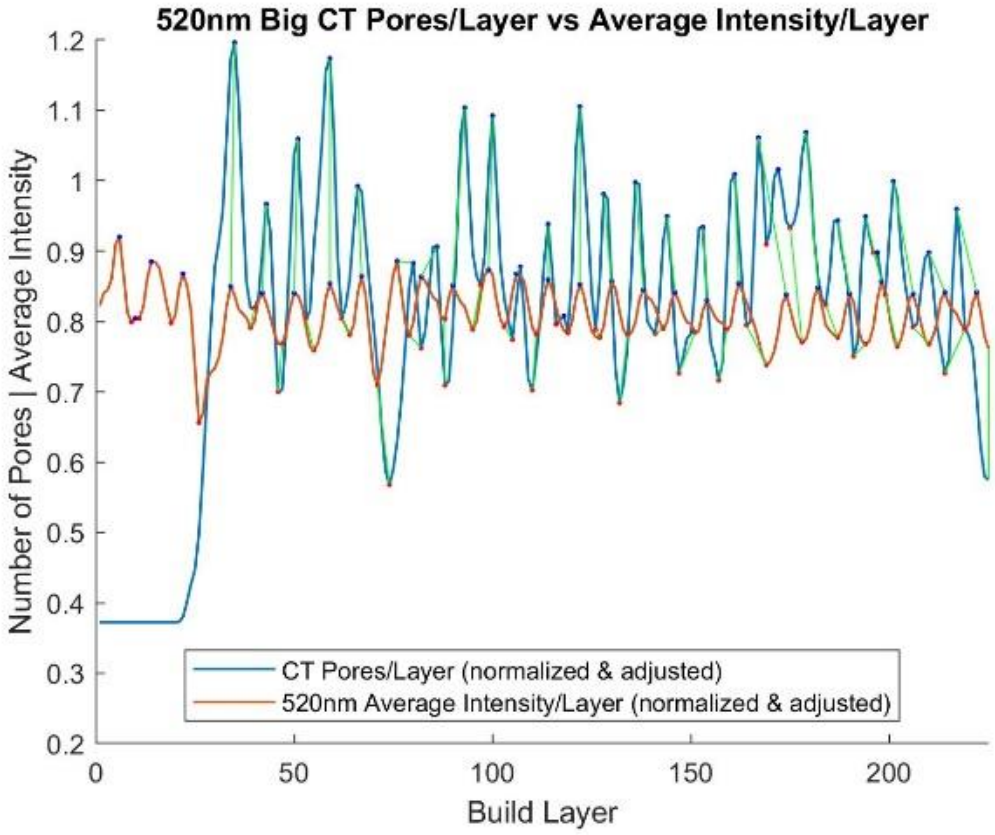

Figure 3.27 Big CT Pores vs Average 520 nm Intensity Smoothed

Similar to the average broadband intensity per layer, the average 520 nm intensity per layer has corresponding locations of spikes and drops when compared to the number of pores per layer. This again excludes an extra spike and drop in the CT pores per layer around layer 175 and the section at which the material was removed from the bottom of the large build. A similar relationship can be seen in Figure 3.28, which displays the relationship between the normalized, adjusted, and smoothed data for the average 520 nm intensity per layer and number of pores per layer for the little build.

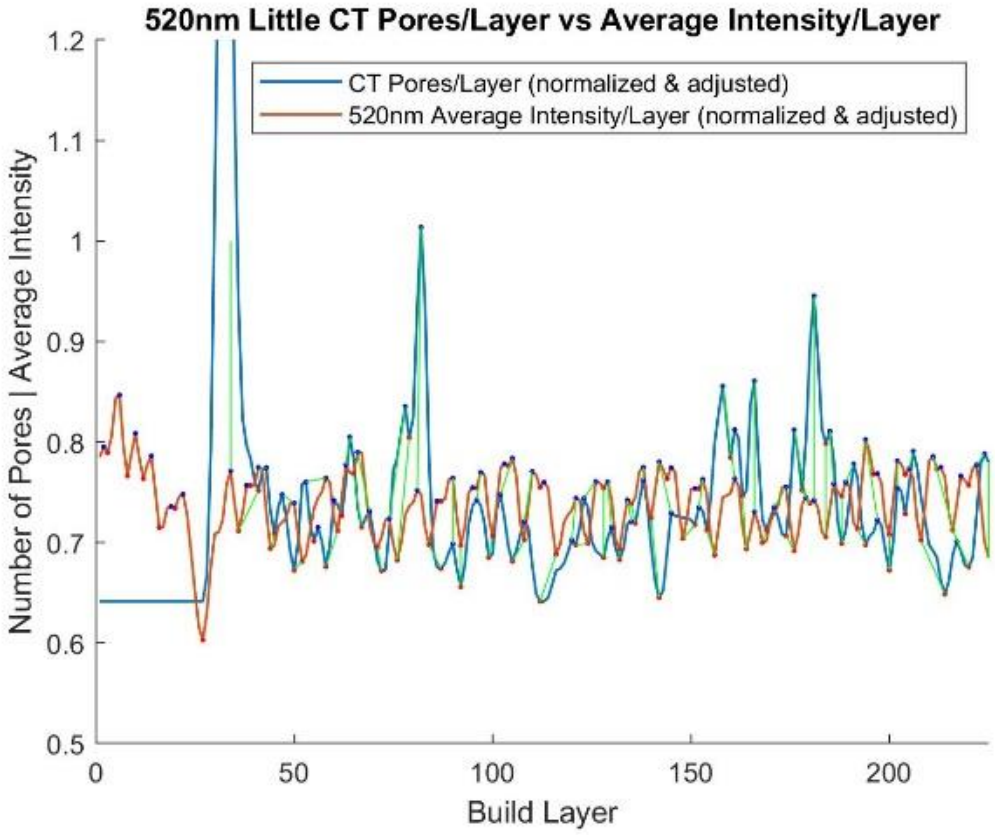

Figure 3.28 Little CT Pores vs Average 520 nm Intensity Smoothed

It can be seen that the majority of spikes and drops in the CT pores per layer occur in the same window and have a corresponding spike and drop in the average 520m intensity per layer for the little build. Again, this excludes the window around layer 175 which contains one extra spike and drop in the CT pores per layer data and the beginning section of the part where material was lost during the removal from the build plate.

Figure 3.29 displays the normalized, adjusted, and smoothed data for the average 530 nm intensity per layer and number of pores per layer for the large cuboid.

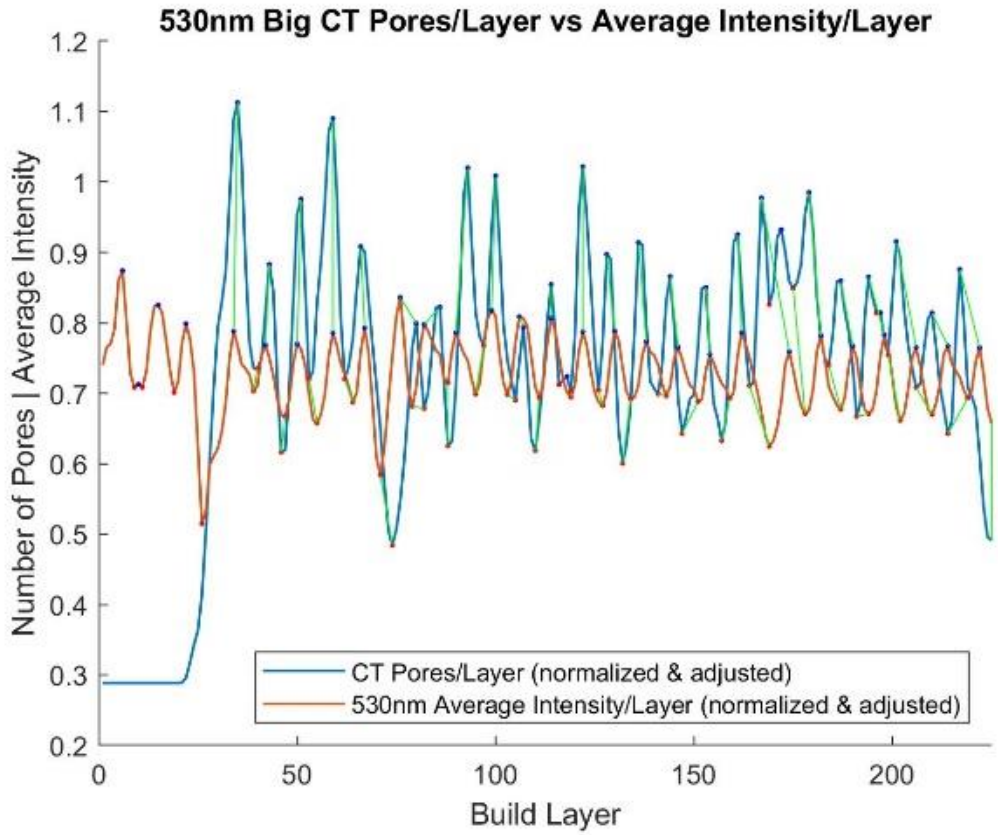

Figure 3.29 Big CT Pores vs Average 530 nm Intensity Smoothed

Similar to the average broadband and 520 nm intensity per layer, the average 530 nm intensity per layer has a corresponding spike and drop for a majority of the spikes and drops located within the same window as the CT collected number of pores per layer. It also shows the same mismatch located around layer 175 that shows an extra spike and drop in the pores per layer.

Figure 3.30 displays the same relationship between the normalized, adjusted, and smoothed data for the average 530 nm intensity per layer and number of pores per layer for the large cuboid.

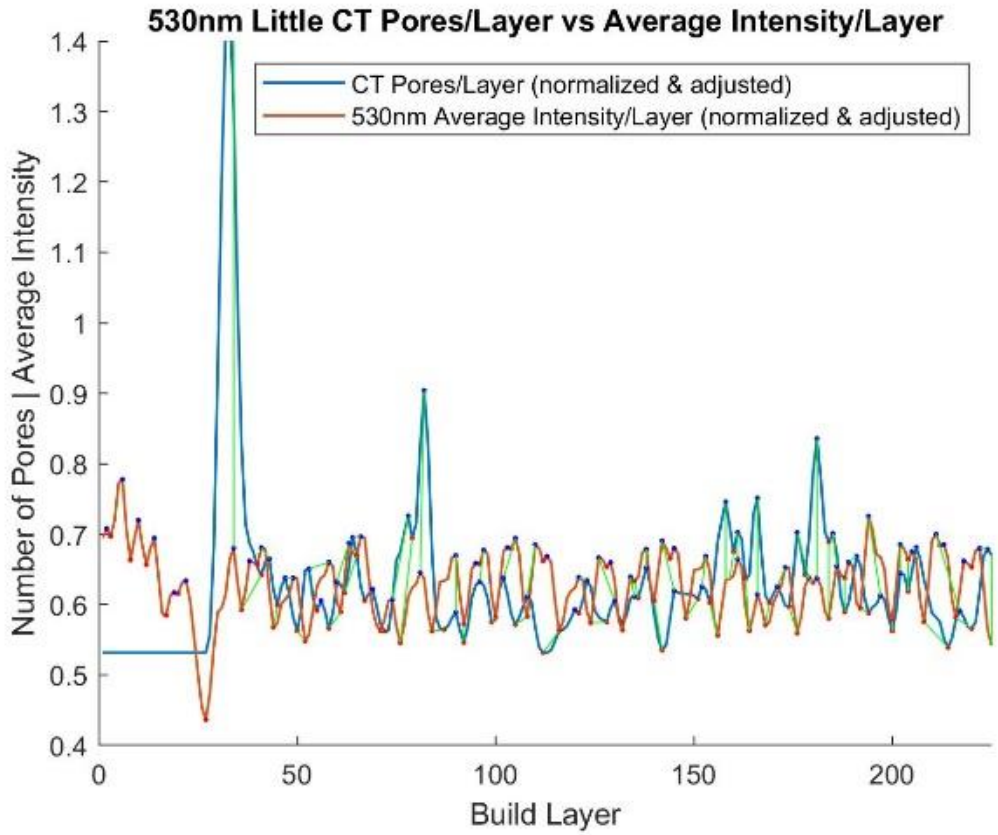

Figure 3.30 Little CT Pores vs Average 530 nm Intensity Smoothed

The same observation that is made in the other spectrums is present in the average 530 nm intensity per layer and number of pores per layer comparison. Most of the spikes and drops in the average 530 nm intensity per layer for the little parts correspond to a spike and drop in the number of pores per layer found by CT scanning the part.

Once the average spectral intensities per layer for all of the spectrums and the number of pores per layer for both the big and little builds were normalized, adjusted, and smoothed a general trend can be observed. There appears to be a direct correlation between the number of pores per layer found by CT scanning the part and the level of average spectral intensity for that window of layers in all three spectrums observed in this experiment for both builds. However, all six data sets of the average spectral intensities per build layer do not encapsulate one spike and drop in the CT collected pores per layer data around the layer 175.

Since both the number of pores per layer and the average spectral intensities per layer had to be normalized, adjusted, and smoothed to clearly see the correlation between the two, the results determined in this section are deemed to be qualitative and not quantitative.

3.7.3 Spatial Relation Attempt

An attempt to relate the measured spectral intensity to the location of the laser in 3D space while the reading occurred was made to try and correlate intensity spikes to the defects found in 3D space by CT scanning the big and little parts. This was performed using an interpolation method that takes the vector of spectral intensiy data and evenly distributes the readings allong the scan pattern of each layer. Figure 3.31 displays the top five hundred broadband intensity readings interpolated to an estimated loaction on the layer where it occurred for the first eight layers of the big part. The size of the red dot is proportional to the intensity reading of that data point.

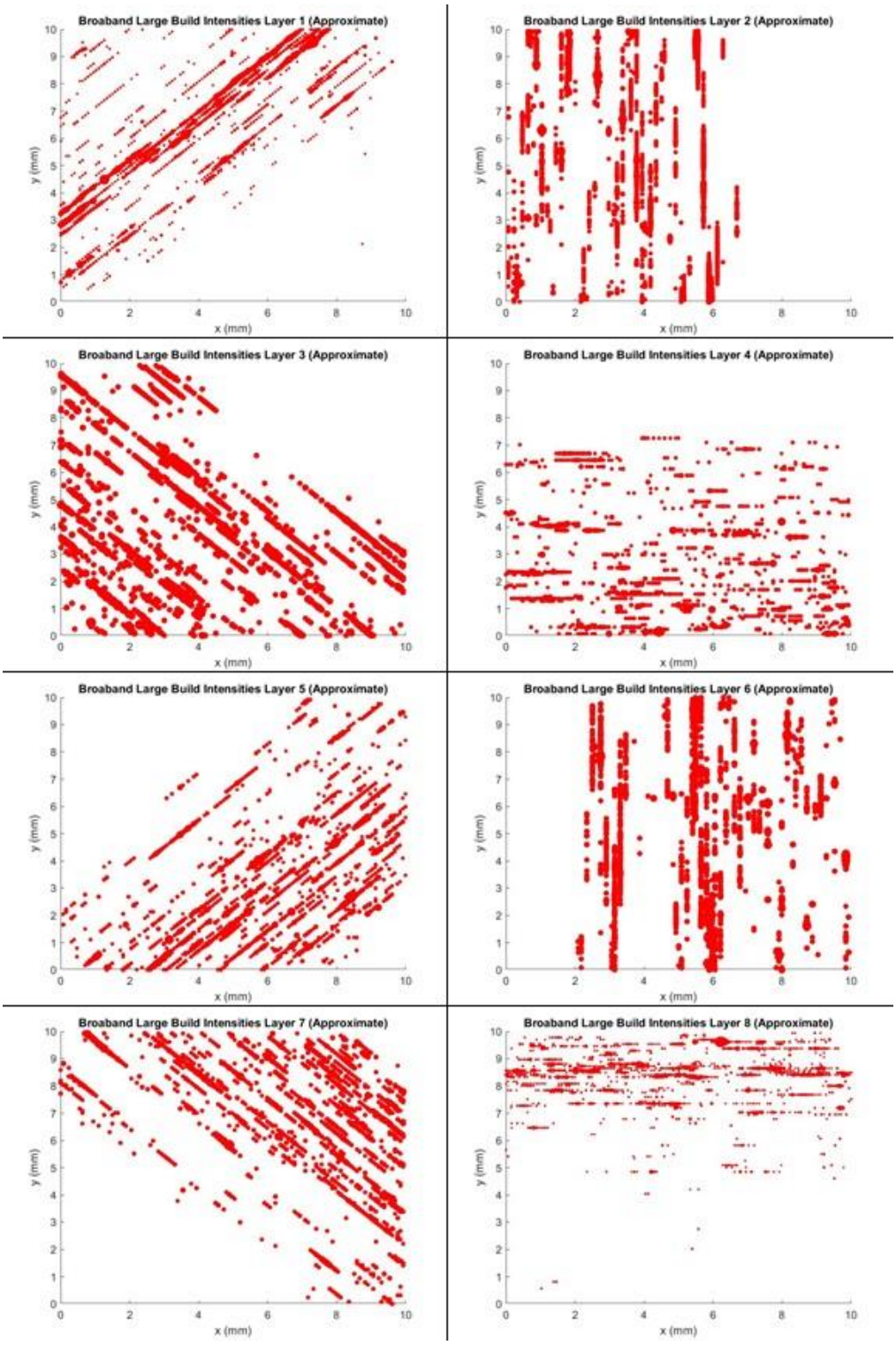

Figure 3.31 Broadband Top 500 Intensities for Big Layers 1-8

The same interpolation attempt was made for the spectral intensity recorded during the little build printing. Figure 3.32 displays the top five hundred broadband intensity measurements for the first eight layers of the little build at approximated locations of the laser based on interpolation of the intensity readings across the layer's scan pattern.

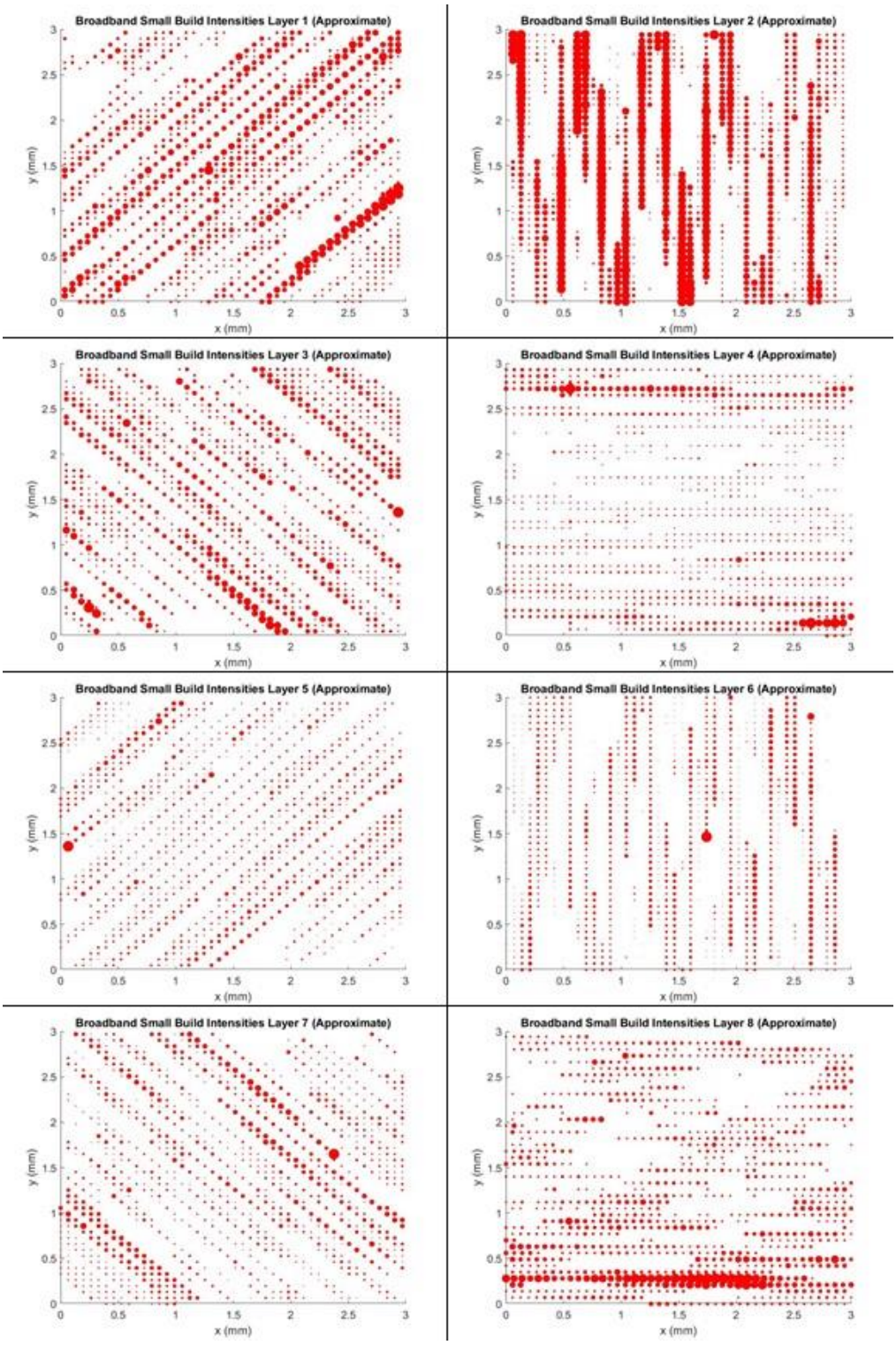

Figure 3.32 Broadband Top 500 Intensities for Little Layers 1-8

Unfortunately, due to rounding errors present in the calculation software, the spatial locations of intensity spikes could not be properly placed in the correct space. The rounding errors occurred mainly along the edges of the scan pattern where the laser has to pivot and travel the opposite direction. Another source of rounding error in the software occurs when the hatch spacing was calculated based on the number of data points in the intensity vector. A rounded hatch spacing value typically wouldn't be an issue for very small parts however, for both the big and little parts in this experiment, the hatch spacing error is compounded hundreds of times across the layer to fill in the scan pattern of the layer.

One positive outcome from the result of the spatial relation attempt is how the instances of high intensities typically occur across many readings resulting in strands of high intensity data points. Also, high intensity reading tend to occur between the halfway point and the end point of the scan patter for the layers. This is to be expected since the laser continues to introduce more energy into the system across the whole scan pattern. As the consumed energy increases the intensity readouts will be greater in compared to earlier sections where less energy is contained in the reaction.

3.8 Discussion

When comparing the average spectral intensities per layer pertaining to the big and little parts for all three spectrums considered in this experiment, it can be seen that the average intensities for the big part printing are generally greater than the average intensities for the little part. Intuitively, this makes sense since the big part has a larger scan pattern and it was observed that the intensity will increase as the laser travel though

the entire scan pattern. A longer scan pattern would result in more energy being observed for each layer of the big build compared to the little which can be seen in the average intensities per layer results. Inversely, the line to continuum per layer appears to have opposite results than the average intensity per layer results. The big build shows that the line to continuum tended to be lower per layer when compared to the little build.

The results from the layer-by-layer analysis seem to indicate a connection between high and low points of average spectral intensity measured in the build chamber as the parts were being printed and the number of pores per layer found by CT scanning the parts after they were removed from the build plate. In order to see this relationship, both sets of data had to be normalized since the values of each individual property differed by a large amount. When they are normalized, the general shapes of both the average spectral intensity per layer and the number of pores per layer appear to be similar. As the number of pores per layer increases or decrease across layers, the average spectral intensities of each layer follow. However, the magnitude of at which the number of pores per layer and the average spectral intensity change differ for each. Further observation shows that the change that is present in both sets of data doesn't always show up on the same layer being considered. Occasionally the average spectral intensity per layer shows the corresponding spike or drop up to three layers before or after the number of pores per layer show a change. With this in mind the average spectral intensity per layer and the number of pores per layer were not only normalized, the mean values were adjusted to be the same and the data sets were smoothed to consider windows eight layers

thick. This was performed in order to generalize the qualitative relationship between changes in pores per layer and the in-situ collected average spectral intensity per layer.

Windows of eight layers were selected because there appears to be a periodic trend in the intensity values every eight or so layers. This can be a result of the scan patterns of the layers repeating every eight cycles. The scan pattern of the layer can potentially influence the intensity reading since the laser and the melt pool could travel through one location more or less often than in different scan patterns. This is especially true in the scanning patters that are at an angle of 45° from horizontal. When the laser is melting the middle of the layer in one of these patterns, it will travel much longer distances compared to melting at the beginning and end corners between successive laser passes. This means more time passes between scans in the same areas in the middle of the part compared to the edges causing varying thermal cooling rates across the layer which can impact the spectroscopy data based on the temperature intensity relationship. More time between side-by-side laser passes can also contribute to lack of fusion porosity since the material would have more time to cool resulting in less successful melting in the hatch direction. Conversely, in the areas where the laser passes more frequently in the same amount of time, keyholing porosity can occur when the laser introduces more heat in the next pass before the current line has had a chance to solidify.

Once the in-situ collected average spectral intensity per layer and the number of pores per layer data sets were normalized, adjusted, and smoothed, a general relationship could be observed between the two for each of the spectrums considered in this experiment and for both the big and little build. As the number of pores per layer increase

or decrease, the average spectral intensity collected in-situ during those printing locations will increase or decrease accordingly. Because of this it can be assumed that there is a qualitative correlation between the in-situ collected spectroscopy data and pores located throughout the build of a LPBF part. This relationship is deemed to be qualitative since the magnitudes of the spikes and drops in the average spectral intensity per layer and the number of pores per layer do not agree quantitatively. The correlative property that they share is that the spikes and drops in both occur at relatively the same instances.

3.9 Conclusion

The major takeaway from this experiment is that there is a qualitative correlation between spectroscopy in-situ readings taken during a LPBF print and defects located within the parts. This correlation is deemed to be qualitative since the magnitudes of the spikes and drops in the number of pores per layer and the average spectral intensity per layer have no mathematical dependence. Since there is no specific spectral intensity value that was determined to directly cause a defect within the parts, the following claims and be made based on the analysis in this experiment. When the in-situ spectral intensity for the broadband visible spectrum, 520 nm wavelength, and 530 nm wavelength increases, it is expected that one or multiple pores will be forming. Conversely, when the in-situ spectral intensity decreases, defects are less likely to form. Future experimentation to determine the relationship between in-situ collected spectral intensities and the defects within LPBF parts should be to determine the threshold of spectral intensity that consistently produces defects in the parts. It can also focus on the more on the local areas within each layer to determine defects in a 3D space rather than on a layer-by-layer basis.

The early adaptations of LPBF printing equipment and sensing systems didn't work together as well as they do now. In this experiment, the (x, y) coordinates of the laser for each spectral intensity scan were not recorded because of limited capabilities and had to be interpolated to an inaccurate estimated location within the parts. As this ability is developed, more precise predictions can be made about defect formulation in LPBF based on in-situ collected spectroscopy data.

Chapter 4 Conclusion

In-situ monitoring offers a promising solution for defect detection during the building process that would greatly improve the quality and reliability of the parts being created by LPBF. One of the methods being developed is the use of spectroscopy to monitor the build chamber that measures the intensity of light given off by the melting process at wavelengths relevant to the material being deposited. So far limited analysis has been performed and development is in its early stages. The experiments presented in this document seek to aid in the determination of correlation between anomalies in the in-situ collected spectroscopy data from LPBF part builds and defects found by CT scanning the parts post build.

The Variable Experiment deposited single beads of material at a range of laser power and speeds. The results of the Variable Experiment show the impact on individual intensities as well as the line to continuum ratio based on given sets of processing parameters. These individual intensity reactions and the line to continuum reaction are compared to expected physical properties of the LPBF process such as the melt pool dimensions and cooling rate that are affected by varying processing parameters. Based on this comparison neither the 520nm, 530 nm, broadband, nor line to continuum intensity reactions are effected in the same way as any known physical melt pool properties listed previously. This leads to the conclusion that either the individual intensity values and line to continuum values are only impacted by individual processing parameters (only the

power) or they are being effected by something other than the processing outcomes discussed such as spatter emitted during the LPBF melting process. Determining what impacts the intensities the most in a LPBF build can be a focus of future research in in-situ spectroscopy defect detection.

The individual intensity results found in the Variable Experiment were used to generate a baseline model for estimating the intensity measured during the melting process of alloy 718 used in a LPBF build at a given set of processing parameters. As this model continues to develop, scientists will be able to determine if a defect has potentially occurred in a LPBF build based on intensity measurements that deviate greatly from the estimated intensity value. Unfortunately, this model is in early stages of development and is not able to accurately predict the intensity values for entire builds with varying geometries, only single lines. Though it demonstrates the potential for in-situ spectroscopy data of LPBF build to be compared to the estimated intensity value with the corresponding acceptable range to determine intensity spikes or drops. The upper and lower boundaries of the acceptable range would correspond to intensities known to represent defects within the LPBF part.

The Big Little Experiment fabricates two different sized build geometries at the same processing parameters and CT results for the internal defects are presented. Results from the Big Little Experiment show a qualitative correlation between fluctuations of individual intensity data as well as line to continuum and the number of defects present within the LPBF build. These results are significant despite the correlation not being quantitatively defined. The qualitative relationship found by normalizing and adjusting

both the in-situ collected spectroscopy data and the pore data found by CT scanning the LPBF parts show that changes in the spectroscopy data correspond to the fluctuations of the pores located within the parts. These results will aid in the future experimentation of determining the correlation between in-situ monitoring techniques and defects within LPBF additively manufactured parts.

The experiments performed in this work partially fulfill the requirements needed to create a model for predicting defects within an alloy 718 LPBF. A model was generated that estimates the spectral intensity that given off during a LPBF build based on the processing parameter inputs and fluctuation in the individual intensities were found to relate to changes in the number of defects within the parts. The unsuccessful portion of these experiments was determining the upper and lower intensity value boundaries that correspond to defects within the LPBF. This would have been found in the Big Little Experiment however, the only correlative relationship that was determined is the qualitative connection between fluctuations in the in-situ collected spectroscopy data and the number of pores found by CT scanning the parts. Focus of future research should focus on the determination of the upper and lower intensity values that correlate to a defect in the LPBF parts. This will need to be determined for many different processing parameter combination used to created parts with different geometries made of any powder materials.

Chapter 5 Future Work

5.1 Collect More Data

As with many experimental conclusions, a larger sample size will greatly benefit the confidence of the conclusions. These experiments could be repeated to see if the same or a stronger trend occurs. Similar experiments could also be performed to see if slight changes in the experimental setup yield similar of different analytical results. If enough data is collected and analyzed for more defined correlations, the upper and lower boundaries of the acceptable range in the model for predicting defects with in-situ collected spectroscopy data could be determined.

5.1.1 Build Geometries

Future research should also focus on the spectroscopy readings corresponding to LPBF parts consisting of more shapes and geometries. The geometries that were used in this work were a series of single print lines and two square cross-sectional cuboids with no overhanging material or specialty features. In-situ spectroscopy data collected during the interaction of the melt pool and rounded contours or overhanging geometries of LPBF parts could produce different trends than what were observed in this work.

5.1.2 Material Variety

Varying powder materials should be considered in repeating any experiment involving in-situ process monitoring to examine the varying measurements that result from reactions of the same processing parameters with different materials. Similar to the

results of the variable experiment, expected spectral intensity formulas could be developed for every common material used to build LPBF parts. In this work, the only material considered is nickel super alloy 718 which is common in LPBF however, many other materials can be utilized to create components in LPBF. An example of another material commonly used in LPBF is titanium alloy Ti-6Al-4V.

5.1.3 Processing Parameter Combinations

A high number of combinations of processing parameters exist for LPBF builds. Because of this, the Variable Experiment could be repeated with any new combination of processing parameters to increase the confidence of the intensity estimation formula developed.

5.2 Machine Learning

The use of machine learning shows promise in future of in-situ monitoring of LPBF builds to detect defects in real time. The biggest component in developing a machine learning method is the training model.

5.2.1 Training Model

Experimental data sets can be collected to create a machine learning training model. These data sets need to have defined correlations between the quality of the melting of a LPBF part and the corresponding spectroscopy reading for each situation. Any current spectral intensity reading will automatically be scored based on the training model to give a prediction if the current measurement has a high or low probability of defect creation.

5.2.2 Scrap or Correct Builds based on In-situ Monitoring

If a training model fully develops, the ability to detect defect inducing scenarios within in-situ monitoring methods could lead to a more advanced feedback algorithms within the LPBF machine code that can take action when these scenarios occur. Depending on the classification of severity of a defect that the machine learning model detects, this feedback loop could automatically scrap the current build saving time, money, and material. Further advancement can unlock the ability of a LPBF machine to automatically correct defects in the parts without having to stop or restart the build entirely.

References

[1] R. Bogue, "3D Printing: The Dawn of a New Era in Manufacturing?," *Assembly Automation,* vol. 33, no. 4, pp. 307-311, 20 September 2013.

[2] T. Nancharaih, K. S. Prakash and S. V. Rao, "Additive Manufacturing Techniques in Manufacturing - An Overview," *Materials Today: Proceedings,* vol. 5, no. 2, pp. 3873-3882, 2018.

[3] M. Attatan, "The rise of 3-D printing: The advantages of additive manufacturing over traditional manufacturing," *Business Horizons,* vol. 60, no. 5, pp. 677-688, 2017.

[4] F. Calignano, D. Manfredi, E. P. Ambrosio, S. Biamino, M. Lombardi, E. Atzeni, A. Salmi, P. Minetola, L. Iuliano and P. Fino, "Overview on Additive Manufacturing Technologies," *Proceesings of the IEEE,* vol. 104, no. 4, pp. 593-612, April 2017.

[5] L. Criales, Y. Arisoy, B. Lane, S. Moylan, A. Donmez and T. Ozel, "Laser powder bed fusion of nickel alloy 625: Experimental investigations of effects of process parameters on melt pool size and shape with spatter analysis," *International Journal of Machine Tools & Manufacturing,* vol. 121, pp. 22-36, October 2017.

[6] T. Kurzynowski, E. Chlebus, B. Kunicka and J. Reiner, "Parameters in selective laser melting for processing metallic powders," in *SPIE*, 2012.

[7] J. E. Gockel, "Integrated Control of Solidification Microstructure and Melt Pool Dimensions in Electron Beam Wire Feed Additive Manufacturing of Ti-6Al-4V," Carnegie Mellon University, Pittsburgh, 2014.

[8] Y. Zhang, J. Y. Fuh, D. Ye and G. S. Hong, "In-Situ Monitoring of Laser-Based PBF Via off-axis Vision and Image," *Additive Manufacturing*, vol. 25, pp. 263-274, 2019.

[9] X. Zhang, B. Cheng and C. Tuffile, "Simulation study of the spatter removal process and optimization design of gas flow systme in laser powder bed fusion," *Additive Manufacturing,* vol. 32, March 2020.

[10] S. Ly, A. M. Rubenchik, S. A. Khairallah, G. Guss and M. J. Matthews, "Metal vapor micro-jet controls material redistribution in laser powder bed fusion additive manufacturing," *Scientific Reports*, vol. 7, 22 June 2017.

[11] G. Marinelli, F. Martina, S. Ganguly and S. Williams, "Grain refinement in an unalloyed tantalum structure by combining Wire + Arc additive manufacturing and vertical cold rolling," *Additive Manufacturing,* vol. 32, 2020.

[12] D. Rosenthal, "The Theory of Moving Sources of Heat and Its Application to Metal Treatments," *Transactions of the A.S.M.E.*, vol. 68, pp. 849-866, 1946.

[13] R. E. Evans, "Thermal Modeling of Coordinated Multi-Beam Additive Manufacturing," Wright State University, Dayton, 2020.

[14] S. Bontha and N. W. Klingbeil, "Thermal Process Maps for Controlling Microstructure in Laser-Based Solid Freeform Fabrication," in *Solid Freeform Fabrication Proceedings*, Austin, 2003.

[15] A. Vasinota, J. L. Beuth and R. Ong, "Melt Pool Size Control in Thin-Walled and Bulky Parts via Process Maps," in *Solid Freeform Fabrication Proceedings*, Austin, 2001.

[16] J. P. Oliveira, A. D. LaLonde and J. Ma, "Processing parameters in laser powder bed fusion metal additive manufacturing," *Materials & Design*, vol. 193, 2020.

[17] L. Scime and J. Beuth, "Using machine learning to identify in-situ melt pool signatures indicative of flaw formation in a laser powder bed fusion additive manufacturing process," *Additive Manufacturing*, vol. 25, pp. 151-165, January 2019.

[18] "What is Hot Isostatic Pressing (HIP)?," KOBE STEEL, LTD, 2020. [Online]. Available: https://www.kobelco.co.jp/english/products/ip/technology/hip.html#page-k12. [Accessed 2020].

[19] A. Leon, G. K. Levy, T. Ron, A. Shirizly and E. Aghion, "The effect of hot isostatic pressure on the corrosion performance of Ti-6Al4 V produced by an electron-beam

melting additive manufacturing process," *Additive Manufacturing,* vol. 33, May 2020.

[20] V. Tripathi, A. Armstrong, X. Gong and G. Manogharan, "Milling of Inconel 718 block supports fabricated using laser powder bed fusion," *Journal of Manufacturing Processes,* vol. 34, pp. 740-749, August 2018.

[21] B. Shen, H. Li, S. Liu and J. Zou, "Influence of laser post-processing on pore evolution of Ti–6Al–4V alloy by laser powder bed fusion," *Journal of Alloys and Compounds,* vol. 818, March 2020.

[22] L. Sheridan, O. E. Scott-Emuakpor, T. George and J. E. Gockel, "Relating Porosity to Fatigue Failure in Additively Manufactured Alloy 718," *Materials Science and Engineering,* vol. 727, pp. 170-176, 2018.

[23] J. E. Gockel, L. Sheridan, B. Koerper and B. Whip, "The Influence of Additive Manufacturing Processing Parameters on Surface Roughness and Fatigue Life," *International Journal of Fatigue,* vol. 124, pp. 380-388, 2019.

[24] T. Mukherjee and T. DebRoy, "Mitigation of lack of fusion defects in powder bed fusion additive manufacturing," *Journal of Manufacturing Processes,* vol. 36, pp. 442-449, 2018.

[25] C. Zhao, K. Fezzaa, R. W. Cunningham, H. Wen, F. De Carlo, L. Chen, A. D. Rollett and T. Sun, "Real-Time Monitoring of Laser Powder Bed Fusion Process

Using High-Speed X-ray Imaging and Diffraction," *Scientific Reports,* vol. 7, no. 1, 2017.

[26] M. Saunders, "How process parameters drive successful metal AM part production," *Metal Additive Manufacturing,* vol. 4, no. 2, pp. 127-135, 2018.

[27] A. Du Plessis, "X-ray tomography for the advancement of laser powder bed fusion additive manufacturing," *Journal of Microscopy,* vol. 00, no. 0, pp. 1-10, June 2020.

[28] P. Boulware, "In-Process Monitoring Techniques for Laser Powder Bed Fusion," Columbus, OH, 2017.

[29] S. M. Kelly, P. C. Boulware, L. Cronley, G. Firestone, M. Jamshidinia, J. Marchal, T. Stempky and C. Reichert, "In-Process Sensing of Laser Power Bed Fusion Additive Manufacturing," EWI, Washington, DC, 2017.

[30] J.-B. Forien, N. P. Calta, P. J. DePond, G. M. Guss, T. T. Roehling and M. J. Matthews, "Detecting keyhole pore defects and monitoring process signatures during laser powder bed fusion: A correlation between in situ pyrometry and ex situ X-ray radiography," *Additive Manufacturing,* vol. 35, 2020.

[31] T. Purtonen, A. Kalliosarri and A. Salminen, "Monitoring and Adaptive Control of Laser Processes," *Physics Procedia,* vol. 56, pp. 1218-1231, 2014.

[32] M. Hirsch, R. Patel, W. Li, G. Guan, R. K. Leach, S. D. Sharples and A. T. Clare, "Assessing the Capability of In-Situ Nondestructive Analysis During Layer Based Additive Manufacture," *Additive Manufacturing,* vol. 13, no. 2017, pp. 135-142, 2017.

[33] A. Gaikwad, R. Yavari, M. Montazeri, K. Cole, L. Bian and P. Rao, "Toward the digital twin of additive manufacturing: Integrating thermal simulations, sensing, and analytics to detect process faults," *IISE Transactions,* vol. 0, no. 0, pp. 1-14, 24 January 2020.

[34] Albeck, Melissa;, "Inconel 718 powder (Size cuts: -90µm/+45µm)," Matmatch GmbH, Munich, 2020.

[35] A. J. Dunbar and A. R. Nassar, "Assessment of optical emission analysis for inprocess monitoring of powder bed fusion additive manufacturing," *Virtual and Physical Prototyping,* vol. 13, no. 1, pp. 14-19, 2018.

[36] "OpenAdditive PANDA Metal 3D Printing System," Open Additive, LLC., 2019. [Online]. Available: openadditive.com. [Accessed 2020].

[37] D. B. Witkin, D. Patel, T. V. Albright, G. E. Bean and T. MaLouth, "Influence of surface conditions and specimen orientation on high cycle fatigue properties of Inconel 718 prepared by laser powder bed fusion," *International Journal of Fatigue,* vol. 132, March 2020.

[38] A. Plotkowski, M. Kirka and S. Babu, "Verification and validation of a rapid heat transfer calculation methodology for transient melt pool solidification conditions in powder bed metal additive manufacturing," *Additive Manufacturing,* vol. 18, pp. 256-268, 2017.

[39] J. R. Walker, "Multi-Sensor Approach to Determine the Effect of Geometry on Microstructure in Additive Manufacturing," Wright State University, Dayton, 2019.

[40] "Statistics and Machine Learning Toolbox," The Mathworks, Inc., Natick, 2020.

[41] "Percent Error Formula," University of Iowa, 2017. [Online]. Available: http://astro.physics.uiowa.edu/ITU/glossary/percent-error-formula/. [Accessed 06 June 2020].

[42] E. Dauria, "Looking at R-Squared," Medium, 13 May 2019. [Online]. Available: https://medium.com/@erika.dauria/looking-at-r-squared-721252709098. [Accessed 26 June 2020].

[43] L. Sheridan, J. E. Gockel and O. E. Scott-Emuakpor, "Primary Processing Parameters, Porosity Production, and Fatigue Prediction for Additively Manufactured Alloy 718," *Journal of Materials Engineering and Performance,* vol. 28, pp. 5387-5397, 2019.

[44] A. Purwanto, R. I. Wisnuwijaya, E. K. Sari and W. S. Dwandaru, "Non-contact temperature measurement based on Wien’s displacement law using a single

webcam in the infrared spectrum region," *Physics Education,* vol. 55, no. 2, March 2020.